Lehrstuhl für Experimentalphysik E21

CALCULATIONS FOR NEUTRON SPIN ECHO
Optimization of the magnetic field geometries and preparations and analysis of experiments on crystal lattice dynamics

Sergey Prokudaylo

Vollständiger Abdruck der von der Fakultät für Physik der Technischen Universität München zur Erlangung des akademischen Grades eines

Doktor der Naturwissenschaften

genehmigten Dissertation.

Vorsitzender: Univ.-Prof. Dr. Manfred Kleber

Prüfer der Dissertation:

1. Univ.-Prof. Dr. Peter K. Böni
2. Univ.-Prof. Dr. Winfried Petry

Die Dissertation wurde am 29.03.2004 bei der Technische Universität München eingereicht und durch die Fakultät für Physik am 20.09.2004 angenommen.

Introduction.

Neutron Resonance Spin-Echo (NRSE) has developed to a versatile tool in neutron science. Applications in high resolution lattice dynamics, high resolution small angle scattering and on the slow dynamics in macromolecules are well-established now at five commissioned NRSE instruments around the world. Two further ones are near completion at TUM and at present a number of design studies of new instruments takes place - at least three instruments are planned in the United States. The refinement of the technique and the advent of new perspectives now requires extended calculations and design studies and it is the aim of the thesis to contribute to these further developments.

In the nineties, the first resonance coils for NRSE spectroscopy were based on try-and-error methods 2D and 3D calculations of the complex field geometries combining air fields, mu - metal regions and RF fields were only done sporadically. Only recently comfortable programs based on elegant algorithms became available for reasonable price. This now opens a lot of new possibilities and the present thesis certainly should be seen as a first step into a new area. The experimental optimisation of the shielding geometries would be much more time and cost consuming than the calculations. New curved field geometries would require high investments and serious simulations have to be done before realization. The capabilities of the MIEZE technique, a variant of NRSE, need deep calculations before realization.

Besides fundamental aspects, knowledge of phonon lifetimes is of basic interest in high-performance electronics as heat conductivity strongly depends on propagation of phonons (ballistic phonons). In this context industry has produced first isotopically pure large size Si crystals, aimed to be a future material of the high-power electronics. Also of high potential interest in this field is isotopically clean diamond with its unrivalled heat conductivity. A major technique for the measurements of the phonon lifetimes is the standard triple-axis technique. Uniting it with the NRSE technique enhances the energy resolution of the triple-axis technique by two-three order of magnitude. However the preparation and the evaluation of these experiments need special treatment, because the commonly used 2D approach to the transmission function can not be applied in this case, as the curvature of the dispersion surfaces has to be considered in all 4D. This work is intended to be a major step in this direction.

Table of contents.

Chapter 1.
The basic principles of Spin Echo.

1.1. Basic principle of neutron spin echo.

The basic idea of Neutron Spin Echo can be explained by the following scheme: assume a polarized neutron beam (for this initial consideration monochromatic) passes two regions (before and after the sample) of equal length with magnetic fields, and these fields are of the same value but of opposite sign (direction), as it is shown in Figure 1.

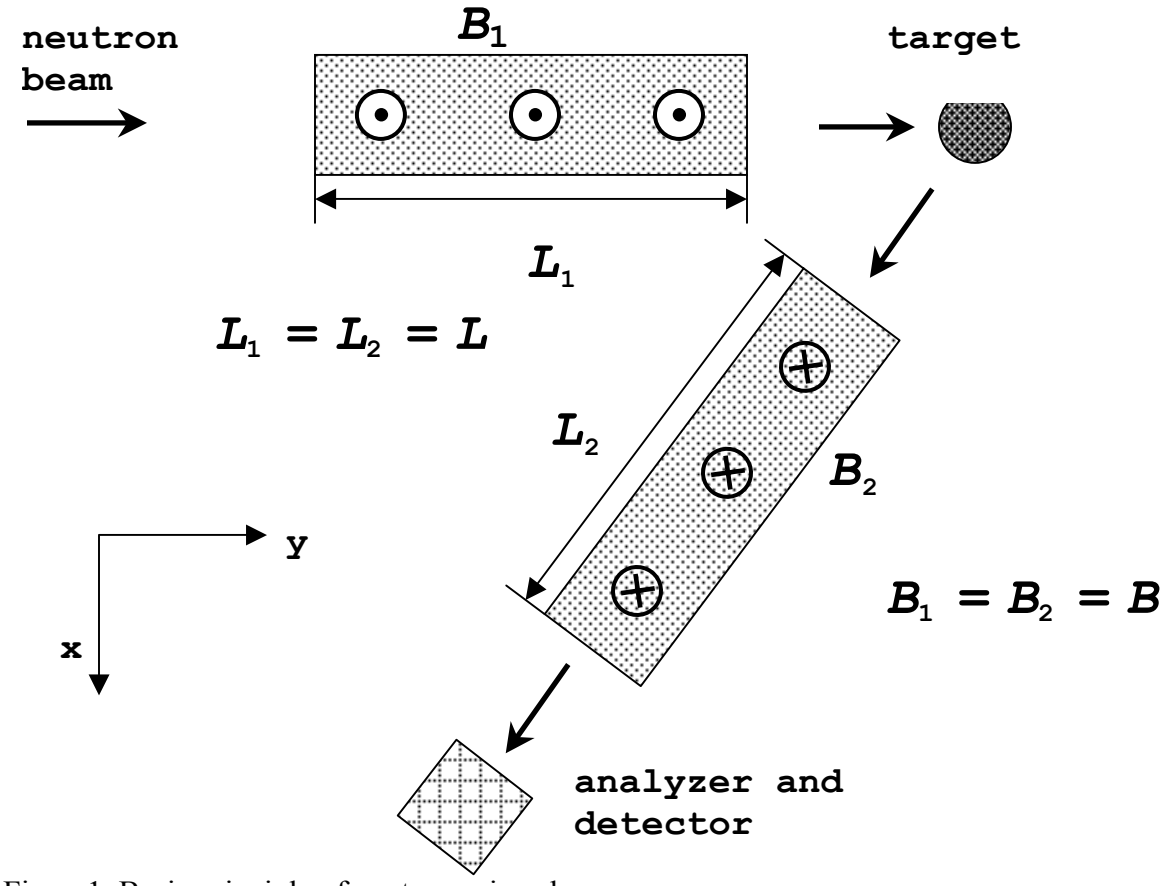

Figure1. Basic principle of neutron spin echo.

Consider a neutron spin in a classical way. Let the spin initially point in x direction. Passing region B_1, it precesses, then scatters on the target and then enters the second field. In the field B_2 it precesses again, but, as the field is in opposite direction, its sense of rotation is reversed. The precession angle is proportional to the time spent in the field region or inverse

proportional to the velocity of the neutron. If the scattering would be elastic, the neutron in the second field would travel with the same velocity as in the first field and the spin direction at the analyzer would be the same as on entering the first field (because the fields and the lengths of this two regions are equal). This means that the polarization of the beam at the analyzer would be the same as before the first field.

Consider now a small change of energy of the neutron upon scattering. In the second field, the neutron would now have a different velocity and in this way the precession angle after the second region will be changed. This change of beam polarization contains the information about the energy change and in this way about the microscopic dynamics in the sample. The change of energy and momentum of the scattered neutron is given by the scattering function $S(\boldsymbol{q},\omega)$, which describes the probability of a scattering event with energy change ω and momentum change $\boldsymbol{q}$. Change of the polarization gives the information about $S(\boldsymbol{q},\omega)$, describing the microscopic dynamics of the sample.

The precession in the first field is given by:

$$\varphi_1 = \omega_L t_1 = \gamma B \frac{L_1}{v_i} \tag{1.1}$$

In the second field:

$$\varphi_2 = \omega_L t_2 = \gamma B \frac{L_2}{v_k} \tag{1.2}$$

where $\omega_L = \gamma B$ is the Larmor frequency, v_i is the velocity of the incident neutrons, v_k is the velocity of the scattered neutrons. γ is the gyromagnetic ratio, $\gamma = 2\pi * 2916$ *rad Gauss*$^{-1}$. Taking $B_1 = B_2 = B$ and $L_1 = L_2 = L$, the net spin precession after passing both regions is:

$$\varphi = \varphi_1 - \varphi_2 = \gamma B \frac{L_1}{v_i} - \gamma B \frac{L_2}{v_k} = \gamma B L \left(\frac{1}{v_i} - \frac{1}{v_k}\right) \tag{1.3}$$

Assuming $v_k = v_i \pm \delta v$; $\delta v << v_k$, the resulting precession angle is:

$$\varphi = \gamma B L \frac{\delta v}{v^2} \tag{1.4}$$

and with the neutron energy transfer given by:

$$\hbar\omega = \frac{m}{2}(v_k^2 - v_i^2) = m v \delta v \tag{1.5}$$

we obtain:

$$\varphi = \gamma B L \frac{\delta v}{v^2} = \left(\frac{\hbar \gamma B L}{m v^3}\right)\omega = \omega \tau_{NSE} \tag{1.6}$$

τ_{NSE} is called "spin-echo time" (because it is of dimension of time). It is describing the energy resolution of a NSE measurement for a particular experimental setup. The physical meaning of τ_{NSE} will be discussed later in this thesis. The polarization after the second field is given by:

$$< P_x >= \int S(q,\omega)\cos(\varphi)d\omega = \int S(q,\omega)\cos(\omega\tau_{NSE})d\omega \qquad (1.7)$$

The cosine relates just the projection of the neutron spin to the direction of polarization. $<P_x>$ is the cosine Fourier transform of $S(\boldsymbol{q},\omega)$. To get $S(\boldsymbol{q},\omega)$ one has to do the inverse transform, transform via $\tau_{NSE.}$ To do that one needs the dependence of $<P_x>$ from $\tau_{NSE.}$ There are two ways to get this dependence: to vary the length of the magnetic field region or to vary the magnetic field strength. Usually the field strength is being varied. Frankly speaking, a Neutron Spin Echo experiment consists in a measurement of the polarization at different field values. The measured $<P_x>(\tau_{NSE})$, processed by Fourier transform, gives the dependence of the scattering function from the energy transfer. The classical example of this energy dependence is the Lorentzian function, describing an anharmonicity of the crystal oscillations [1]:

$$S(q,\omega) \propto \frac{\Gamma^2}{\Gamma^2 + (\omega - \omega_0)^2} \qquad (1.8)$$

where ω_0 is the resonance frequency, Γ is the anharmonic damping of the oscillation (half-width at half maximum). For such a process the dependence $<P_x>(\tau_{NSE})$ will be the following:

$$< P_x > \propto \int \frac{\Gamma^2}{\Gamma^2 + (\omega - \omega_0)^2}\cos((\omega - \omega_0)\tau_{NSE})d\omega \propto e^{-\Gamma\tau_{NRSE}} \qquad (1.9)$$

The logarithm of $<P_x>(\tau_{NSE})$ gives a linear function with its slope representing Γ. The explanation of the Neutron Spin Echo principle above is done for a monochromatic beam. Consider now a polychromatic beam. If there is only elastic scattering, neutrons of each velocity after passing both fields come to the same spin state as before. If there is an energy change in scattering, the outcome polarization for each velocity is given by the same formula (1.7) as in the monochromatic case. To get the total polarization for the velocity distribution, the expression (1.7) has to be integrated over the velocity distribution:

$$< P_x >= \int f(v)dv \int S(q,\omega)\cos(\omega\tau_{NSE})d\omega = \int d\omega S(q,\omega)\int f(v)dv\cos(\omega\tau_{NSE}) = \int S(q,\omega)F(\omega\tau_{NSE})d\omega$$

(1.10)

τ_{NSE} has an inverse cubic dependence on the neutron velocity. For *f(v)* constant in between $v \pm \delta v$, where $\delta v << v$, and zero elsewhere $F(\omega, \tau_{NSE})$ is [3]:

$$F(\omega\tau_{NRSE}) = \cos(\omega\overline{\tau}_{NRSE})\frac{\sin(3\delta v/v\,\omega\overline{\tau}_{NRSE})}{3\delta v/v\,\omega\overline{\tau}_{NRSE}} \tag{1.11}$$

where $\overline{\tau}_{NSE}$ is the average τ_{NSE}. This result shows that the formalism for obtaining scattering function parameters like in equation (1.9) is valid only for a quasi-monochromatic beam. It tells that the NSE method will work in real experimental conditions (when some spread in velocity distribution always exits), but working with a widely polychromatic beam needs some care to get the scattering function parameters from the experiment[3]. The dependence of the scattering function from momentum adds new features to the NSE technique, which will be discussed later.

To get a physical meaning of τ_{NSE}, consider the echo effect described above from a quantum mechanical point of view. In this approach the neutron beam is represented by a wave packet, initially polarized in x direction. The wave packet propagates through the experimental setup, schematically shown in Figure1.

The initial state, an eigenstate σ_x with eigenvalue 1, is a superposition of the eigenstates σ_z:

$$|+\rangle_x = \frac{|+\rangle_z + |-\rangle_z}{\sqrt{2}} = \frac{1}{\sqrt{2}}\begin{bmatrix}1\\1\end{bmatrix} \tag{1.12}$$

On entering the magnetic field region, the wave packet is split into two coherence volumes corresponding to spin-up and spin-down eigenstates. These volumes correspond to two possible orientations of the spin in the magnetic field (up and down) and two levels of potential energy respectively:

$$|+\rangle_z \to \mu B\,,\ |-\rangle_z \to -\mu B \tag{1.13}$$

where $\mu = eh/2\pi M_p c$ is the nuclear Bohr magneton, M_p is the proton mass.

Because of this difference in potential energy, these two wave packets will travel with different velocities, which to first order are symmetric:

$$v_{\pm} = v_i \pm \hbar \frac{\mu B}{m v_0} = v_i \pm \frac{\hbar \omega_z}{m v_0} \tag{1.14}$$

and respectively with different *k*:

$$k_{\pm} = k_i \pm \frac{\hbar \omega_z}{\hbar^2 k_i} m \tag{1.15}$$

where $\omega_z = \mu B/\hbar = \frac{1}{2}\omega_L$, m is the mass of neutron.

These two states will take different times to travel through the field:

$$t_{\pm} = \frac{L}{v_i \pm \hbar \frac{\mu B}{m v_i}} = \frac{L}{v_i} \mp \frac{L \hbar \omega_z}{m v_i^3} = t_0 \mp \frac{\tau_{NSE}}{2} \tag{1.16}$$

so there will be a relative delay between them:

$$t_{\pm} = t_+ - t_- = \tau_{NSE} \tag{1.17}$$

τ_{NSE} is the time difference for the two states to reach a given point after leaving the first field region. The action of the second field is to remove this delay, superposing these spin-up and spin down packets again. The interference between these two packets will give the echo signal. There is a time delay between two states and for the spin up packet, the scattering event takes place at a moment t at some point in space ***r***, for the spin down packet scattering at the same point* will occur at time $t + \tau_{NSE}$.

* Scattering of course occurs in the whole sample, however significant amplitude in the scattered beam is only obtained from superposing amplitudes scattered at one, well localized plane of the size of the coherence volume.

In this way the spin echo time obtains the meaning of an interaction time of the split incident wave packet with a local scattering area.

On entering the field the wave packet can be described by the following wave function:

$$\psi = e^{i(k_i y - E_i t/\hbar)} \begin{bmatrix} 1 \\ 1 \end{bmatrix} \tag{1.18}$$

On leaving the field region, the wave function is:

$$\psi = e^{i(k_i y - E_i t/\hbar)} \begin{bmatrix} e^{-i\Delta k L} \\ e^{i\Delta k L} \end{bmatrix} = e^{i(k_i y - E_i t/\hbar)} \begin{bmatrix} e^{-i\omega_z L/v_i} \\ e^{i\omega_z L/v_i} \end{bmatrix} \tag{1.19}$$

where $\omega_z = \mu B/\hbar$. After scattering the wave function looks like:

$$\psi = e^{i(k_k y - E_k t/\hbar)} \begin{bmatrix} \rho(\boldsymbol{r}, t - \frac{\tau_{NSE}}{2}) \\ \rho(\boldsymbol{r}, t + \frac{\tau_{NSE}}{2}) \end{bmatrix} \begin{bmatrix} e^{-iE_i \Delta t} e^{iE_k \Delta t} \\ e^{iE_i \Delta t} e^{-iE_k \Delta t} \end{bmatrix} \begin{bmatrix} e^{-i\omega_z L/v_i} \\ e^{i\omega_z L/v_i} \end{bmatrix} \tag{1.20}$$

where $\rho(\boldsymbol{r},t)$ is the density of the scattering media at point $\boldsymbol{r}$, at time t.

The factor $\begin{bmatrix} e^{-iE_i\Delta t}e^{iE_k\Delta t} \\ e^{iE_i\Delta t}e^{-iE_k\Delta t} \end{bmatrix}$ describes the phase difference obtained because the wave packets arrive to the point of scattering at different times. The phases of the two states on leaving the second field will be (some graphical explanation is given in Figure 2):

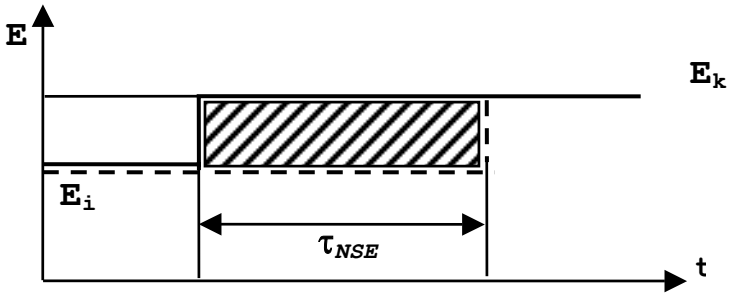

Figure2: The time-energy diagram of spin-up and spin-down packets. The shaded area represents the phase difference between these two packets.

$$\psi = e^{i(k_k y - E_k t/\hbar)} \begin{bmatrix} \rho(\boldsymbol{r},t-\frac{\tau_{NSE}}{2}) \\ \rho(\boldsymbol{r},t+\frac{\tau_{NSE}}{2}) \end{bmatrix} \begin{bmatrix} e^{i\frac{\tau_{NSE}}{2}(E_k-E_i)} \\ e^{-i\frac{\tau_{NSE}}{2}(E_k-E_i)} \end{bmatrix} \begin{bmatrix} e^{-i\omega_z L/v_i} \\ e^{i\omega_z L/v_i} \end{bmatrix} \begin{bmatrix} e^{i\omega_z L/v_k} \\ e^{-i\omega_z L/v_k} \end{bmatrix} \tag{1.21}$$

or

$$\begin{aligned} \psi &= e^{i(k_k y - E_k t/\hbar)} \begin{bmatrix} \rho(\boldsymbol{r},t-\frac{\tau_{NSE}}{2}) \\ \rho(\boldsymbol{r},t+\frac{\tau_{NSE}}{2}) \end{bmatrix} \begin{bmatrix} e^{i\frac{\tau_{NSE}}{2}(E_k-E_i)} \\ e^{-i\frac{\tau_{NSE}}{2}(E_k-E_i)} \end{bmatrix} \begin{bmatrix} e^{i\omega_z L(\frac{1}{v_k}-\frac{1}{v_i})} \\ e^{-i\omega_z L(\frac{1}{v_k}-\frac{1}{v_i})} \end{bmatrix} = \\ &= e^{i(k_k y - E_k t/\hbar)} \begin{bmatrix} \rho(\boldsymbol{r},t-\frac{\tau_{NSE}}{2}) \\ \rho(\boldsymbol{r},t+\frac{\tau_{NSE}}{2}) \end{bmatrix} \begin{bmatrix} e^{i\frac{\tau_{NSE}}{2}(E_k-E_i)} \\ e^{-i\frac{\tau_{NSE}}{2}(E_k-E_i)} \end{bmatrix} \begin{bmatrix} e^{i\frac{\tau_{NSE}}{2}(E_k-E_i)} \\ e^{-i\frac{\tau_{NSE}}{2}(E_k-E_i)} \end{bmatrix} = \\ &= e^{i(k_k y - E_k t/\hbar)} \begin{bmatrix} \rho(\boldsymbol{r},t-\frac{\tau_{NSE}}{2}) \\ \rho(\boldsymbol{r},t+\frac{\tau_{NSE}}{2}) \end{bmatrix} \end{aligned} \tag{1.22}$$

As said above, the polarization on the detector is the interference of spin-up and spin-down states, and will be proportional to:

$$\langle\sigma\rangle_x \propto \left\langle \rho(\boldsymbol{r},t+\frac{\tau_{NSE}}{2}), \rho(\boldsymbol{r},t-\frac{\tau_{NSE}}{2}) \right\rangle_{\boldsymbol{r},t} = \langle \rho(\boldsymbol{r},t), \rho(\boldsymbol{r},t+\tau_{NSE}) \rangle_{\boldsymbol{r},t} \tag{1.23}$$

which is density-density correlation function. Thus in this model the parameter τ_{NSE} appears to be a real physical delay between the two states. The product of the amplitudes of the two (relatively delayed) beams, gives directly the time dependence of the correlation function.

The rigorous quantum mechanical derivation of the spin echo principle in case of a non-monochromatic beam can be found in [4].

The lay-out of a neutron spin – echo spectrometer can be seen on the next Figure 3. The incoming neutron beam is being initially polarized by means of a supermirror polarizer. Magnetic fields are created by solenoids, with their field direction usually parallel to optical axis. An alternative approach uses coils with their field perpendicular to the optical axis. The design of such a coil is one of the objects of this thesis and will be cited in detail.

Examples of neutron spin echo spectrometers are Reseda (FRM-2, Munich, Germany, under construction) [5], IN20 (ILL, Grenoble, France) [6], and much more around the world.

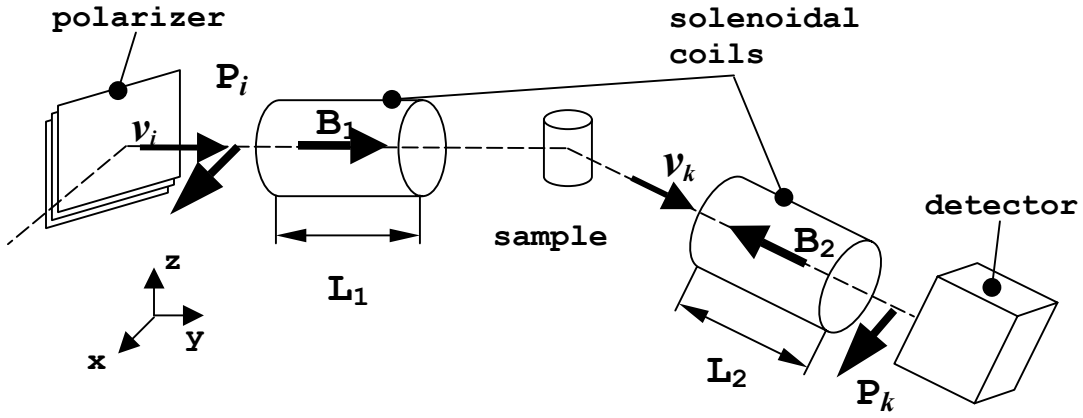

Figure 3: The schematic lay-out of a Neutron Spin Echo spectrometer.

1.2. Spin Echo for the dispersive excitations.

The dependence of the scattering function $S(\boldsymbol{q},\omega)$ not only on energy change ω, but also on momentum change $\boldsymbol{q}$ adds new features to the performing of spin echo experiments. If there is a strong dependence of the scattering function from momentum change, like in case of phonons, there is a significant spread in velocity distribution after scattering within the field B_2. This spread leads to the spread in phase φ, making the approach shown in paragraph 1.1 invalid. The way to solve this problem is given in [7]. The remedy consists in an inclination of the field borders with respect to the neutron beam axis as shown in Figure 4:

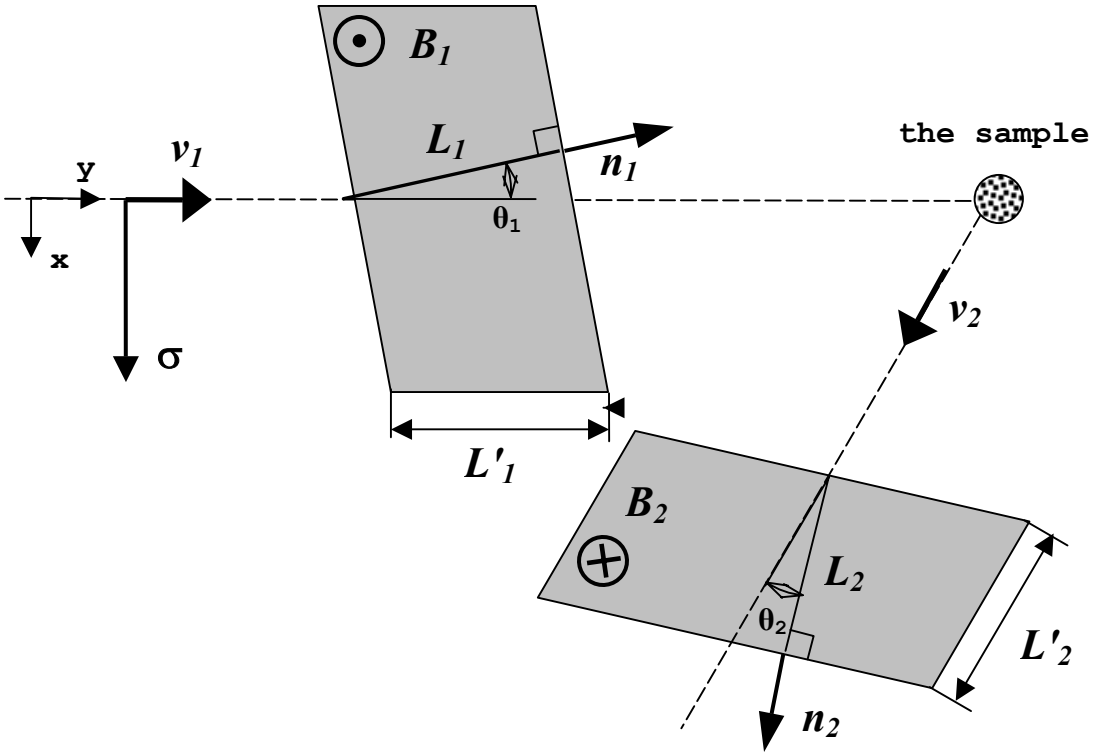

Figure 4 Schematic layout of a spin echo spectrometer with tilted precession fields. $\theta_{1,2}$ are the coil tilt angles, $\boldsymbol{n}_{1,2}$ are vectors normal to the coil surface (both surfaces of one coil are parallel), $L'_{1,2}$ are the path lengths of the neutrons in the coils while $L_{1,2}$ are the lengths of the coils perpendicular to their boundaries.

Generally, tilting of the field boundaries to get echo effect in measurements of dispersive excitations is called “spin-echo phonon focusing”.

To get spin echo signal, the Larmor phase should be proportional to the energy transfer:

$$\varphi = \omega \tau_{NSE} \tag{1.24}$$

Consider the scattering of a phonon, when the dependence of the scattering function on momentum change can be treated as:

$$S(q,\omega) = S(\omega - \omega_0(\boldsymbol{q})) \tag{1.25}$$

Here we assume that the scattering law for phonons changes insignificantly along the surface $\omega_0(q)$, but changes strongly across it. This assumption holds except for certain anomalies. The equation (1.24) becomes:

$$\varphi = (\omega - \omega_0(\boldsymbol{q}))\tau_{NSE} \tag{1.26}$$

To first order:

$$\omega - \omega_0(\boldsymbol{q}) = \omega - (\omega_0(\boldsymbol{q}_0) + \nabla_q \omega_0(\boldsymbol{q}_0)(\boldsymbol{q} - \boldsymbol{q}_0)) \tag{1.27}$$

and using:

$\omega = \frac{m}{2\hbar}(v_k^2 - v_i^2)$, $\boldsymbol{q} = \frac{m}{\hbar}(\boldsymbol{v}_k - \boldsymbol{v}_i)$, where $\boldsymbol{v}_k$ and $\boldsymbol{v}_i$ are the neutron velocities after and before scattering, we have:

$$\omega - \omega_0(\boldsymbol{q}) = \frac{m}{\hbar}((\underline{\boldsymbol{v}}_k - \nabla_q \omega_0(\boldsymbol{q}_0))d\boldsymbol{v}_k - \frac{m}{\hbar}((\underline{\boldsymbol{v}}_i - \nabla_q \omega_0(\boldsymbol{q}_0))d\boldsymbol{v}_i) \tag{1.29}$$

where $\underline{\boldsymbol{v}}_k = \boldsymbol{v}_k + d\boldsymbol{v}_k$, $\underline{\boldsymbol{v}}_i = \boldsymbol{v}_i + d\boldsymbol{v}_i$, $\underline{\boldsymbol{v}}_k$ and $\underline{\boldsymbol{v}}_i$ are the mean neutron velocities after and before scattering respectively, $\omega_0(\boldsymbol{q}_0) = \omega(\underline{v}_k, \underline{v}_i)$, $\boldsymbol{q}_0 = q(\underline{\boldsymbol{v}}_k, \underline{\boldsymbol{v}}_i)$.

According to Figure 4, the phase of the neutron spin in each coil is:

$$\varphi_{1,2} = \omega_L t_{1,2} = \frac{(\omega_L L)_{1,2}}{v_{i,k}\cos(\theta_{1,2})} = \frac{(\omega_L L)_{1,2}}{\boldsymbol{v}_{i,k}\boldsymbol{n}_{1,2}} \tag{1.30}$$

The phase after passing both fields is (by expansion in Taylor series via $d\boldsymbol{v}_i$ and $d\boldsymbol{v}_k$ to first order):

$$\begin{aligned} \varphi = \varphi_2 - \varphi_1 = \frac{(\omega_L L)_2}{\boldsymbol{v}_k \boldsymbol{n}_2} - \frac{(\omega_L L)_1}{\boldsymbol{v}_i \boldsymbol{n}_1} = \\ = \frac{(\omega_L L)_2}{(\underline{\boldsymbol{v}}_k \boldsymbol{n}_2)^2}(d\boldsymbol{v}_k \boldsymbol{n}_2) - \frac{(\omega_L L)_1}{(\underline{\boldsymbol{v}}_i \boldsymbol{n}_1)^2}(d\boldsymbol{v}_i \boldsymbol{n}_1) \end{aligned} \tag{1.31}$$

The conditions (1.26) and (1.29) are satisfied when:

$$\frac{(\omega_L L)_{1,2}}{(\underline{\boldsymbol{v}}_{i,k}\boldsymbol{n}_{1,2})^2}\boldsymbol{n}_{1,2} = \tau_{NSE}\frac{m}{\hbar}(\underline{\boldsymbol{v}}_{i,k} - \nabla_q \omega_0(\boldsymbol{q}_0)) \tag{1.32}$$

This gives the conditions for tilting of the fields boundary:

$$\boldsymbol{n}_{1,2} \;||\; ((\underline{\boldsymbol{v}}_{i,k} - \nabla_q \omega_0(\boldsymbol{q}_0)) \tag{1.33}$$

$$\cos(\theta_{1,2}) = \frac{\boldsymbol{v}_{i,k}(\underline{\boldsymbol{v}}_{i,k} - \nabla_q \omega_0(\boldsymbol{q}_0))}{|\boldsymbol{v}_{i,k}||(\underline{\boldsymbol{v}}_{i,k} - \nabla_q \omega_0(\boldsymbol{q}_0))|} \tag{1.34}$$

Also (1.32) gives the expression for the spin echo time and the condition for the field strength in both arms:

$$\tau_{NSE} = \frac{\hbar(\omega_L L)_1}{m v_i^{\,2} |\underline{\boldsymbol{v}}_i - \nabla_q \omega_0(\boldsymbol{q}_0)| \cos(\theta_1)} = \frac{\hbar(\omega_L L)_2}{m v_k^{\,2} |\underline{\boldsymbol{v}}_k - \nabla_q \omega_0(\boldsymbol{q}_0)| \cos(\theta_2)} \tag{1.35}$$

Now the expression for the final polarization can be written (remembering the approach $S(\boldsymbol{q},\omega) = S(\omega - \omega_0(\boldsymbol{q}))$:

$$< P_x >= \int d\omega S(\omega - \omega_0(\boldsymbol{q}_0)) \cos(\varphi) = \int S(\omega - \omega_0(\boldsymbol{q}_0)) \cos(\{\omega - \omega_0(\boldsymbol{q}_0)\}\tau_{NSE} + \varphi_0) d\omega \tag{1.36}$$

It represents the cosine Fourier transform of the scattering function and can be treated in a manner similar to the way described in the last paragraph.

Another point of view on spin-echo phonon focusing comes from the quantum mechanical consideration. Again consider the neutron beam, initially polarized in x direction, passing through the field region with inclined field boundaries, as shown in Figure 5.

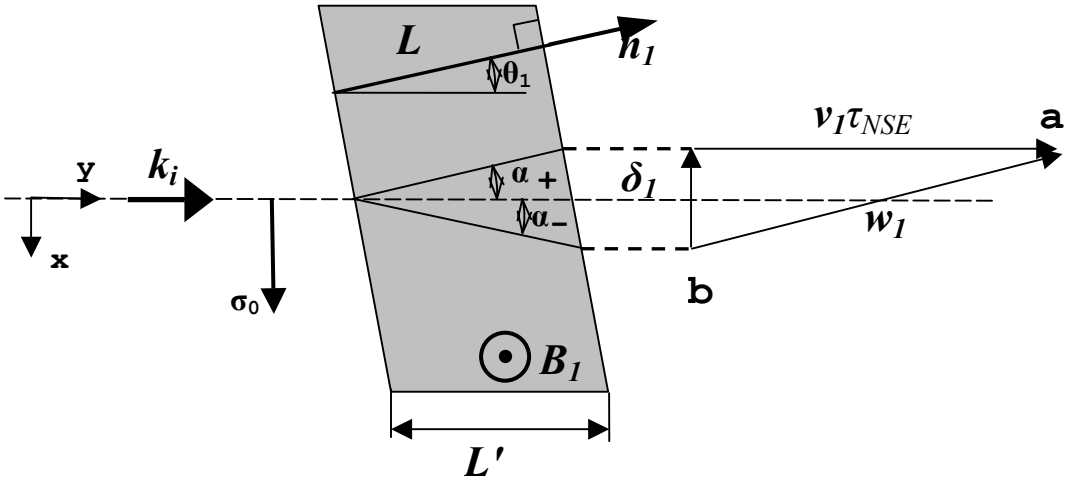

Figure 5: Trajectories of paths of the wave packets relating to the two spin states on passing a magnetic field with inclined boundary. The magnetic field splits the initial wave packet into two ones, following different trajectories, and the splitting occurs in the direction of the normal to the field boundary ($\boldsymbol{n}_1$).

As described in paragraph 1.1, the initial state, an eigenstate σ_x is a superposition of the eigenstates of σ_z:

$$|+\rangle_x = \frac{|+\rangle_z + |-\rangle_z}{\sqrt{2}} \tag{1.37}$$

On entering the magnetic field, the coherence volume is split into two coherence volumes, corresponding to two levels $\pm \boldsymbol{\mu B}$ of potential energy of the neutron magnetic moment in the static magnetic field. This splitting changes the kinetic energy (or wave vector $\boldsymbol{k_i}$) of each of the beams, corresponding to spin-up and spin-down states. To first order this splitting in k is given by

$$k_{\pm} = k \pm \frac{\hbar \omega_z}{\hbar^2 k} m \tag{1.38}$$

where $\omega_z = \mu B/\hbar = \frac{1}{2}\,\omega_L$, m is the mass of neutron.

In a magnetic field with tilted boundaries only the component of the wave vector perpendicular to the field boundary is changed accordingly to (1.38), while the component, parallel to the field boundary, remains unchanged:

$$k_{\perp} = k\cos(\theta) \pm \frac{\hbar \omega_z}{\hbar^2 k \cos(\theta)} m$$

$$k_{\parallel} = k\sin(\theta) \tag{1.39}$$

This situation leads to the fact, that wave packets of spin-up and spin down states will follow different trajectories in the magnetic field, as shown in Figure 5.

The angles of these trajectories with respect to field boundary can be calculated as following:

$$\tan(\theta_{\pm}) = \frac{k\sin(\theta)}{k\cos(\theta) \pm \frac{\hbar \omega_z}{\hbar^2 k \cos(\theta)} m} = \tan(\theta)\left(1 \mp \frac{\hbar \omega_z}{\hbar^2 k^2 \cos(\theta)^2} m\right) \tag{1.40}$$

with $\theta_{\pm} = \theta - \alpha_{\pm}$; $\alpha_{\pm}$ is:

$$\alpha_{\pm} = \pm m \frac{\hbar \omega_z}{\hbar^2 k^2} \tan(\theta) \tag{1.41}$$

On leaving the field, spin-up and spin-down wave packets will be separated not only along the y axis (as would be in case of un-tilted boundaries), but also in x direction:

$$\delta = L'(\alpha_+ - \alpha_-) = L' m \frac{2\hbar \omega_z}{\hbar^2 k^2} \tan(\theta) = \frac{2L\omega_z}{v(\boldsymbol{kn})} \tan(\theta) \tag{1.42}$$

After leaving the magnetic field, the k splitting is removed and both the wave packets will again propagate along the y axis. As derived in paragraph 1.1, there will be a time delay between both packets:

$$\tau_{NSE} = t_+ - t_- = \frac{L'}{v - \frac{\hbar\omega_z}{mv}} - \frac{L'}{v + \frac{\hbar\omega_z}{mv}} = \frac{L}{\cos(\theta)} 2\frac{\hbar\omega_z}{mv^2} = \frac{2L\omega_z}{v^3(\boldsymbol{kn})} \tag{1.43}$$

From (1.42 and (1.43) we have:

$$\delta = v\tau_{NSE}\tan(\theta) \tag{1.44}$$

Thus $\boldsymbol{w_1} = \boldsymbol{\delta} + \boldsymbol{v}\tau_{NSE}$ is parallel to $\boldsymbol{n_1}$, what is shown in Figure 5.

As in the classical discussion, consider the scattering from a phonon, taking it as a traveling excitation with velocity given by $\boldsymbol{c} = \nabla\omega_0(\boldsymbol{q})$. Figure 6 shows that at the moment when the upper spin state comes to the point $\boldsymbol{r_a}$, the other state is at $\boldsymbol{r_b}$. So if the upper state is scattered at $\boldsymbol{r_a}$ at time t_a, the lower state will be scattered on the same phonon at $\boldsymbol{r_c}$ at time t_c if $(t_c - t_a) = \tau_S$ equals the time taken for a phonon to go from $\boldsymbol{r_a}$ to $\boldsymbol{r_c}$. The time difference between these two scattering events is given by the delay between these two states.
Both packets should scatter on the same phonon. It means:

$$\boldsymbol{r}_c - \boldsymbol{r}_a \equiv \boldsymbol{c}\tau_s \tag{1.45}$$

$$\boldsymbol{r}_c - \boldsymbol{r}_b \equiv \boldsymbol{v}_1\tau_s \tag{1.46}$$

From the last two expressions we have:

$$\boldsymbol{r}_a - \boldsymbol{r}_b \equiv \boldsymbol{w}_1 \equiv (\boldsymbol{v}_1 - \boldsymbol{c})\tau_s \tag{1.47}$$

But $\boldsymbol{w_1}$ is parallel to the normal to the field boundary $\boldsymbol{n_1}$. We can write:

$$\boldsymbol{n}_1 \,||\, (\boldsymbol{v}_1 - \boldsymbol{c})\tau_s \tag{1.48}$$

Thus we have derived the first focusing condition.

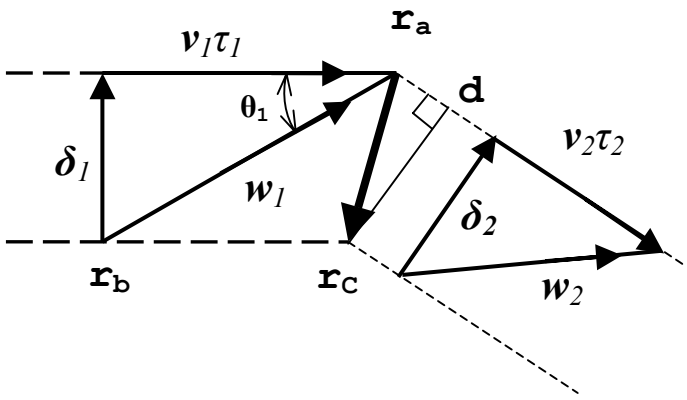

Figure 6: The relation between the paths of both wave packets before and after scattering on a phonon traveling from $\boldsymbol{r_a}$ to $\boldsymbol{r_c}$ with velocity $\boldsymbol{c} = \nabla\omega_0(\boldsymbol{q})$.

After scattering, spin-echo requires that the wave packets should interfere with each other. To get that, space and time splitting after the second coil should be removed. Looking at the packet trajectories from the analyzer (principle of reversibility), we can say that space and time splitting between spin-up and spin-down state, which could be obtained if neutrons

would travel from the detector to the sample, should be equal to the space and time splitting between them after scattering correspondingly (Figure 6). Time delay between spin-up and spin-down packets after scattering consists of the time difference between scattering events, and the time delay, coming from the fact that the packets have different position with respect to the normal to the beam trajectory. The last delay can be calculated as following:

$$\tau_{\perp} = \frac{\overline{ad}}{v_2} = \frac{1}{v_2} c\tau_s \cos(\boldsymbol{c} \wedge \boldsymbol{v}_2) = \tau_s \frac{(\boldsymbol{c}\boldsymbol{v}_2)}{v_2^{\,2}} \tag{1.49}$$

Thus the whole delay is:

$$\tau_2 = \tau_s - \tau_{\perp} = \tau_s (1 - \frac{(\boldsymbol{c}\boldsymbol{v}_2)}{v_2^{\,2}}) = \tau_s \frac{\boldsymbol{v}_2 (\boldsymbol{v}_2 - \boldsymbol{c})}{v_2^{\,2}} \tag{1.50}$$

Space splitting after scattering can be obtained as a vector difference in the following way:

$$\boldsymbol{\delta}_2 = \boldsymbol{v}_2 \tau_{\perp} - \boldsymbol{c}\tau_s = \tau_s (\frac{(\boldsymbol{c}\boldsymbol{v}_2)}{v_2^{\,2}} \boldsymbol{v}_2 - \boldsymbol{c}) \tag{1.51}$$

so that:

$$\boldsymbol{w}_2 = \boldsymbol{v}_2 \tau_2 + \boldsymbol{\delta}_2 = \tau_s (\boldsymbol{v}_2 - \boldsymbol{c}) \tag{1.52}$$

Like for the first field (in correspondence to the ray reversibility principle), $\boldsymbol{w_2}$ is parallel to $\boldsymbol{n_2}$. That means:

$$\boldsymbol{n}_2 \,||\, (\boldsymbol{v}_2 - \boldsymbol{c})\tau_s \tag{1.53}$$

what is the condition for the inclination of the second coil with respect to the optical axis. Expressions (1.48) and (1.53) are equivalent to (1.33). This shows that the conditions for obtaining the spin echo in the case of phonon focusing can be treated as the result of the requirement that the space and time separations of the two spin states satisfy the following constraints: The space time separation of the states after the first coil must be the same as the separation of two scattering events that are connected by a propagating phonon. After scattering the action of the second coil must be to cancel the space time separation which remains after the scattering and the change of direction associated with it. The approach above gives the same result as the classical one, but gives more detailed understanding of the physical reason for inclination of the field boundary in the case of measuring traveling excitations like phonons. In the literature the method of inclination of the field boundary got the name “spin-echo phonon focusing”.

1.3. Basic principle of neutron resonance spin echo.

Neutron resonance spin echo (NRSE), being a more recent variant of the spin echo principle, generally does the same as non-resonant technique: it applies to the neutron spin states some phase shift before scattering and removes it after. The change of the neutron beam polarization in an NRSE experiment describes the scattering functions in the same way as in NSE. But the principle of applying and removing of the neutron spin phase is different. NRSE is based on a combination of static and radio-frequency rotating magnetic fields – a resonance spin flipper. These fields are shown in Figure 7.

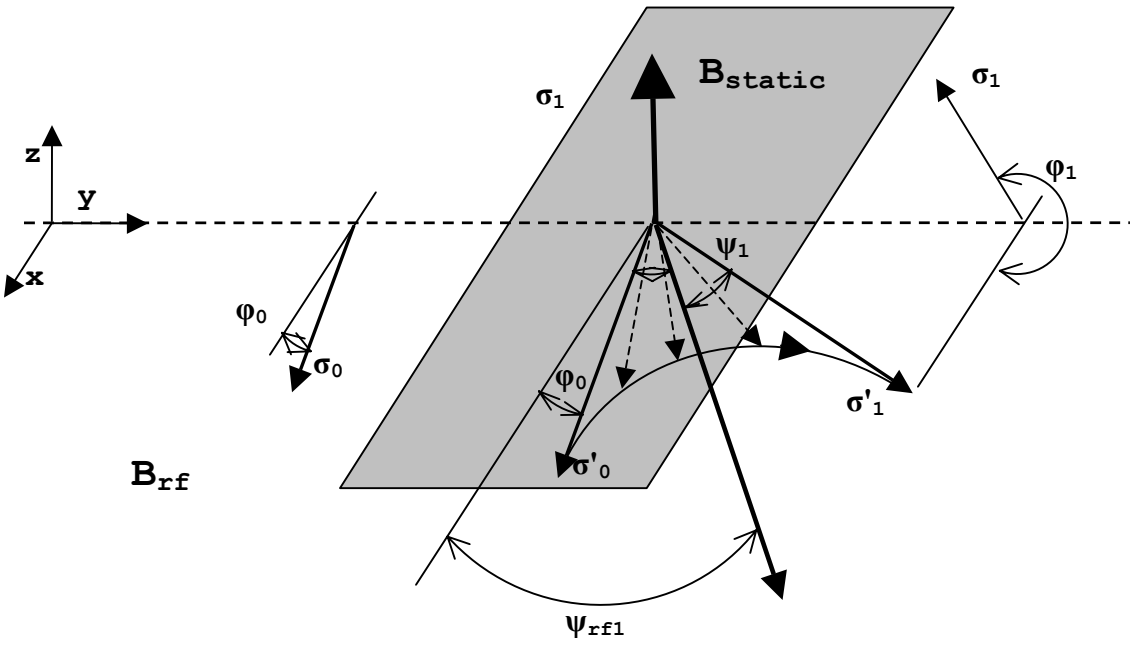

Figure 7: Working principle of the flipper.

The frequency of the radio-frequency field is adjusted to the Larmor frequency of the neutron in the static field of the flipper. Consider a neutron passing this system: coming to the active field region, it starts to precess in the static field. To see the additional action of the radio-frequency field, it is best to go into the reference system of the rotating spin.
In this system, the radio-frequency field is static, and the spin should precess around it. The field strength is adjusted to make exactly a π-turn. Making the π-turn, the spin comes back to the initial xy plane. Seen from the laboratory system, the spin precesses in addition in the static field. The precession in the static field together with the π-turn in the reference frame

of the rotating field tracks a spiral trajectory of the polarization vector with start and end in the xy plane. The resulting phase after passing the flipper is:

$$\varphi_1 = \omega_L(t_1 - t_0) + \psi_{rf1} + \psi_1 = \omega_L(t_1 - t_0) + 2\psi_{rf1} - \varphi_0 \tag{1.54}$$

where t_0 – time of coming to the flipper, t_1 – time of leaving the flipper, the angles are shown of ψ_1, φ_0, ψ_{rf1} are given in Figure 7.

After some distance L, a second identical flipper is placed (Figure 8).

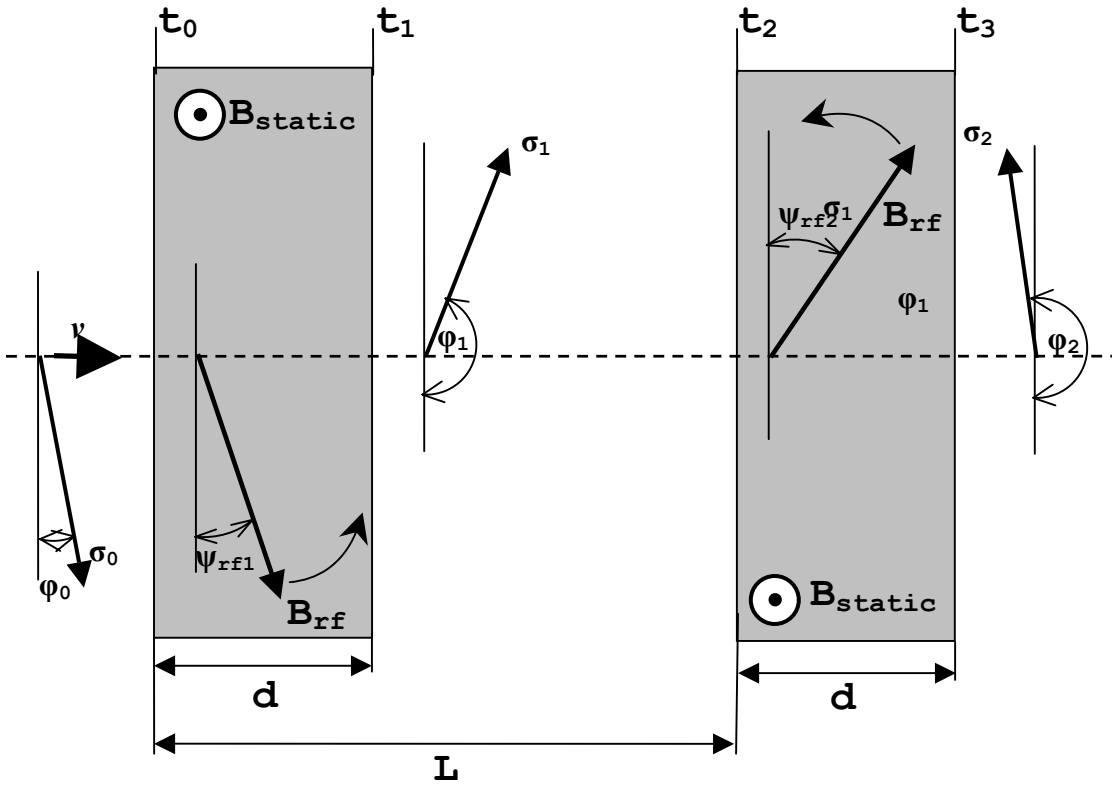

Figure 8: Operation of a system of two flippers

The rotating fields of both are synchronized (they are parallel to each other at each moment of time). During traveling of the neutron for the distance L, the angle of the rotating field becomes:

$$\psi_{rf2} = \psi_{rf1} + \omega_L(t_2 - t_0) \tag{1.55}.$$

The neutron passes the second flipper and the phase becomes (in the same manner as after the first flipper):

$$\varphi_2 = \omega_L(t_3 - t_2) + 2\psi_{rf2} - \varphi_1 \tag{1.56}$$

Substituting (1.54) and (1.55) into (1.56), and remembering that flippers have the same size ($t_3 - t_2 = d/v = t_1 - t_0$), we have:

$$\varphi_2 = \omega_L(t_3 - t_2) + 2(\psi_{rf1} + \omega_L(t_2 - t_0)) - (\omega_L(t_1 - t_0) + 2\psi_{rf1} - \varphi_0) =$$
$$= 2\omega_L(t_2 - t_0) + \varphi_0 = 2\omega_L \frac{L}{v} + \varphi_0 \qquad (1.57)$$

The spin phase change is twice as much as the phase change obtained in NSE – (1.1). It means that the system of two flippers simulates a static magnetic field of twice the static field. To remove the phase, accumulated in the first arm, after the scattering on the sample again a system of two flippers (second arm) is applied. In analogy to NSE, the second arm consists of two flippers of the same size and separated by the same distance. Static fields are of the same value as in the first arm, but of opposite direction. The direction of the rotating fields is also opposite in comparison to the flippers in the first arm.

In NRSE, rotating fields are created by oscillating fields of proper (radio) frequency. Any oscillating field can be decomposed in two counter-rotating fields. The spin flip is produced by one of these fields (of proper direction of rotation). The second field with the opposite sense of rotation only plays a second order role in the spin flip process. Rigorous solution of spin-flip problem can be found in [8], [9].

A further improvement of the NRSE technique consists in applying a pair of flip coils with static fields in opposite directions instead of a single flipper. This technique is called "bootstrap" technique. The scheme of a single arm in bootstrap technique is shown in Figure 9:

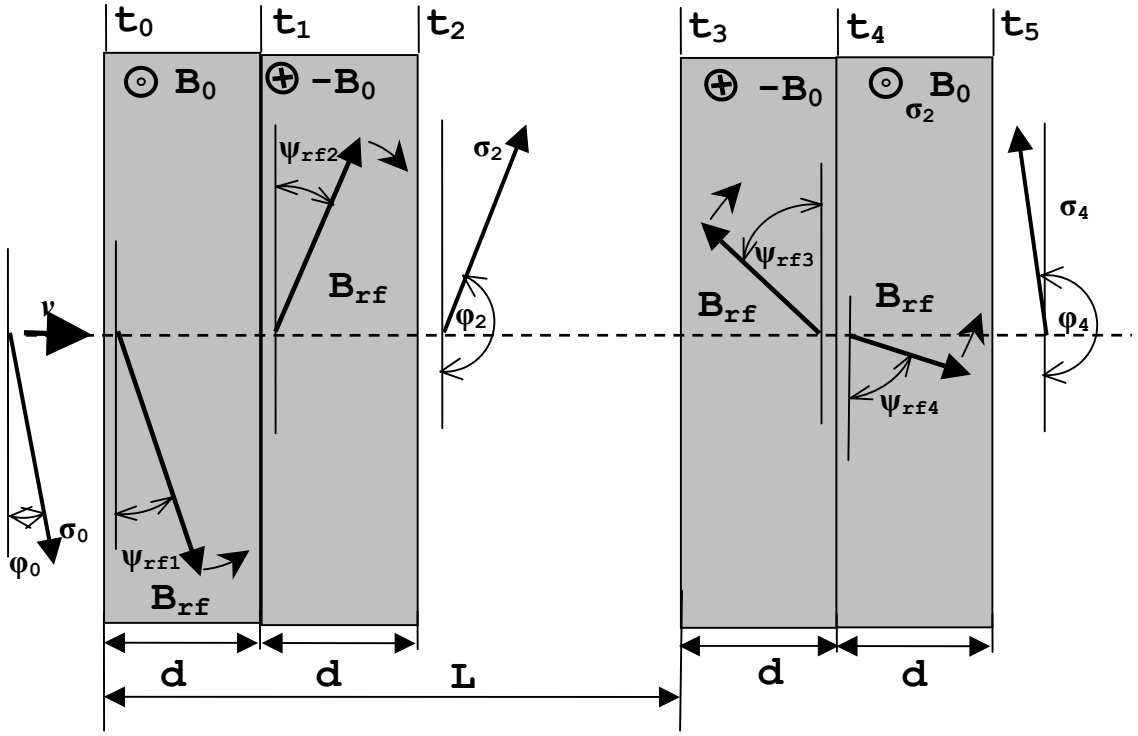

Figure 9: Principle of operation of a "bootstrap" setup of resonance flippers.

The phase of the neutron spin upon traveling through this setup can be calculated in the same manner as for the system of two flippers. After the first flipper the phase of the neutron spin is:

$$\varphi_1 = \omega_L (t_1 - t_0) + 2\psi_{rf1} - \varphi_0 \tag{1.58}$$

The neutron passes a static field of opposite direction with a rotational field in opposite sense. The angle of the rotating field is:

$$\psi_{rf2} = -(\psi_{rf1} + \omega_L (t_2 - t_0)) \tag{1.59}$$

The angle of the neutron spin is:

$$\varphi_2 = -\omega_L (t_2 - t_1) + 2\psi_{rf2} - \varphi_1 = -4\omega_L \frac{d}{v} - 4\psi_{rf1} + \varphi_0 \tag{1.60}$$

After passing the distance L, the neutron enters the third flipper. The static field points in opposite direction with respect to the first coil with corresponding sense of rotation of the RF field. The angle of the rotating field at the entering to the active area of the third flipper is:

$$\psi_{rf3} = -(\psi_{rf1} + \omega_L (t_3 - t_0)) \tag{1.61}$$

The phase of the neutron spin after the third flipper is:

$$\varphi_2 = -\omega_L (t_4 - t_3) + 2\psi_{rf3} - \varphi_2 = -2\omega_L \frac{L}{v} + 3\omega_L \frac{d}{v} + 2\psi_{rf1} - \varphi_0 \tag{1.62}$$

The fourth flipper operates with a positive static field and a corresponding rotating field. The angle of the rotating field is:

$$\psi_{rf4} = \psi_{rf1} + \omega_L (t_4 - t_0) \tag{1.63}$$

The phase of the neutron spin after the fourth flipper is:

$$\varphi_4 = \omega_L (t_5 - t_4) + 2\psi_{rf4} - \varphi_3 = 4\omega_L \frac{L}{v} + \varphi_0 \tag{1.64}$$

This is the final result for the neutron spin phase. It follows that the bootstrap technique gives a four times enhancement in the phase in comparison with standard NSE of the same static field strength. Utilization of the flipper pair has a further significant advantage in comparison to a single flipper. The field of the static coil of the flipper returns in the neutron beam area outside of the coil. This situation is shown in Figure 12 a). The presence of the field outside of the coil in the beam area significantly distorts the polarization of the neutron beam. This problem to some extent is solved in bootstrap geometry. The field from the first static coil of the bootstrap pair is guided to the second one by means of mu-

metal plates on top and bottom and a closed well defined magnetic loop is created as shown in Figure 12 b).

The flipper consists of a coil, creating a static field in vertical direction, and a coil, creating the radiofrequency field. They are shown in Figure 10. The geometry of the radio frequency field is caused by the necessity to keep its field well inside of the static field, preventing the creation of eddy currents in the windings, what would lead to large power losses.

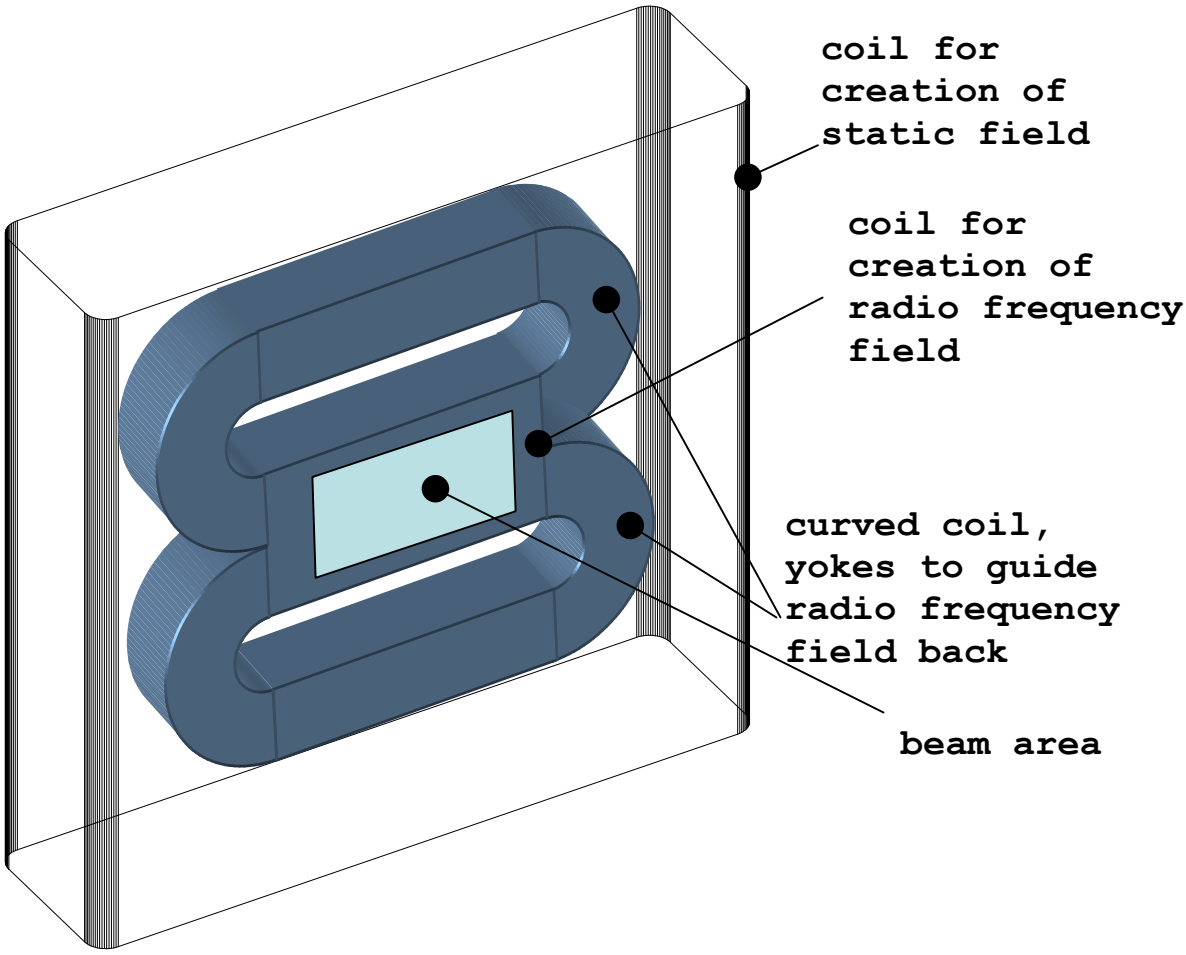

Figure 10: Lay-out of spin flipper.

A common way of coil creation consists in winding them from tape. The possibility to use wire instead of tape will be given in this thesis later on. An alterative proposal for coil manufacturing is given in Appendix B.

The other advantage of the NRSE technique is the much easier possibility for “spin-echo” phonon focusing. Here the inclination of the field can be obtained just by turning the bootstrap coil around its vertical axis, as shown in Figure 11.

The field outside of the bootstrap pair in the beam area is about an order of magnitude smaller then the field outside of the single coil in the beam area. The application of mu-metal plates further improves the homogeneity of the field inside of the coils in the beam area and further reduces the outer stray fields. Operation of the flippers (or bootstrap) is highly sensitive to external magnetic fields and special shielding from mu–metal is generally used. Details about optimization of bootstrap operation will be treated in this work in chapter 2.2.

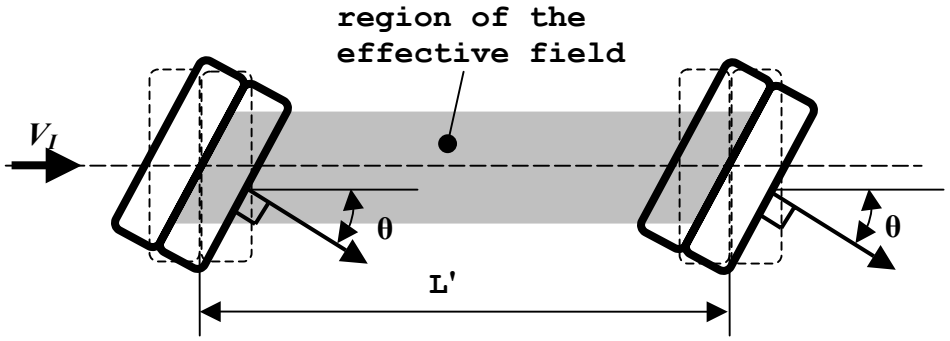

Figure 11: Inclination of the field boundaries in neutron resonant spin echo technique.

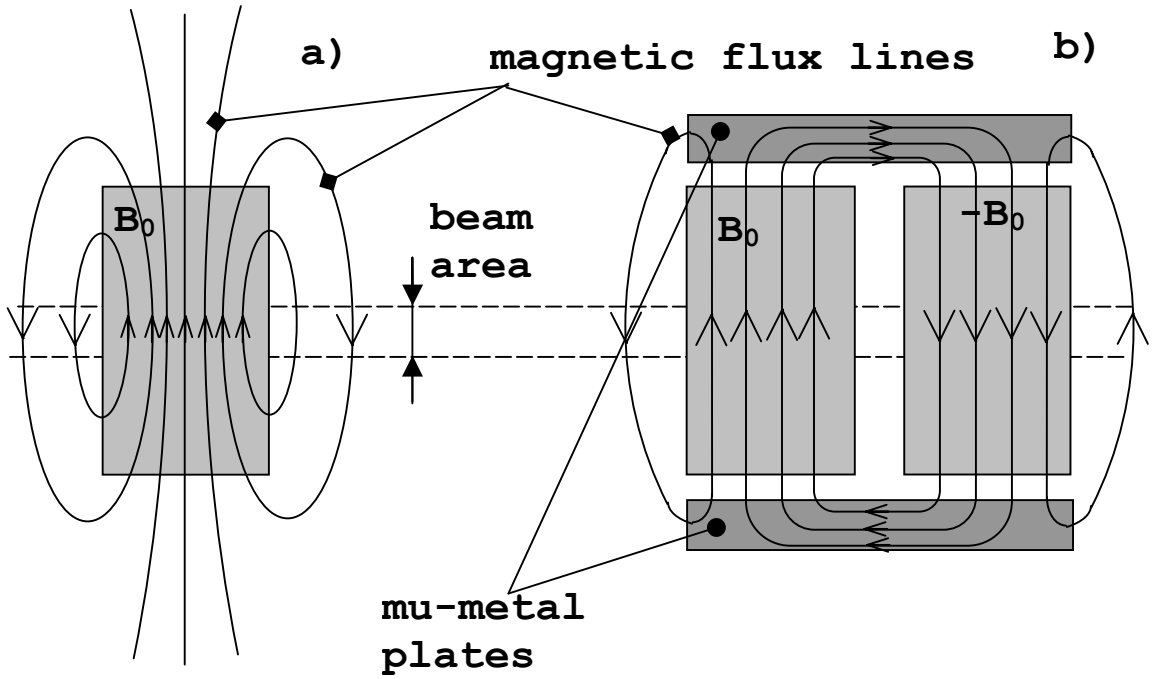

Figure 12: a) magnetic flux pattern for the static field of one flipper, b) magnetic flux pattern for the static field of a bootstrap setup.

Chapter 2.

The calculations for spin-echo coils.

2.1 The “round wire” task.

As described in paragraph 3.1, the static field of a bootstrap coil is generated by a coil with rectangular cross-section. For optimum homogeneity of the field close to the conductor, such a coil usually is wound with plane tape. For example, in case of the spin-echo spectrometer Reseda at FRM-2 [5] the coils have been wound from an aluminum tape of 8×0.5 mm. If such a coil could be wound with standard round wire, several technical difficulties in the coil production could be avoided. The problem considered in this paragraph is weather standard Al tape can be replaced by round wire without loss of polarization.

This task has been considered in the following approach: the field of a coil has been simulated in 2D, corresponding to the field in the YZ – plane (Figure 13 a)). The structure of the coil has been considered as two rows of wires - Figure 13 b), where the field of one wire is $B=4\pi\mu_0 I/r$. The current of 21 A corresponds to ~250 Gauss (what is a maximum field usually used in bootstrap mode). As neutron velocity we assume 500m/s.

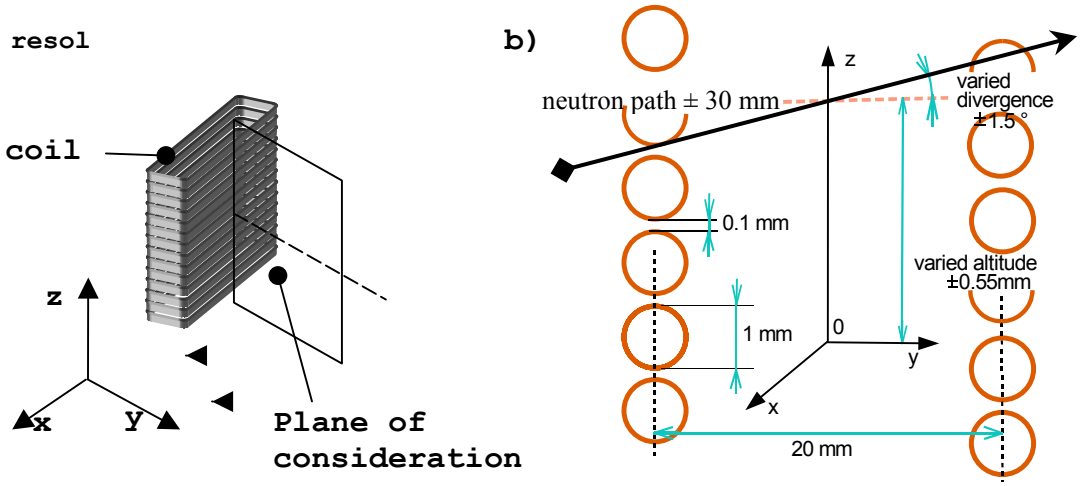

Figure 13: Possibility to use round wire. a) coil and the plane of calculations. b) model and parameters with their variational limits used in the simulation of a neutron traversing the coil.

To estimate the effect of round wire on the neutron polarization the spin rotation in the actual field is calculated. The spin turn angle has been calculated by step-by-step application of the rotation matrix along the neutron path:

$$\begin{pmatrix} \cos(\alpha)\cdot\sin^2(\varphi)+\cos^2(\varphi)\cdot(\cos^2(\theta)+\cos(\alpha)\cdot\sin^2(\theta)) & \cos^2(\theta)\cdot\sin^2(\frac{\alpha}{2})\cdot\sin(2\varphi)+\sin(\alpha)\cdot\sin(\theta) & -\cos(\theta)\cdot(\sin(\varphi)\cdot\sin(\alpha)+(\cos(\alpha)-1)\cdot\cos(\varphi)\cdot\sin(\theta)) \\ \cos^2(\theta)\cdot\sin^2(\frac{\alpha}{2})\cdot\sin(2\varphi)-\sin(\alpha)\cdot\sin(\theta) & \cos^2(\theta)\cdot\sin^2(\varphi)+\cos(\alpha)\cdot(\cos^2(\varphi)+\sin^2(\theta)\cdot\sin^2(\varphi)) & \cos(\theta)\cdot(\cos(\varphi)\cdot\sin(\alpha)+(1-\cos(\alpha))\cdot\sin(\varphi)\cdot\sin(\theta)) \\ \cos(\theta)\cdot(\sin(\alpha)\cdot\sin(\varphi)+(1-\cos(\alpha))\cdot\cos(\varphi)\cdot\sin(\theta)) & -\cos(\theta)\cdot(\cos(\varphi)\cdot\sin(\alpha)+(\cos(\alpha)-1)\cdot\sin(\varphi)\cdot\sin(\theta)) & \cos(\alpha)\cdot\cos^2(\theta)+\sin^2(\theta) \end{pmatrix} \tag{2.1}$$

which being right-hand multiplied on unit vector **x**, represents turn of this vector on angle α around direction given by spherical coordinates φ and θ. This way the calculation consisted in evaluation of the magnetic field in the point, the value of field in this point gave the angle to be put in the rotation matrix described above, and the field components gave the direction for such a turn. In the next point along the neutron path the result of spin turn at the previous point is the input for the new multiplication of rotation matrix (which is now different form the previous one as soon as the other point in space is taken).

The dependence of the outgoing spin direction on the angular divergence of the neutron path and on the shift of the path center with respect to Z coordinate (altitude) from a center of a coil has been calculated. The outgoing spin polarization P has been estimated as mean projection of the X-Y spin components on a mean direction of these components.

$$P = \frac{1}{N}\sum_{i=1}^{N}(\boldsymbol{\delta}_i \langle \boldsymbol{\delta} \rangle) \tag{2.2},$$

where N is the number of trajectories considered in simulation (N~1000), $\langle\boldsymbol{\delta}\rangle$ is the mean spin direction estimated as:

$$\boldsymbol{\delta} = \frac{1}{N}\sum_{i=1}^{N}\begin{bmatrix}\delta_x \\ \delta_y\end{bmatrix} \tag{2.3}$$

For a wire of 1 mm diameter the polarization was P = 0.987 (what was just at a limit of calculation precision).This is the result after one coil. The final effect can be estimated as [10]:

$$P_{final} = P_{one\_coil}^{\sqrt{8}} \tag{2.4}$$

$\sqrt{8}$ represents the statistical average after passing 8 coils of static field, what corresponds to the standard NRSE setup (paragraph 1.3). For a wire of 1 mm diameter the final polarization was 0.963. This shows that wire of 1 mm diameter can be used to build static coils for the bootstrap setup. It is quite important to note that the value of the final polarization is not considerably varied by small randomizations of wire positions, which was done by applying a statistical variation of the position of the wires (amplitude of Z variation is 0.05mm, amplitude of variation Y is 0.01mm).

2.2 Optimization of the bootstrap performance.

Independent of the shape of the conductor used for the static coils, neutrons spins are affected by unavoidable stray fields, created by leakage of field mostly from the static coils. Because of this fact the behavior of the neutron spins outside of the active field region has been explored for the complete geometry of a bootstrap coil in 2D approach. Top and bottom mu-metal plates play a main role, they guide the magnetic flux of one coil into the second one, keeping the magnetic flux from going through the beam region outside of the coils.

To simulate the behavior of mu-metal in magnetic field the ANSYS 5.4 [11] commercial finite element method [12] code program has been used. To limit computing time only the upper half of a bootstrap has been considered. Due to the symmetry, the „flux perpendicular to boundary“ boundary condition had been applied. The bootstrap geometry considered in simulations and a typical picture of the field is shown in Figure 14.

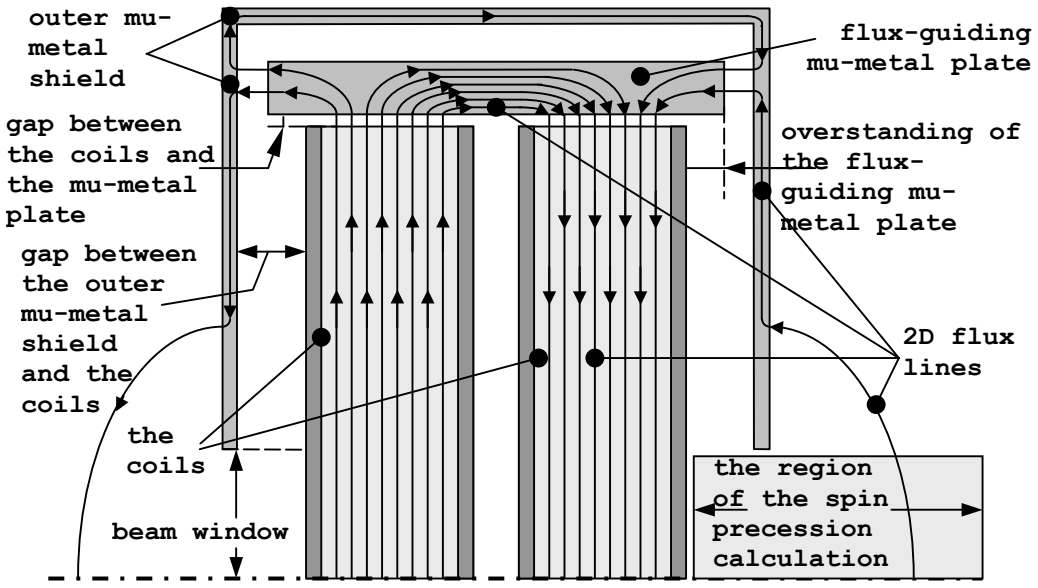

Figure 14: The section view of a static field pattern of the bootstrap setup. The region of calculation is shown.

The spin precession was calculated in the region outside of the coil in the beam area, on one side of the bootstrap. The magnetic field values for calculation of the precession angle were taken from the ANSYS program. The spin precession has been calculated as a function of altitude (0-20mm) in the beam window and for a divergence angle of 0-1.5°. The

precession angle and the polarization have been averaged over the considered range of altitude and angle. The final polarization (after 4 pairs of bootstrap coils) was estimated by means of equation (2.4). The calculations have been done for the monochromatic neutron beam of 500m/s neutron velocity.

As the mu-metal plate plays the key role in guiding the magnetic flux between the coils, there was the idea that increasing of thickness of the plates might reduce the leakage of the field into the outer space of the coils. The simulations of geometry shown in Figure 14 with different thickness on the plate have been done. The results of them are summarized in Table 1.

Table 1: Variation of mu-metal plate thickness without outer mu-metal shield.

Plate thickness, mm.	Spin turn due to the outer field, degrees.	Polarization after passing the region of calculations (Figure 14).	Final polarization after passing of four bootstrap coils.
2	259	0.99	0.99*
3	254	0.99	0.99*
4	255	0.99	0.99*

The data of Table 1 tell that a change of mu-metal plate thickness does not change the field in the beam region in the outer space of the coil. Another parameter, which was varied is the gap between the outer mu-metal shield and the bootstrap coil. The results of this variation are given in Table 2.

Table 2: Variation of gap between coils and shield (see Figure 14). The thickness of the shield is 0.1 mm.

Gap, mm.	Spin turn due to the outer field, degrees.	Polarization after passing the region of calculations (Figure 14).	Final polarization after passing of four bootstrap coils.
5	135	0.89	0.73
10	72	0.98	0.95
15	39	0.99	0.99

Table 2 shows that the efficiency of the outer field increases significantly with distance of the shield from the coil. This is an important result for the design of the coil
Then the shield thickness was varied, the results are shown in Table 3.

Table3: The shield thickness is varied. The gap between coil and shield is 10 mm. Mu-metal plate thickness is 4 mm.

Shield thickness, mm.	Spin turn due to the outer field, degrees.	Polarization after passing the region of calculations (Figure 14).	Final polarization after passing of four bootstrap coils.
0.1	72	0.98	0.95
0.5	6.5	0.99	0.99*
1.0	5.7	0.99	0.99*

Here one can see a significant reduction of the field when the shield thickness is increased up to 0.5mm from 0.1 mm. This drastical improvement certainly arises from partial saturation of the shield at 0.1 mm thickness. The saturation for mu-metal means that it can not guide the full magnetic flux (Appendix A).

Calculations for the spin precession were done for the case when the top (and from symmetry reason bottom) mu-metal plate exceeds the coil pair cross-section to the sides along the optical axis as it is shown in Figure 14. Simulations for such a configuration have been performed without considering the outer mu-metal shield, in order to obtain more clearly distinguishable effects. The results of these simulations show that in the case when the mu-metal plates overstand the coils by 2-4 mm the spin turn is two times smaller then without overstanding.

The results of the simulations described in this paragraph can be concluded as follows: one should avoid situations when the mu-metal becomes saturated. The mu-metal shield of the bootstrap serves not only to protect from external field, but also greatly reduces field leakage from the coils to the beam area outside the coil. By choice of proper geometry of the mu-metal plates and the outer shields, nearly perfect coils can be produced.

---

* means that calculations show that the neutron beam polarization after passing region of calculations is not changed in frame of the available numerical precision (it is nearly 1), and the calculation of the final polarization doesn't give any additional information ($1^x = 1$).

Chapter 3.

The design study of multi angle neutron resonance spectrometer.

3.1. MIEZE-2 principle and basic concept of multi angle spin-echo spectrometer.

The next generation of spin-echo instruments will be equipped with multi angle analysis units. Here we design the first multi angle instrument with π/3 angular range and high resolution (20 – 50 ns spin-echo time). It is based on the MIEZE-2 principle (Figure 15), and the dependence of the phase of the spin states on the detector from the change of the neutron momentum can be derived is this paragraph. The other version of MIEZE technique is MIEZE-1, which is thoroughly explained in [4].

We follow the presentation given in [13], taking Planck constant $\hbar$ as equal to one. The propagation operator for the wave function downstream of the flipper reads now:

$$\hat{O}_{flipper} = \begin{pmatrix} 0 & e^{-2i\Delta k y} e^{2i\Delta\omega t} \\ e^{2i\Delta k y} e^{-2i\Delta\omega t} & 0 \end{pmatrix} \qquad (3.1)$$

where $\Delta k = k_0 \cdot \gamma B / 2E_0$, $\Delta\omega = \gamma B/\hbar$, k_0 and E_0 are the momentum and the energy of the neutrons correspondently, and B is the static field in the flipper.

For a single bootstrap such a propagator can be obtained by subsequent multiplication of two operators like (3.1) (with the reversed sign of the exponent of the second multiplier):

$$\hat{O}_{bootstrap1} = \begin{pmatrix} e^{4i\Delta k_1 y} e^{-4i\Delta\omega_1 t} & 0 \\ 0 & e^{-4i\Delta k_1 y} e^{4i\Delta\omega_1 t} \end{pmatrix} \qquad (3.2)$$

where $\Delta k_1 = k_1 \cdot \gamma B_{z1} / 2E_1$, $\Delta\omega_1 = \gamma B_{z1}$, k_1 and E_1 are the momentum and the energy of the incoming neutrons correspondently. B_{z1} is the field of the first bootstrap. For the second bootstrap at the distance L_1 from the first one the propagator can be written as:

$$\hat{O}_{bootstrap2} = \begin{pmatrix} e^{-4i\Delta k_1 y} e^{4i\Delta\omega_1 t} & 0 \\ 0 & e^{4i\Delta k_1 y} e^{-4i\Delta\omega_1 t} \end{pmatrix} \qquad (3.3)$$

where $\Delta k_2 = k_1 \cdot \gamma B_{z1} / 4E_1$, $\Delta\omega_2 = \gamma B_{z1}$, k_1 and E_1 are the momentum and the energy of the incoming neutrons respectively. B_{z1} is the field of the second bootstrap (which is the same as in the first one).

After the first arm the wave function is now:

$$\Psi_{arm1} = \hat{O}_{bootstrap2}\hat{O}_{bootstrap1}\Psi_0 \qquad (3.4)$$

where Ψ_0 is the initial state (see equation (1.18).

For the third bootstrap of the MIEZE-2, which is situated after the sample, the propagation operation reads as:

$$\hat{O}_{bootstrap3} = \begin{pmatrix} e^{-4i\Delta k_3 y} e^{4i\Delta\omega_3 t} & 0 \\ 0 & e^{4i\Delta k_3 y} e^{-4i\Delta\omega_3 t} \end{pmatrix} \qquad (3.5)$$

where $\Delta k_3 = k_2 \cdot \gamma B_{z2}/2E_2$, $\Delta\omega_3 = \gamma B_{z2}$, k_2 and E_2 are the momentum and the energy of the scattered neutrons correspondently. B_{z2} is the field of the third bootstrap (the fields in the second and the third bootstraps are equal in MIEZE-2). The multiplication of the (3.5), (3.4), (3.2) gives the wave function downstream of the third bootstrap:

$$\Psi_3 = \begin{pmatrix} e^{4i\left[-\Delta k_3 y + L_1(\Delta k_2 + \Delta k_3)\right]} e^{4i\Delta\omega_3 t} & 0 \\ 0 & e^{-4i\left[-\Delta k_3 y + L_1(\Delta k_2 + \Delta k_3)\right]} e^{-4i\Delta\omega_3 t} \end{pmatrix} \Psi_0$$

$$\Psi_3 = \hat{O}_{space}\hat{O}_{time}\Psi_0 \qquad (3.6)$$

where:

$$\hat{O}_{time} = \begin{pmatrix} e^{4i\Delta\omega_3 t} & 0 \\ 0 & e^{-4i\Delta\omega_3 t} \end{pmatrix} \qquad (3.7)$$

$$\hat{O}_{space} = \begin{pmatrix} e^{4i\left[-\Delta k_3 y + L_1(\Delta k_2 + \Delta k_3)\right]} & 0 \\ 0 & e^{-4i\left[-\Delta k_3 y + L_1(\Delta k_2 + \Delta k_3)\right]} \end{pmatrix} \qquad (3.8)$$

From (3.6),(3.7), (3.8) one can say that after third flipper there are time beats with frequency $\omega_4 = 4 \cdot \Delta\omega_3$. The phase of them is defined by exponential term in (3.8). At position L_2 after the third coils (where the detector suggested to be) the phase will be:

$$\varphi_3(k) = 4\left[-\Delta k_3 L_2 + L_1(\Delta k_2 + \Delta k_3)\right] \qquad (3.9)$$

taking into account expressions for Δk_3 , Δk_2 , Δk_1 one could have:

$$\varphi_3(k) = 4 m \gamma \left(B_2 \left(\frac{L_1}{k_1} - \frac{L_2}{k_2}\right) + \frac{L_1}{k_2} B_2 \right) \qquad (3.10)$$

In the basic concept of MIEZE-2, the lengths of the first and the second arm are equal and the fields in all bootstrap coils are set to be equal:

$$B_1 = B_2 = B \,,\; L_1 = L_2 = L \qquad (3.11)$$

In this case $\varphi_3(k)$ on the detector reduces to:

$$\varphi_3(k) = 4m\gamma \frac{BL}{k} \qquad (3.12)$$

and detector will see the beats of polarization of frequency $4\gamma B$. In the case of the quasielastic scattering, that means $k_2 = k_1 \pm \Delta k$, $\Delta k << k_1$, we can differentiate the equation (3.12) and receive the change of the polarization from small change of the neutron momentum:

$$\Delta\varphi = 4m\gamma \frac{BL}{k^2}\Delta k \qquad (3.13)$$

or remembering that $k = mV/\hbar$, and $\Delta V = \Delta E/mV$, where ΔE is the energy transfer in the scattering it reads:

$$\Delta\varphi = 4\frac{\gamma BL}{mV^3}\Delta E \qquad (3.14)$$

The equation (3.14) coincides with the basic equation of the spin echo spectroscopy (1.6).

Compared to NRSE, MIEZE-2 does not need a large magnetic screen downstream of the sample, and, similar to NSE and NRSE, it allows the use large samples without loss of resolution. Actually, the MIEZE-2 signal does not depend on the position of the analyzer with respect to the position of the third bootstrap coil. This gives the possibility to place the analyzer very close to the third bootstrap coil.

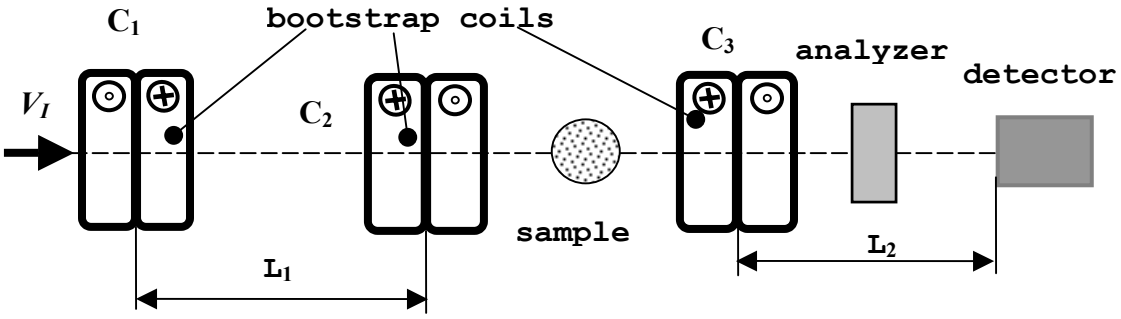

Figure 15: The lay-out of the MIEZE-II spectrometer. The distance from C_3 to analyzer is arbitrary*.

---

* for this fact see [3], page 192.

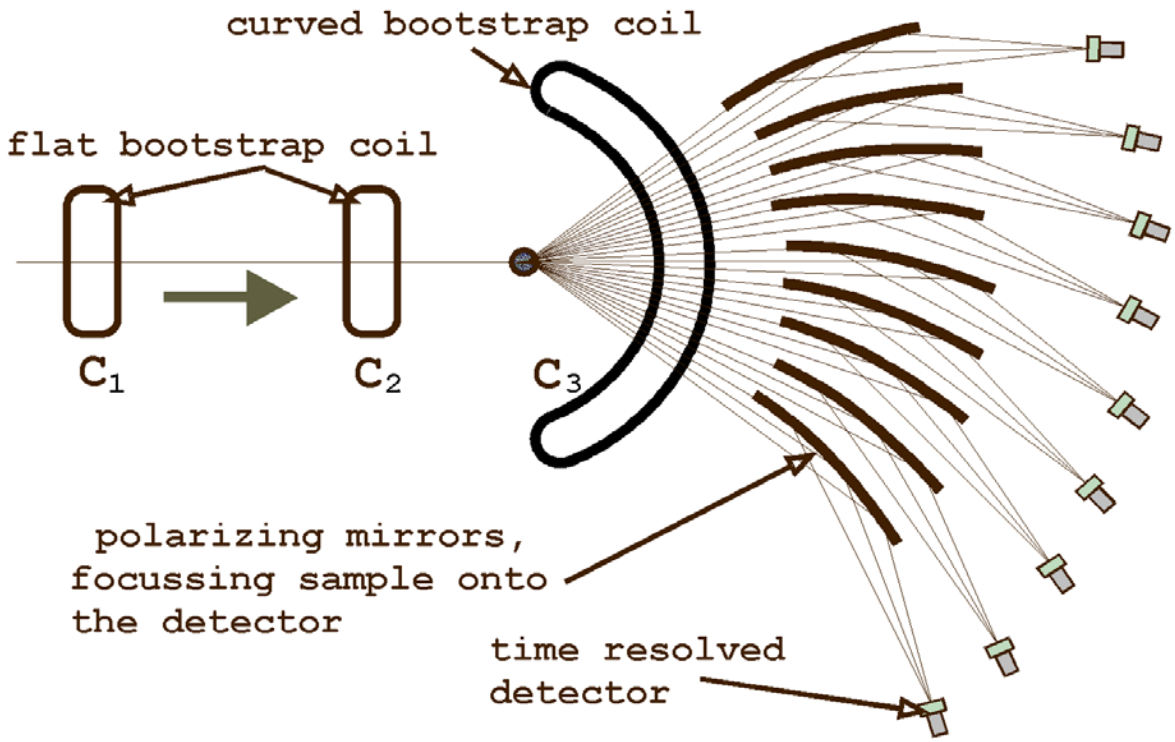

Figure 16: The lay-out of a multi angle MIEZE-2 spectrometer. The curved bootstrap coil (the static field is perpendicular to the plane of the drawing, the RF field in the plane of the drawing) represents the third bootstrap coil of a standard NRSE-instrument. The polarizes also serve as focusing mirrors and minimize path length differences from the sample to the detector. Magnetic screening is necessary between the first bootstrap C_1 and the curved bootstrap coil. Here we assume a range of $\pi/3$ for the analysis of the scattered neutrons. A near 2π range could be analyzed by using an annual coil for C_3, which serves as C_2 coil as well.

The major advantage of the MIEZE-2 principle is the possibility to measure neutron scattering at different scattering angles at the same time (multi angle measurements). The lay-out of multi angle MIEZE-2 spectrometer is given in Figure 16.

In the design of this spectrometer the following problems had to be studied:

1) The neutron paths focusing by elliptical mirrors, path length homogeneity.
2) The operation of the curved coil for the creation of the static field.
3) Operation of the curved coil for the creation of the radio frequency field.

The following paragraphs are devoted to these problems.

3.2. Optical ray tracing.

The MIEZE –2 principle demands high constancy of the length of all neutron trajectories between coils C_1 and C_2, as well as between C_3 and the detector. Their variations must be small compared to $<v \cdot T_{RF}>$, where v is the velocity of the neutron and T_{RF} is the period of the RF-frequency of the flipper. The lengths of the neutron paths in the situation when the sample has infinitely small size and the shape of mirrors is perfect must be equal because of Fermat's principle. Drawbacks of deviation of supposed experimental setup from ideal one and remedies to these drawbacks that have been estimated will be described in this chapter. The expected sources of problems are following:

1) The polarizing supermirrors should focus in two dimensions. The required micro-roughness of <10 Å is difficult to achieve at moderate costs.
2) Path lengths have to be calculated from the curved bootstrap coil up to the detector (in correspondence to the MIEZE-2 principle), but not from the sample (what corresponds to Fermat's principle). The last factor will definitely cause some difference in path lengths.
3) The sample has some finite size what can cause additional problems with focusing and path length homogeneity.

For qualitative estimation of the above errors ray – tracing simulations have been done. The simulations are based on the geometry shown in Figure 17. For this task an original code has been written in Mathematica. This code computes the path length directly, without using the lens equation [14].

Computations have shown that there will be no significant difference whether one uses spherical or elliptical mirrors. Using of spherical mirrors gives an non-homogeneity in path lengths of value $\sim 1*10^{-6}$ m, what is far below the limit of precision of polarizing supermirrors manufacturing. But using spherical mirror makes ray focusing significantly worse. The distribution of the intensity on the plane of the detector in the case of using spherical mirrors is given in Figure 18. Nevertheless utilization of a 1.5 inch detector allows to gather the whole intensity. The further estimations have been made for a spherical mirror. The paths of neutrons from the bootstrap coil to the detector vary by a value of $\sim 5 \cdot 10^{-6}$ m, what is small enough to get the MIEZE-2 signal.

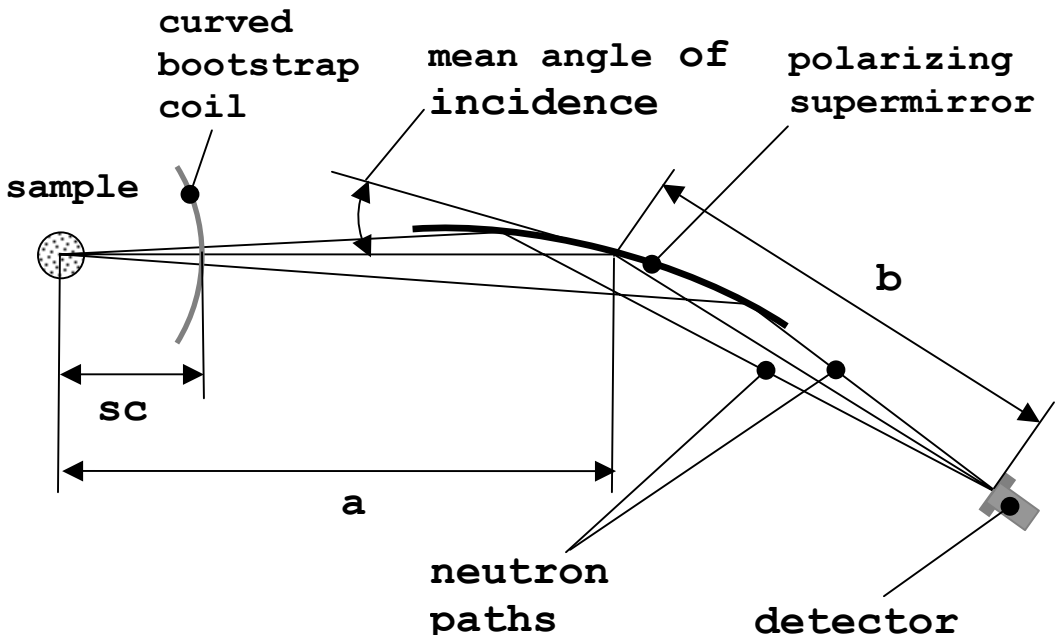

Figure 17: Scheme of the optical system, which has been used as a base for optical ray-tracing simulations in the design of a multi angle MIEZE-II spectrometer. The distance from the sample center to the mirror (**a** in Figure 21) is 2 m. The distance from the sample to the curved bootstrap (**sc** in Figure 21) is 0.5 m. The radius of the mirror is 100 m, its length is 1.2 m. The angle of incidence on the mirror is 1.5°. Here we assume a polarizing supermirror with m = 2.5 and a wavelength range 6-15 Å. The distance from mirror to the detector is (**b** in Figure 21) 2 m. The sample has 1 cm radius.

Based on these parameters the variations of the coil position, the inclination of the coil with respect to the optical axis, and the variation of the coil profile from flat to curved have been done in simulations and they gave no satisfactory path length homogeneity. Actually, the fact that the path length is calculated from the coil to the detector saves the situation from the one when the path length is calculated from the sample to the detector. The last would give path length differences comparable to the sample size, what would make the application of the MIEZE-2 principle impossible.

The finite size of the sample this way only causes second order distortion. In case of a sample size of 1cm, the path length difference remains approvable ($5 \cdot 10^{-6}$ m), for 2 cm size, path length difference reaches a value of $1 \cdot 10^{-5}$ m.

To optimize the optical system, the variation of the detector position and the tilting with respect to the optical axis and has been analyzed. The optimum position for the detector is at the nominal focus of the system, perpendicular to the optical axis.

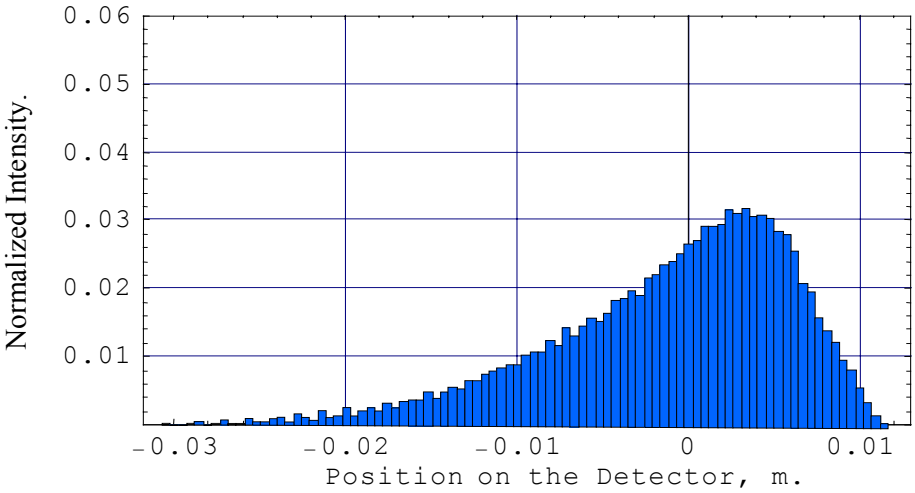

Figure 18: Expected lateral distribution of the intensity on the detector. The optical axis is at zero.

The results of optical ray-tracing computations, given above, show that the performance of the optical system allows to use it for experiments based on the MIEZE-2 principle. A signal, which one could expect to see on the detector, is shown in Figure 19. As we see, the path length differences do not cause any significant loss of contrast at $\omega = 10^6$ s^{-1}.

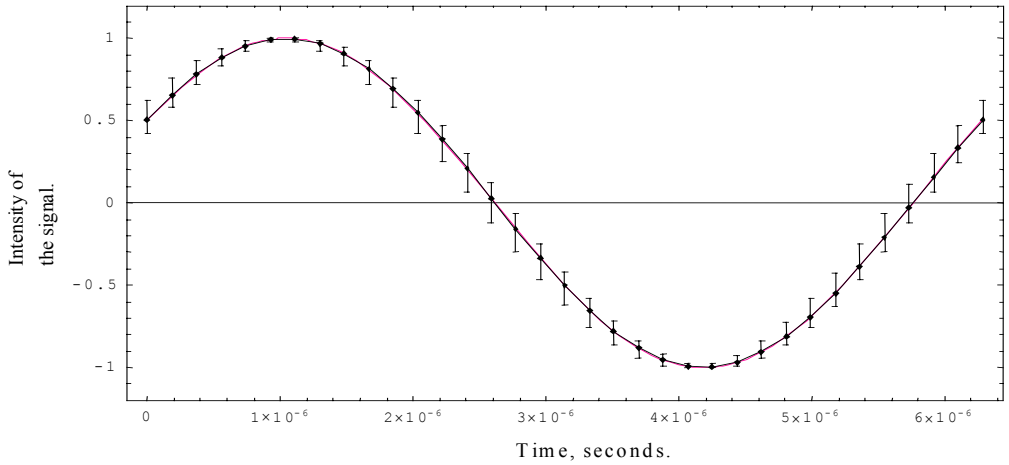

Figure 20: An expected MIEZE–2 signal for neutrons of 500 m/s and for the frequency of 10^6 s^{-1}. Error bars represent expected value of error due to the path length inhomogeneity.

3.3 Static field coils for curved bootstrap.

The annual shape of the static field coils for the curved bootstrap coil is based on the from the idea of a multi angle spin-echo spectrometer and its scheme is drawn in Figure 21.

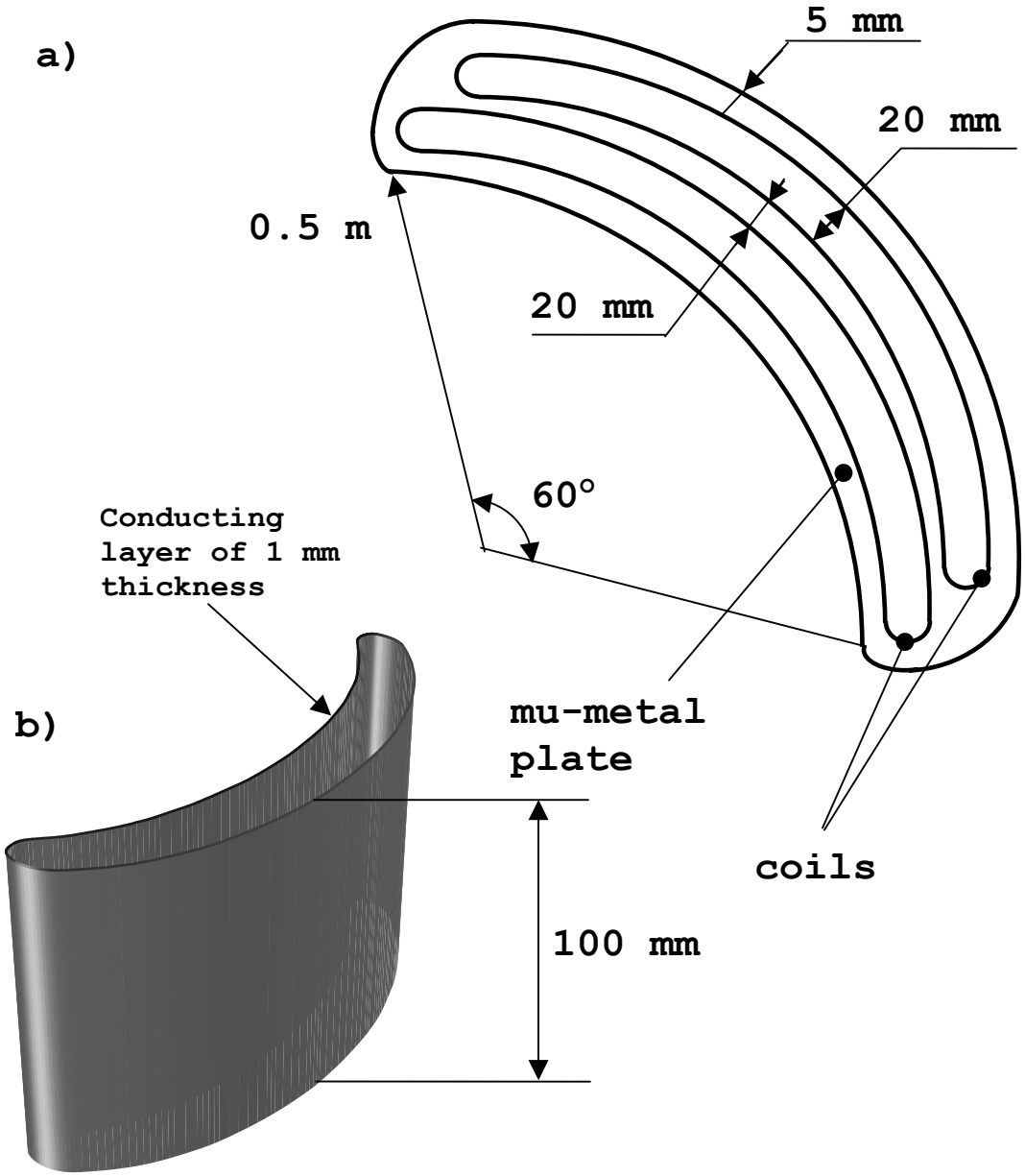

Figure 21: a) top view of static coils of the curved bootstrap (not to scale). Mu-metal plates of 4 mm thickness are applied on top and bottom of the coils. b) 3D view of static field coil of the curved bootstrap (not to scale).

The static field coils are identical and have the same shape and area. The difference of radial geometry is negligible. The coils of shown geometry have been simulated with the aid of Amperes [15] commercial Boundary Element Method (BEM) code (the detailed description of it can be found in Appendix C). All simulations have been done for a current 21 A, corresponding to the maximum field value of 250G. There are two points were the performance of the coil has to be evaluated. It is a field inside of the coil, which should be homogenous enough to make a proper spin flip, without significant loss of polarization. The second problem is the field outside of the coil, which should not cause distortion of the polarization.

As for the field inside of the coils, BEM calculation has shown some increase field strength from the outer sides of the coil to the inner ones. This dependence is shown in Figure 22.

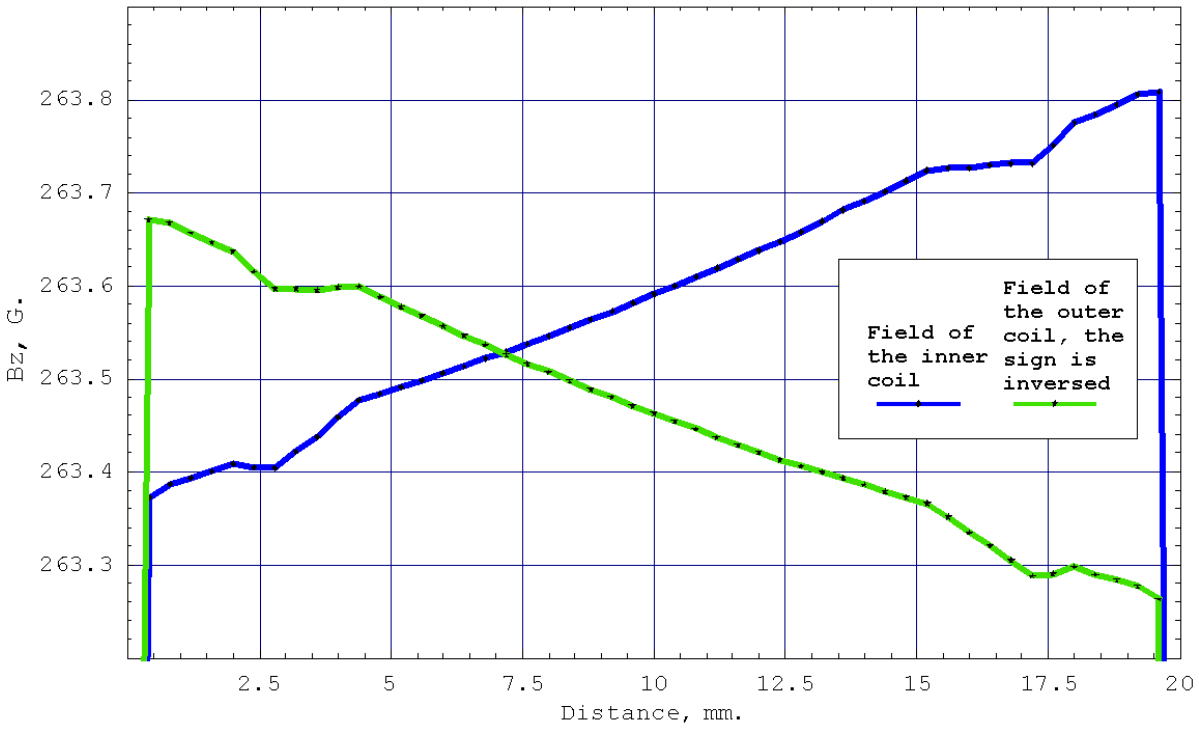

Figure 22: The static field in the curved bootstrap coil, inner and outer coil. On the x axis, the distance means a distance in the coil along the symmetry axis. The field of the outer coil is negative and is given on the figure with reversed sign in order to compare it with the field in the inner coil. Deviations from the linear shape near the ends are artificial and caused by some features of the numerical method [15].

Figure 22 represents the radial field dependence along the main optical axis. The angular field dependence is very small and can be neglected here, i.e. the field inside of

curved coils is homogeneous enough and further discussion on the static field of the curved bootstrap coil will be on the field values along the optical axis.

These dependences have been compared with ones of a flat bootstrap coil (Figures 23, 24, like being used at the working NSRE machine in Saclay [16] or Berlin [17]. The performance on these two spectrometers is well proven and can serve as a reference. The inner and the outer coils of curved bootstrap are not symmetrical and should be considered separately.

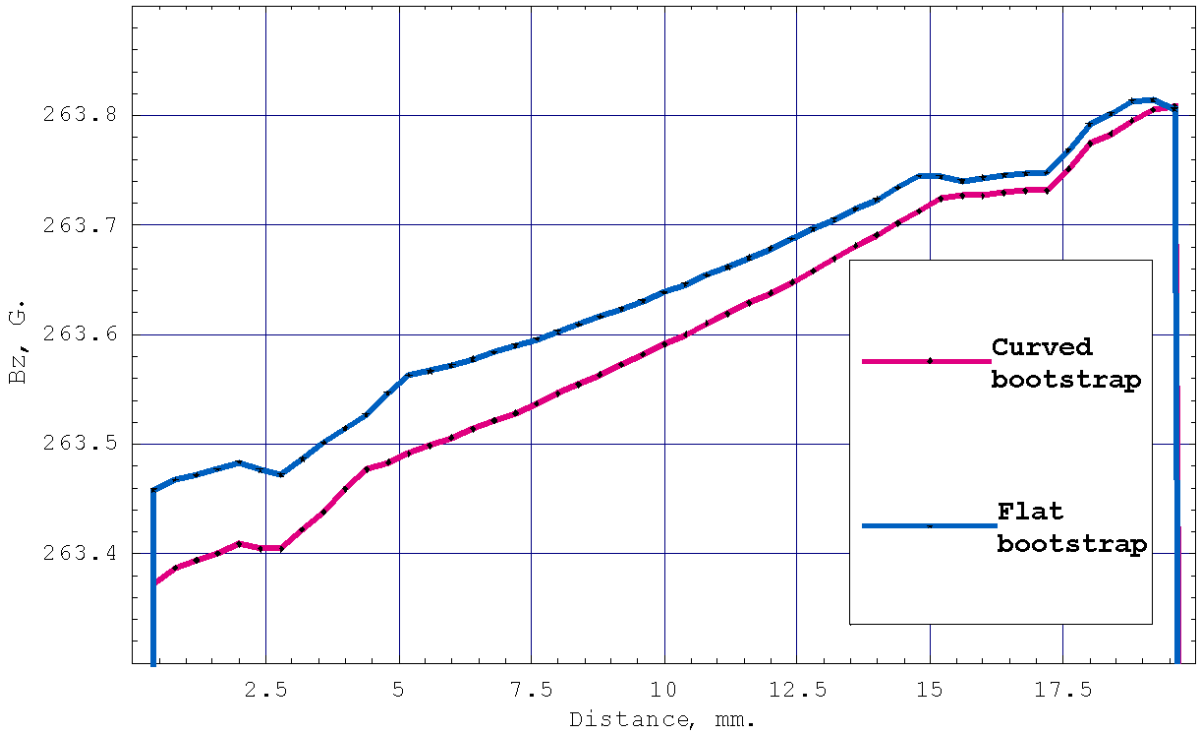

Figure 23 Comparison of the static fields in curved and flat bootstrap coil, for the curved one – the inner coil is taken. The distance is taken along the symmetry axis. The curves are close to coincide.

The field dependence shown in Figure 22 shows that the field of the inner coil is a little bit bigger than the field in the outer one. The field inside of curved coils is practically the same as in case of flat ones. For the curved bootstrap coil (with smoothing of artificial hills near the ends of the curves) direct simulations on the spin flip have been done. The result of them is that the reduction of the magnetic field toward the outer sides of the curved bootstrap coil have no effect at all on the process of spin flip. The slight difference in magnitude between fields in inner and outer coils also make no effect.

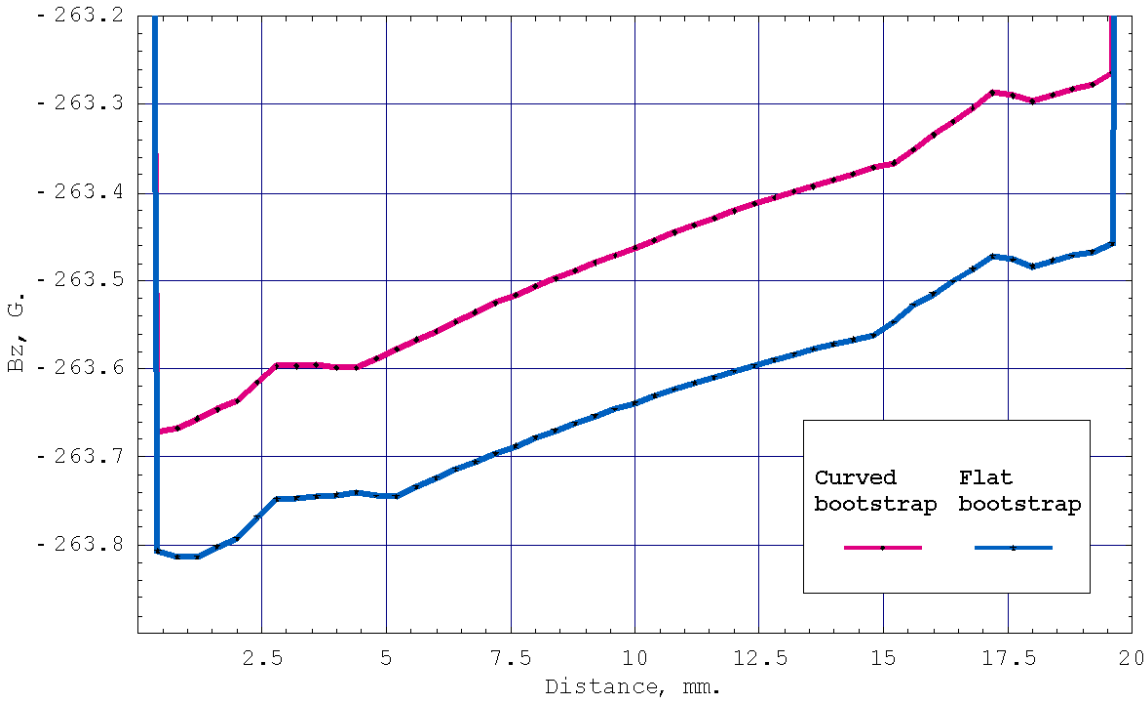

Figure 24 Comparison of static field in curved and flat bootstrap, for curved – outer coil is taken. The distance means a distance in the coil along the symmetry axis. The curves are close to coincide.

The field outside the coils and its influence at the polarization of the neutron beam has been estimated. Simulations have shown an empirical rule: the field outside of the coil in the outer part of space with respect to the coil curvature is never bigger then or the same as in the inner part of the outer space – Figure 25 This way, if the field in the inner part of the coil is good enough, the field in the outer part will be good also. On the next Figure 36 the static field outside of the bootstrap is shown. The gap between coils and mu-metal plates in this case is 4 mm (what is standard in bootstrap manufacturing). From Figure 36 two conclusions could be drawn. The first – application of the shield reduces the field integral significantly (approximately twice). The second - the field from the curved bootstrap is smaller then the field from the flat bootstrap.

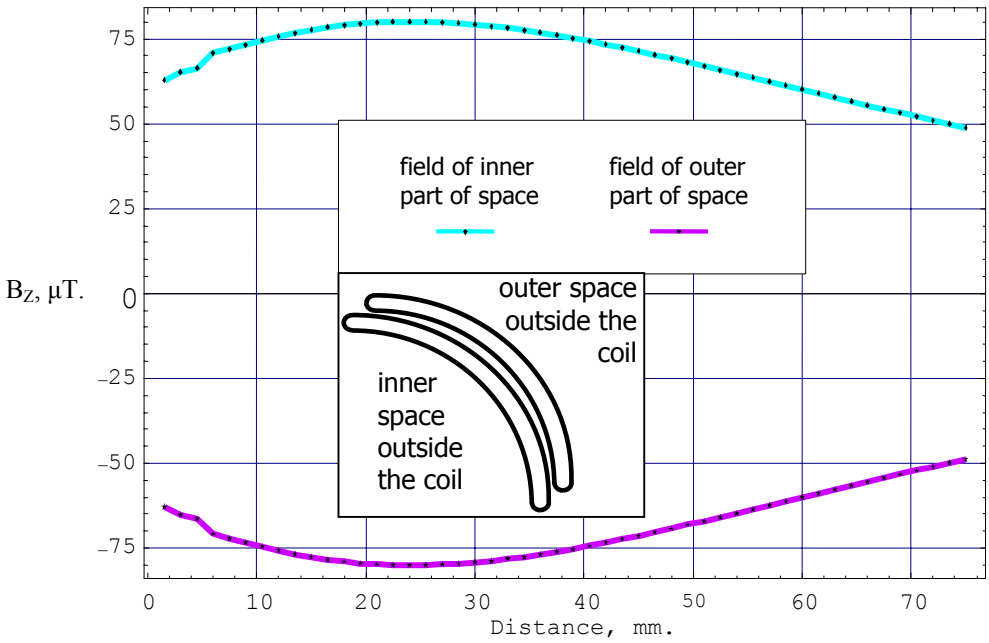

Figure 25: Field outside of bootstrap coil, in inner and outer parts of space. The distance means a distance in outside of the coil along the symmetry axis, zero of distance is the conducting layer of the coils.

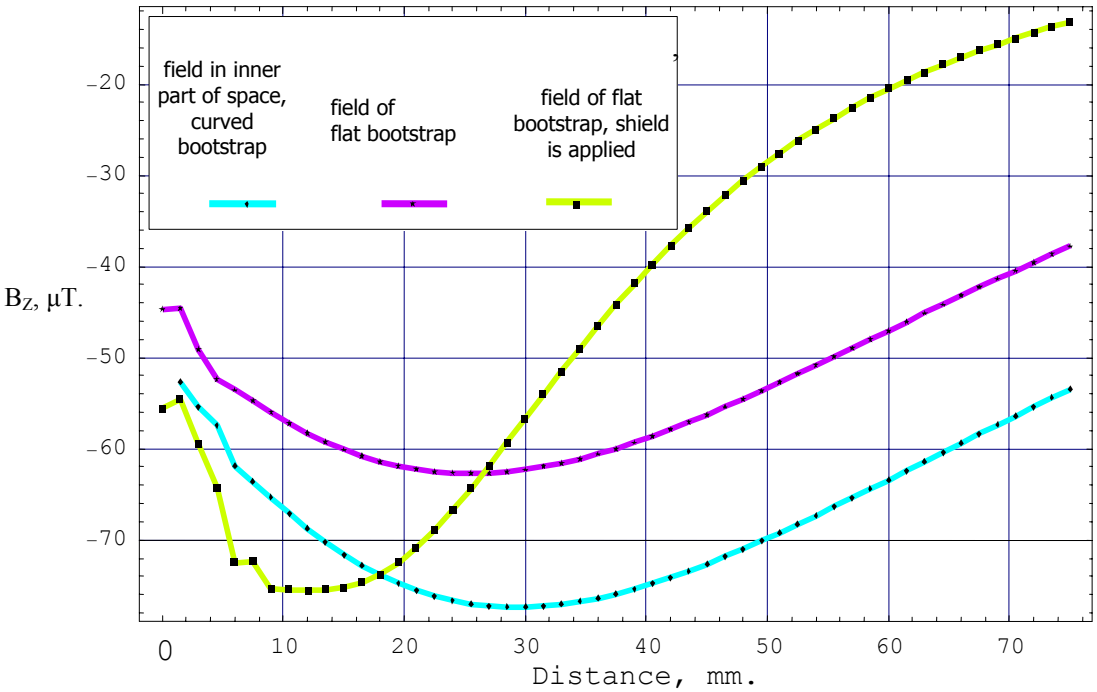

Figure 26: Field outside of bootstrap coil. Comparison between curved and flat bootstrap, and for the flat bootstrap coils shield applied. The distance is taken from the coil along the optical axis.

Reducing the gap between coils and flux-guiding mu-metal plate to 1 mm (what is allowed by manufacturing facilities), reduces the field outside by approximately a factor of 5. Even after reduction of the gap the field is still big enough to make some precession of the spin outside of the bootstrap. Spin turn in the outer space on the one side of bootstrap is approximately 20° in this case. But the spins stay in the plane of precession (horizontal plane) and the distortion of the polarization is negligible. Unfortunately, it is very hard to simulate the curved bootstrap with the mu-metal shield because of computer power and resources needed for it. But one can guess on the basis of the Figure 26, that application of the shield will reduce the path integral outside of the coil to a value small enough that it is negligible.

3.4 Radio frequency field coils for curved bootstrap.

The geometry of the multi angle spin echo spectrometer requires the radio frequency coil to be curved as well. A model of such a coil has been built within the "Radia" magnetostatic package [18]. The model was constructed as a superposition of "racetrack" elements (Figure 27). One "racetrack" is equivalent to one winding of the tape used for manufacturing the real coil. Since for each racetrack element the field is computed analytically, the field of the whole coil has being calculated analytically and the calculations are free from errors of iteration routines of numerical methods [19]. A three dimensional vector diagram of the field of the coil is shown in Figure 28.

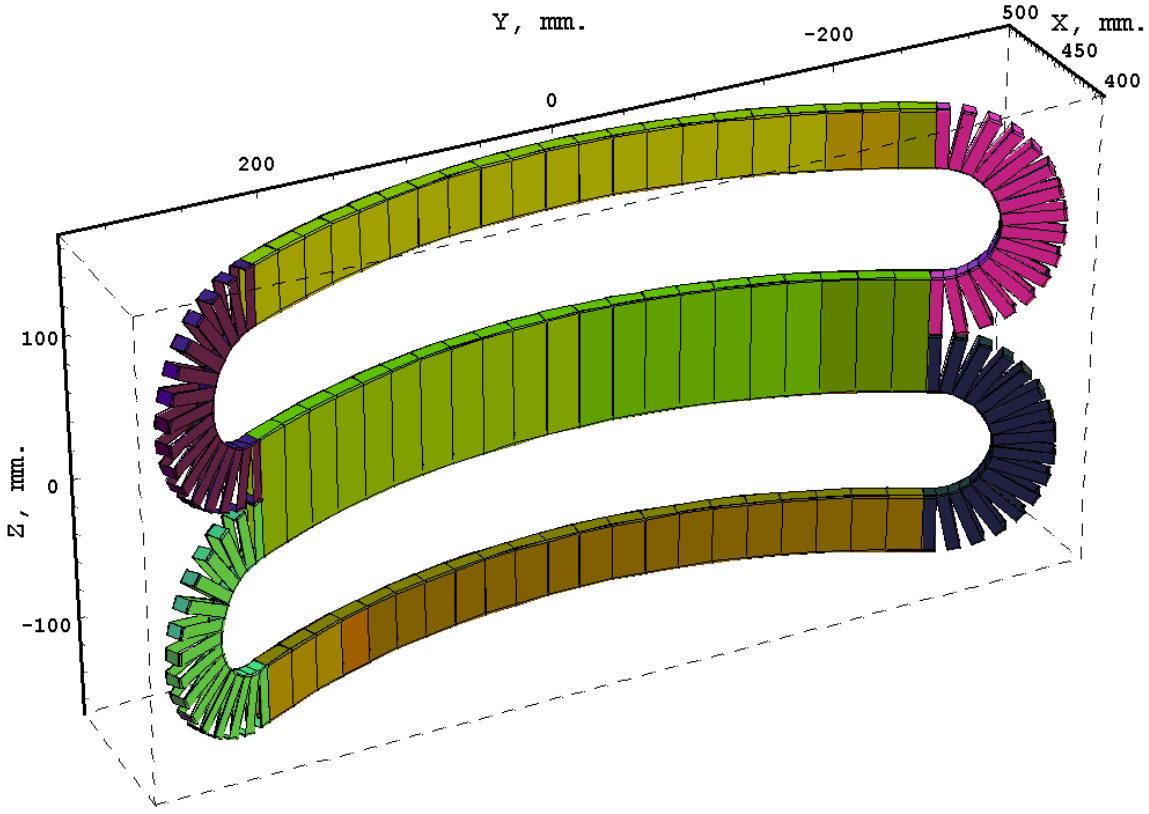

Figure 27: Radio frequency coil of curved bootstrap coil.

The parameters of the curved RF coil used in the simulation are the following. The radius of the coils is 0.5 m. The angular size of the main part covers an angle of 54° (50° working area, 2° on each side – overlapping). The coil width is 10mm. The height of the main part of the coil is 80 mm. The height of upper and lower flux guiding part is 40 mm (the guiding coils together have the same flux as the main coil). The thickness of elements used in computation is 0.5 mm (the real value for hardware manufacturing may

be ~1 mm, but a value of 0.5 mm was chosen to avoid wire shape effects in this particular consideration. The action of the wire shape on beam polarization was considered in paragraph 2.1 in this thesis). The value of the current applied to the single "racetrack" element is 1, what actually does not correspond to a real value of the current to be applied to the coil, but since the field of the coil depends on the current linearly, any value of the current can be used here, while the result of computation must be considered relative to the maximum field value, as it is done in this work.

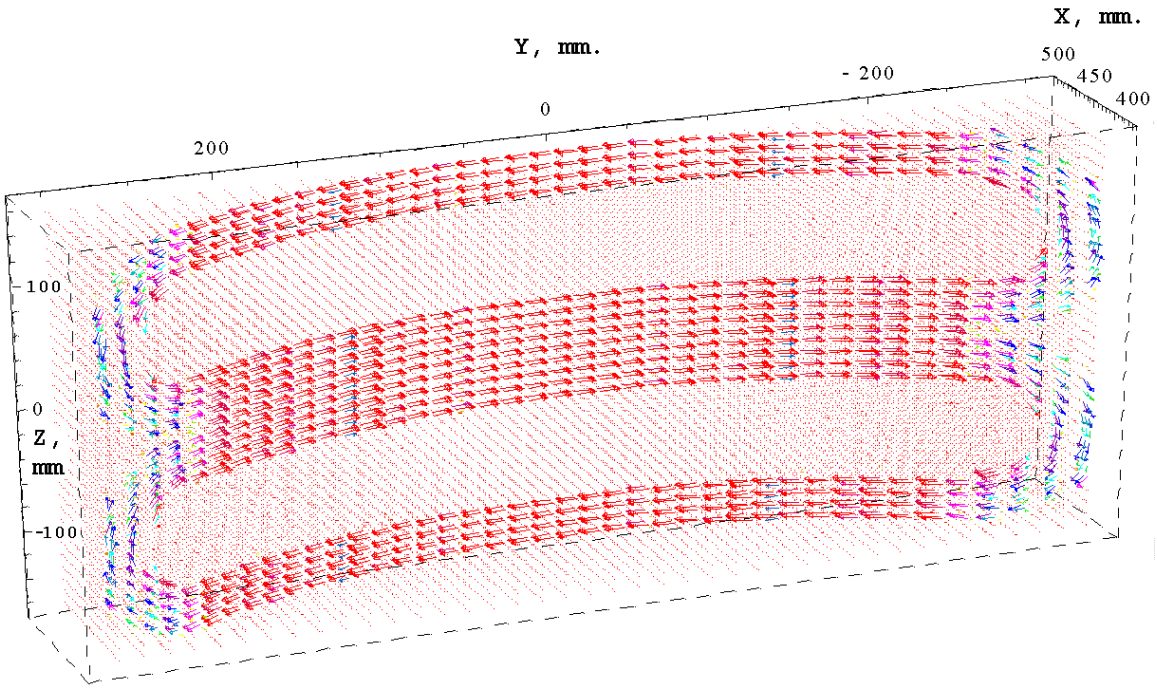

Figure 28: 3D-field diagram of the curved RF coil. Lengths of arrows are proportional to the magnitude of the field.

Drawbacks of coil performance may originate from 3 sources:

1) A general reduction of field to the ends, caused by final angular size of the coil, leads to differences in flipping angle with respect to the necessary flip of π. The plot of the actual (angular) field fn the coil is shown in Figure 29.
2) The local angular field variation caused by the winding structure. The element width is a constant along the radius from the center of coil curvature, "straight" coils (main and flux back guiding) will have some slits on the outer (along the radius) side of the coil). The plot of the field in the neighborhood of the outer side of the main coil is shown in Figure 30. Figure 31 illustrates the same situation using a surface plot.

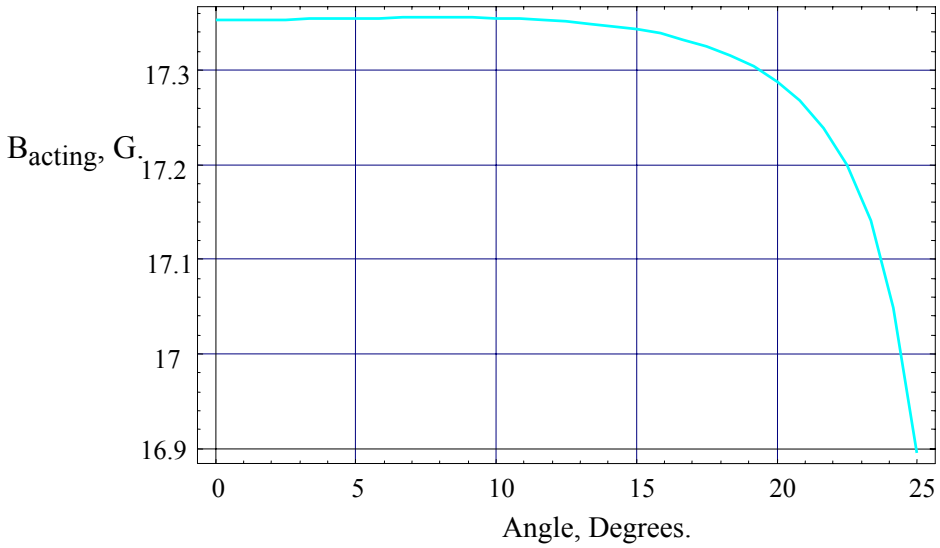

Figure 29: Reduction of the acting field from the center to side of the coil (the field magnitude corresponds here to the maximum value of the time-varying RF field).

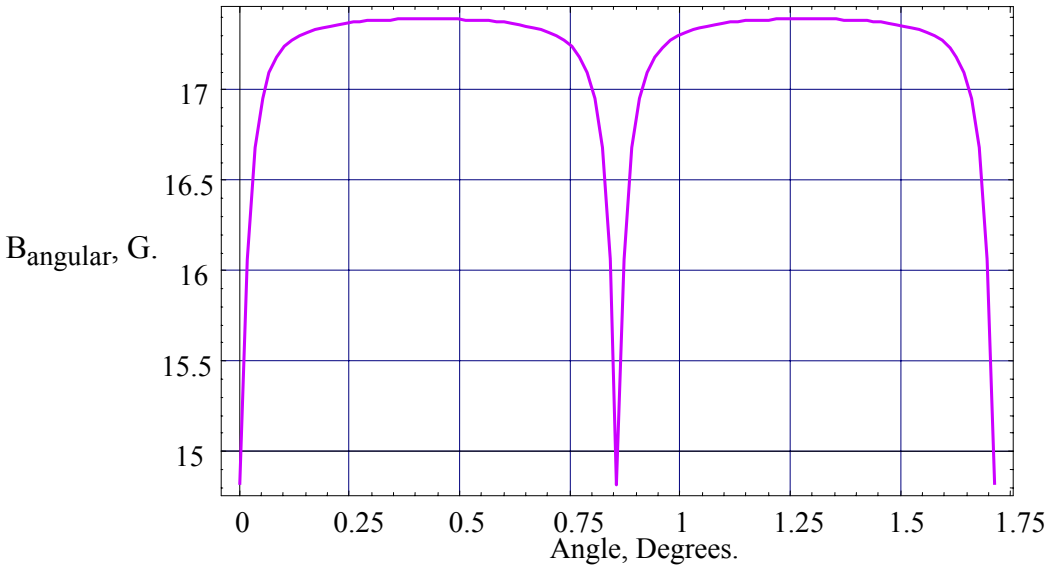

Figure 30: Variation of the field as a function of the angle close to outer side of the coil. The plotted angular region is equivalent to two windings of coil structure.

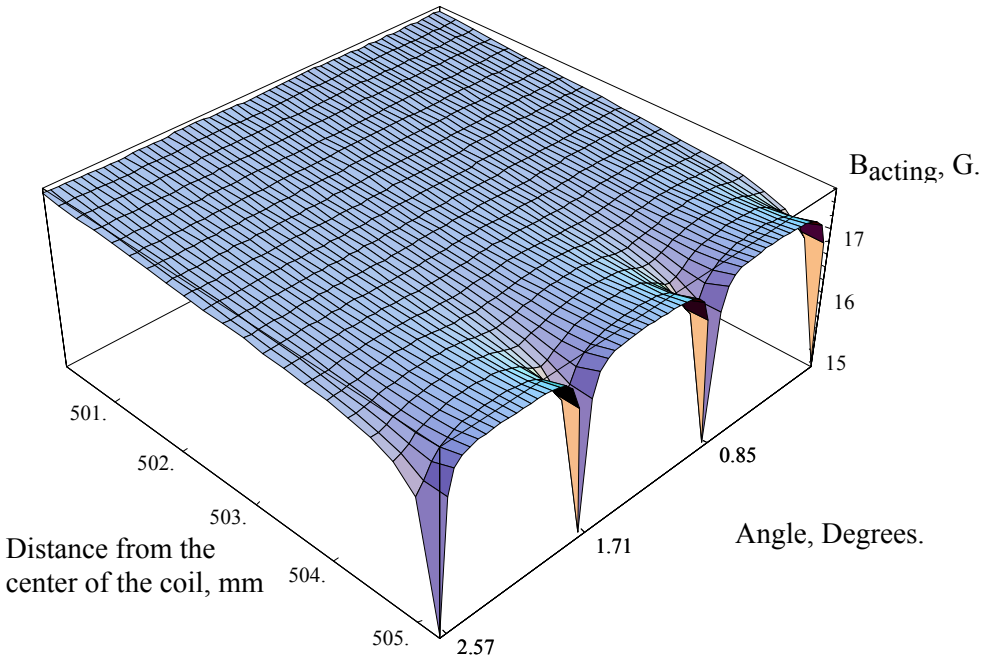

Figure 31: The variation of the field along the angle close to the outer side of the coil. Plotted angular region is equivalent to three windings of coil structure. The radial size of the coil is 10 mm.

3) Homogeneity of the field along the radius inside of the coil. Non-homogeneities cause a variation of the angular velocity of the spin flip and an additional RF current has to be applied to get a flip of exactly π. This situation is illustrated in Figure 32.
4) Field leaking out of the coil (caused by various factors), what could lead to depolarization of the neutron beam after passing the coil. Here the real value of the applied field is important. The maximum (as soon as field varies with time) field value, which can be used is ~17.2 G.

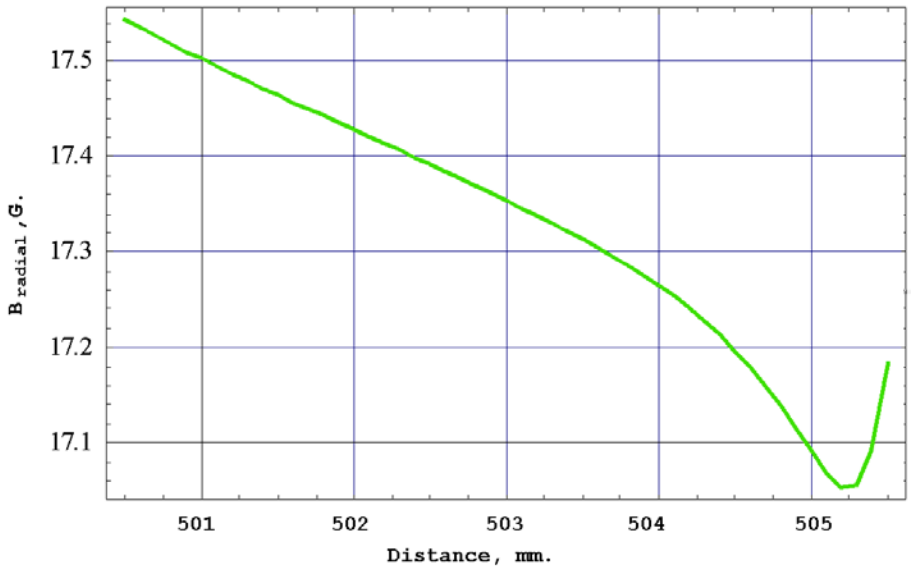

Figure 32: Field dependence along the radius passing the center of a turn.

The field magnitude corresponds here to the maximum value of the time-varying RF field.

First we consider factors 1 and 2. If the width of the tape is about 4 mm, the whole field reduction toward the side of the coil amounts to about~2.5% of the average field value. Local field differences were estimated in terms of path integrals (with path length 10 mm – to have the path inside of the coil). These differences consisted of ~4% from the maximal value of the path integral. Increasing the angular size of the coil makes the error of a factor 2 (see above) smaller, but it does not disappear at all as it is local. It was obtained, that the drawbacks described in items 1 and 2 (see the beginning of this paragraph) get smaller as the width of the coil racetrack element (one wind) becomes smaller. If the width of the tape is about 1 mm, the situation is as follows: the reduction of the field to the sides consists of 0.05% of the mean field value, the local field (path integral) non-homogeneity is 0.16% from the average path integral value, and these values are the same for every neutron trajectory in the beam window. The number of elements used for flux guidance do not affect these two factors significantly, the used number of "racetracks" is 60 (width of element~3mm). The obtained values demonstrate that for small enough element width the deviation of actual spin flips from π will be ~1%, what is good enough. As for factor 3 – non-homogeneity of field along the radius – it is 2%, what is good enough as well.

The field outside of the coil was considered in comparison with the normal, flat RF coil used for normal NRSE [20] Figure 33.

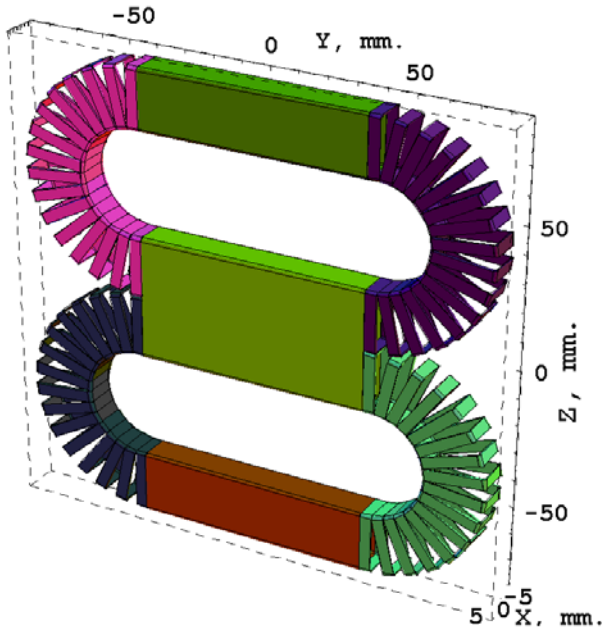

Figure 33: flat RF coil used for normal NRSE.

For the curved RF coil such a field is one order of magnitude smaller then for the flat coil, nevertheless it is of significant value – Figure 34.

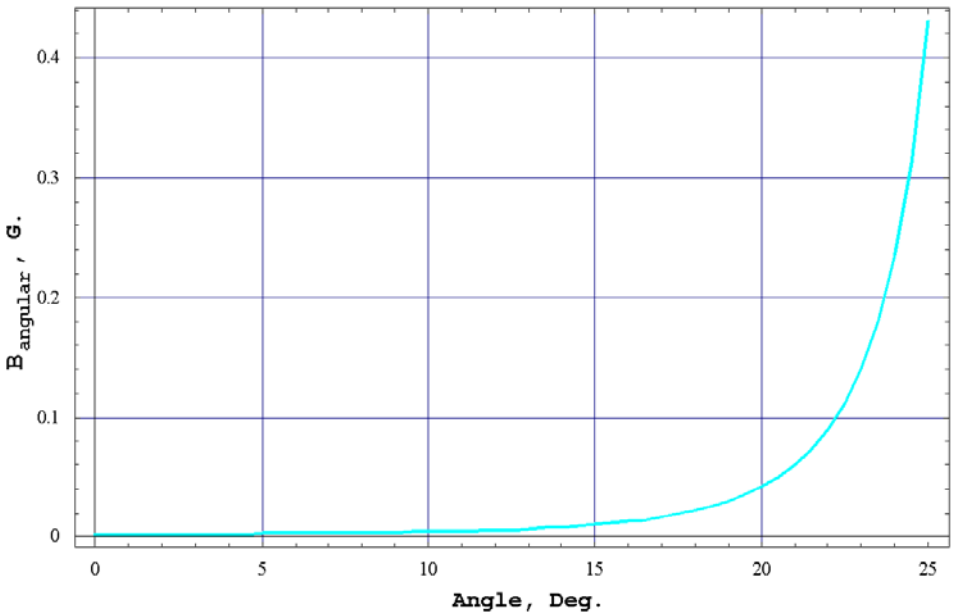

Figure 34: Field magnitude outside of the curved RF coil, along the outer side of coil (constant R = 507 mm).

But as soon as this field is order of magnitude smaller then the corresponding field of the flat coil, coil the reduction in performance caused but this field should be negligible.

The second question here is how big will be the field nearby mu-metal plates, covering the coil of the static field of the curved bootstrap coil (paragraph 3.2 in this thesis). Simulations show that this field will be as small as ~10^{-5} G and we do not have to worry about it. The field inside of the coil will be homogeneous enough to give acceptable performance if we use wire (band) of 1 mm width. In this case all described drawbacks will be small.

Chapter 4. Measurements of phonon linewidths in germanium.

4.1 Survey of theoretical and experimental results obtained for phonon lifetimes.

The obviously first experiment on measurements of phonon lifetimes by means of neutron scattering has been done by Furrer [21] in Pb in 1970. The first measurement of anharmonic effects in Germaium has been done by Nelin and Nilsson [22] in 1974. They got phonon linewidth 537±41 μeV for L_3 at 300K, 422±40 μeV for L_3 at 700K and 537±41 μeV for X_3 at 700k. No extraction of the lifetimes from these experimental data was presented. Very good results on self-energy measurements in silicon are presented in [23] and [24].

In the last ten years strong interest to a profound knowledge of phonons arose again, namely to phonon lifetimes and to spectral shifts in isotopically modified semiconductors. Publications [25], [26], [27], [28] review aspects such as the influence of the isotopic composition on the lattice constant of germanium [29], [30], [31] and of compound semiconductors [32]. The thermal conductivity is strongly affected by isotope disorder, e.g., it is increased by a factor of ten in isotopically pure germanium with respect to that of natural germanium crystals [33], [34]. In certain cases, isotope substitution can be used either to discern the effects of isotope-disorder-induced phonon scattering from those stemming from the anharmonic decay of phonons, [35], [36], [37] or to tune the effect of anharmonic decay channels [38]. Isotopic mass fluctuations in elementary semiconductors represent a particularly simple form of disorder that involves only mass fluctuations but no significant structural or force constant disorder. Phonons are thus well suited for the theoretical and experimental study of isotope disorder effects. Disorder-induced effects on the energies and life-times of phonons appear as an ideal testing ground for theories used for disordered systems like, e.g., the coherent potential approximation. germanium is especially well suited for such a study for several reasons: the range of masses covered by its stable isotopes is rather large, from 70 to 76 atom mass units, it can be grown as single crystals with a high degree of perfection, and anharmonic effects are relatively small, leading to long lifetimes in the absence of isotope disorder.

Significant progress is achieved in measurements of optical phonons near the center of the Brillouin zone by Raman scattering. Plenty of very comprehensive and detailed works were published on this topic [39], [40], [41], [42]. Remarkable results were achieved in [43] for damping of the acoustic phonons, studied by X-ray diffraction.

Recently three significant papers were published about lifetime changes in germanium because of modification of isotopic composition [44], [45] and [46]. The work [45] is probably the most thoughtful and comprehensive and can be considered as a starting point for further investigations of the linewidth in germanium by means of neutron scattering by standard triple-axis technique. Mostly optic phonons were studied therein. As for acoustic phonons, problems with the experimental resolution did not allow the authors to get reasonable results. For comparison of the obtained experimental data the authors in [45] used two theoretical models: Self-consistent Born Approximation (SCBA), Coherent Potential Approximation (CPA) and Super Cell (SC) calculations, which have more numerical character.

Let us consider now these theoretical approaches in some detail. The SCBA is based on second order self-consistent perturbation theory [47], where the complex self-energy Σ(ω) for the particular phonon of energy ω is given by:

$$\Sigma(\omega) = \frac{\omega^2 g}{N} \int_0^{\Omega_{MAX}} \frac{2\Omega\rho(\omega)d\Omega}{\left[\Omega^2 - \omega^2 - 2\omega\Sigma(\omega)\right]} \qquad (4.1),$$

$$\text{where } g = \sum_i x_i \left[1 - \frac{m_i}{\bar{m}}\right]^2 \qquad (4.2)$$

$\bar{m}$ is the average isotope mass of the crystal, m_i is the mass of the i-th isotope, x_i is the concentration of the i-th isotope. $\rho(\omega)$ is the one-phonon density of states. For the particular self-energy the line width and anharmonic shift of the phonon frequency are given by:

$$\Delta_{CPA}(\omega) = \frac{1}{2}\omega\,\mathrm{Re}[\Sigma(\omega^2)] \qquad (4.3)$$

$$\Gamma_{CPA}(\omega) = -\frac{1}{2}\omega\,\mathrm{Im}[\Sigma(\omega^2)] \qquad (4.4)$$

Equation (4.1) should be solved numerically by iterations. The necessary phonon density of states can be taken from experimental data [48] (which are very accurate), or calculated by some ab-initio code (which will be discussed in this paragraph in details).

Implementation of the Bond-Charge Model for DOS calculations does not seem reasonable here, because available codes for that like [49], do not give satisfactory results for the phonon dispersion in Ge. Probably better results for the DOS can be obtained with the help of the dynamical matrix taken from [50]. Despite of the fact that six coordination spheres are used there to construct dynamical matrix, the result for the phonon dispersion in Ge can not be called perfect.

A more deep description for the change of linewidth and anharmonic line shifts can be obtained by the Coherent Potential Approximation (CPA). The self-energy $\tilde{\varepsilon}(\omega^2)$ in CPA for the particular phonon of frequency ω is given by the following equation:

$$\tilde{\varepsilon}(\omega^2) = \sum_i \frac{x_i r_i}{1 + \left[\tilde{\varepsilon}(\omega^2) - r_i\right] \bar{m}\omega^2 G_0 \left\{\omega^2 [1 - \tilde{\varepsilon}(\omega^2)]\right\}} \tag{4.5}$$

where the Green's function G_0 and the dimensionless mass deviations r_i are defined as:

$$G_0(\omega^2) = \frac{1}{\bar{m}} \int \frac{\rho(\omega')}{\omega^2 - \omega'^2} d\omega' \tag{4.6}$$

$$r_i = \frac{\bar{m} - m_i}{\bar{m}} \tag{4.7}$$

where $\bar{m}$ is the average isotope mass of the crystal, m_i is the mass of the i-th isotope, $\rho(\omega)$ is the one-phonon density of states. The change of phonon frequency (line shift) and the change of the linewidth in CPA are calculated from $\tilde{\varepsilon}(\omega^2)$ (respectively):

$$\Delta_{CPA}(\omega) = \frac{1}{2} \omega \, \mathrm{Re}[\tilde{\varepsilon}(\omega^2)] \tag{4.8}$$

$$\Gamma_{CPA}(\omega) = -\frac{1}{2} \omega \, \mathrm{Im}[\tilde{\varepsilon}(\omega^2)] \tag{4.9}$$

CPA gives also the modification of expression for the phonon DOS, where the effect of the isotopic disorder is included:

$$\rho_{eff}(\omega) = \frac{2}{\pi\omega} \mathrm{Im}\left[\int \frac{\rho(\omega')\omega'^2}{\omega^2 [1 - \tilde{\varepsilon}(\omega^2)] - \omega'^2} d\omega'\right] \tag{4.10}$$

Both approaches described above give a good representation of the experimental data. Nevertheless they do not include the dependence of the self-energy on the phonon wave vector $\boldsymbol{q}$ and this fact can be taken into account in further improvements of this theoretical approach.

Another approach to calculate the phonon lineshifts and lifetimes is the Super Cell approximation. This method is based on the following idea: just a large cell (diamond

structure) with a big number of atoms is taken (consisting of hundreds of atoms), and for such a cluster atom dynamics is considered on the base of the harmonic approximation (force constant model, thoroughly described in [51] and [52], or Bond-Charge Model), but the mass, corresponding to the particular isotope, is ascribed to each atom of the supercell randomly. The dynamical matrix of such a cluster is calculated and serves as a base for calculating the anharmonic effects.

In reference [45] results of CPA and SC are compared between each other and with experimental data (for optic phonons). From the results of [45] one can conclude that CPA and SC represent the effects of isotope disorder on the lattice dynamics of germanium in very good agreement with experiment.

Anther way to calculate anharmonic properties of the crystal and their change with isotopic modification of the crystal consist in using ab-initio computing codes. The term "ab-initio" means that for these codes no other input information except the chemical composition of the compound is needed (actually parameters like the density of the k-grid in the Brillouin zone or energy cutoff also have to be supplied as input). Such ab-initio codes usually join pure analytical calculations and some pure numerical routines like iterative solving of equations or algorithms of fast Fourier transform.

The best proven ab-initio packages available now are the following: V.A.S.P (Vien Ab-initio Simulation Package) [53], AB-INIT [54], and PWscf package [55]. All these packages are developed for Linux. We discuss facilities given by these packages.

V.A.S.P.

V.A.S.P. is not free of charge, the price of it per single machine for academic use is 3.000 Euro. This package gives the most wide range of possibilities for calculations for condensed matter among other ab-initio packages. But it can not be directly used for lattice dynamics computations; the special program "Phonon"[56] has to be used for that. The demo-version of this program was not very convincing.

VASP is a complex package for performing ab-initio quantum-mechanical molecular dynamics (MD) simulations using pseudopotentials or the projector-augmented wave method and a plane wave basis set. The approach implemented in VASP is based on the (finite-temperature) local-density approximation with the free energy as variational quantity and an exact evaluation of the instantaneous electronic ground state at each MD time step. Forces and the full stress tensor can be calculated with VASP and used to relax atoms into their instantaneous ground-state.

AB-INIT

The AB-INIT package is distributed under the GNU General Public License, the main features of the code are fully described in [57]. This program is based on the density functional theory (DFT) [58], [59]. The main program in ABINIT, as well as some utilities, are written in FORTRAN90. The package also includes documentation files, scripts for automatic testing, pseudopotential files. The main capabilities of the program are the following: electronic ground-state calculations [60], structure-related calculation (structure optimization and molecular dynamics) [61], [62], [63], [64], [65], and response-function capabilities [66]. One can use also the state-of art capabilities of AB-INIT to do the calculations on spin –orbit (SO) interaction [67], [68] and the fluctuation dissipation theorem [69], [70], [71].

AB-INIT is a huge program and the syntax of the input file (which defines the structure of material, what kind of calculations are to be done, the parameters controlling the calculation) is rather complicated and actually demands a deeper studying even if one needs to do only simple calculations.

PWscf

The PWscf program is distributed under the GNU General Public License. This program in our case was chosen for lattice dynamics in germanium. This code is written in FORTRAN90, and it needs external Blas/Lapack [72] libraries and a Fast Fourier Transform (fftw) library [73]. The main capabilities of this code are the following:

ground-state energy and one-electron (Kohn-Sham) orbitals,
atomic forces, stresses, and structural optimization,
molecular dynamics on the ground-state Born-Oppenheimer surface,
variable-cell molecular dynamics,
phonon frequencies and eigenvectors at a generic wave vector,
effective charges and dielectric tensors,
electron-phonon interaction coefficients for metals,
interatomic force constants in real space,
third-order anharmonic coefficients.

PWscf is based on density-functional perturbation theory (DFPT) [74]. The deep exploration of the theory implemented in the PWscf code can be found in [75] together with some results achieved by this code in the description of lattice dynamics. The PWscf package represents a very good example of really professional programming and software

engineering, what is not always so with free of charge scientific software. Also the input files syntax (which defines the structure of the material, what kind of calculations are to be done, the parameters controlling the calculation) is simple and examples of input files, supplied with the package itself, give a very comprehensive guide to start own coding. One should definitely remark the support which is supplied to beginners (and to advanced users in case of complicated calculations) via internet e-mail forum. The help given to the author of this manuscript from PWscf forum is above any critics and without it this part of the thesis hardly could have been completed. Probably the main disadvantage of the PWscf is a complicated procedure of compilation of the source code to get the executables.

In working with the PWscf code for germanium lattice dynamics calculation we used the pseuopotential file from [76]. The plane wave energy cutoff was chosen to be 18.0 Ry.

In recent time some works have been published, where DFPT was used for the description of anharmonicity in one-component semiconductors (Silicon and germanium). In spite of the fact that DFPT can calculate only the third derivatives of total energy of the crystal, it gives rather good results. In [77] the change of Raman frequencies due to the isotopic modification of the crystal is calculated, and good agreement with experiment was found. In [78] the frequency shift due to the anharmonic effects and linewidth are calculated for high symmetry directions in silicon and germanium. Unfortunately no reliable experimental results are available for the comparison now. But this work can be used as a perfect starting point for the calculation of phonon lifetimes in germanium for pure crystal and for the isotopically modified sample.

4.2 Triple-axis spectrometer technique.

One of the important objects for investigation in neutron scattering is a measurement the microscopic dynamics of condensed matter. Neutrons of thermal energy give a unique opportunity for exploration of crystal lattice dynamics, because the wavelength of thermal neutrons is comparable to atomic distances and their energies are comparable to energies of crystal dynamics. Actually this matching is not accidental – thermal neutrons are in equilibrium with the vibrations of H_2O or D_2O in the moderator of the neutron source. The method for measurement of crystal oscillations (phonons) was established in the fiftieths of the last century by the group of B.N. Brockhouse [79]. Now this method is well-known as triple axis technique. The lay-out of a triple-axis spectrometer is given in the Figure 35.

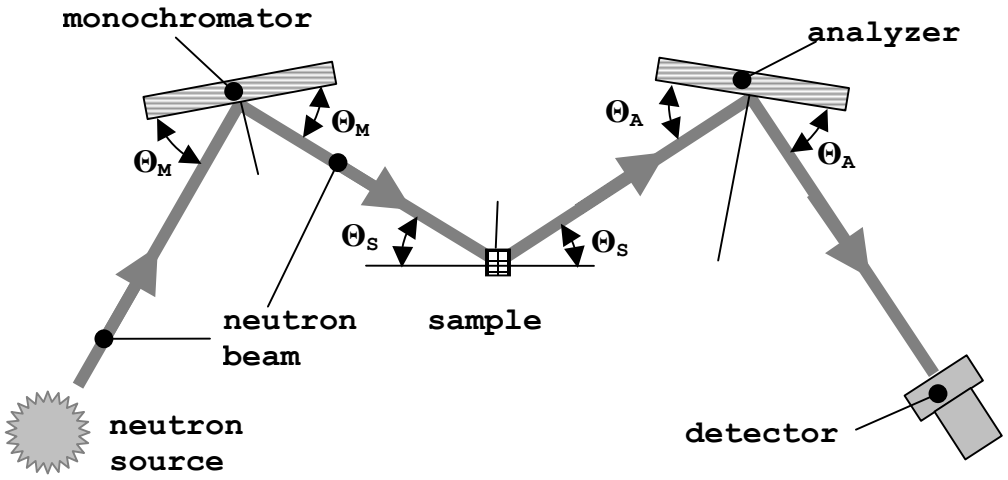

Figure 35: The lay-out of a triple-axis spectrometer. Angles Θ_M, Θ_S, Θ_A are Bragg angles of the monochromator, sample and analyzer, respectively.

On traversing of the setup shown in Figure 35, neutrons, initially having a Maxwell velocity distribution, suffer Bragg scattering [80] from a single crystal monochromator. Due to Bragg scattering on the monochromator neutrons of a narrow wave vector distribution [81] around the first order of Bragg reflection are transmitted further. To suppress higher orders of Bragg reflections, filters are commonly applied. The neutrons of the selected wave vector are scattered from the sample in different direction with

different energies. An analyzer is applied downstream from the sample to select the neutrons of a particular wave vector. To reduce the divergence of the neutron beam at different stages of this setup, the collimators may be applied.

This technique allows to determine the energy transfer between the neutrons and the sample as a function of the scattering angle $2\Theta_S$, which defines the momentum transfer. Generally, the scattering of a neutron by a phonon (what triple axis technique actually measures) obeys momentum and energy conservation laws:

$$\boldsymbol{k}_i - \boldsymbol{k}_k = \boldsymbol{Q} \tag{4.11}$$

$$\frac{\hbar^2 k_i^2}{2m} - \frac{\hbar^2 k_k^2}{2m} = \hbar\omega \tag{4.12}$$

$\boldsymbol{k_i}, \boldsymbol{k_k}$ are the wave vectors of the incoming and scattered beams, $\boldsymbol{Q}$ is the momentum transfer and $\hbar\omega$ is the energy transfer. The momentum transfer consists of a reciprocal translation lattice vector $\boldsymbol{\tau}$ and a phonon wave vector $\boldsymbol{q}$. The relation between them is shown in Figure 36.

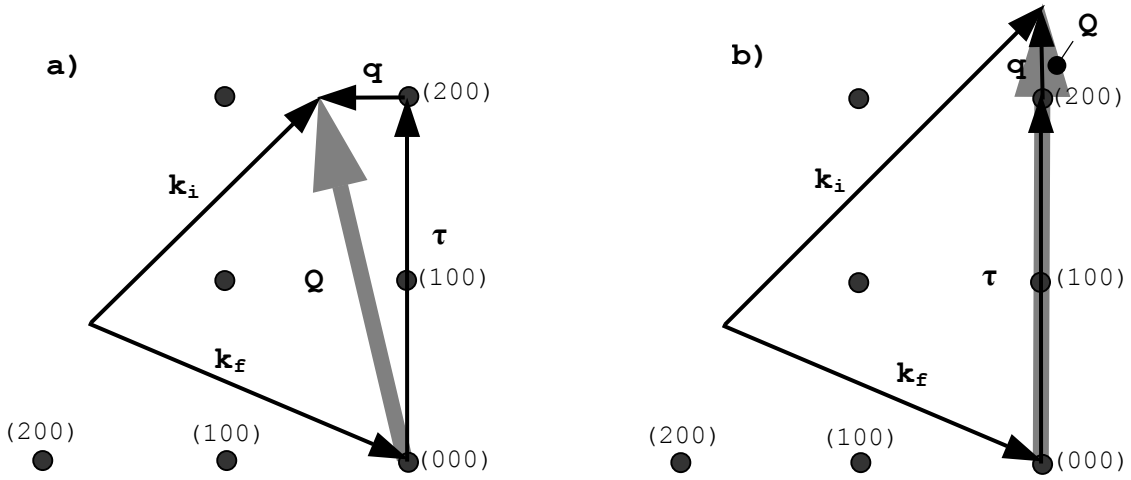

Figure 36: The relation between the momentum transfer $\boldsymbol{Q}$, the reciprocal lattice vector $\boldsymbol{\tau}$, and a phonon wave vector $\boldsymbol{q}$ in reciprocal space of the crystal. a) illustrates the scattering by a transverse phonon, b) illustrates the scattering by a longitudinal phonon.

The main application of triple axis technique consists in measuring the phonon dispersion relation – the dependence of the energy of the phonon from its wave vector.

The usual way consists in scanning with constant momentum transfer at different energy transfers (constant q scan), which is illustrated in Figure 37.

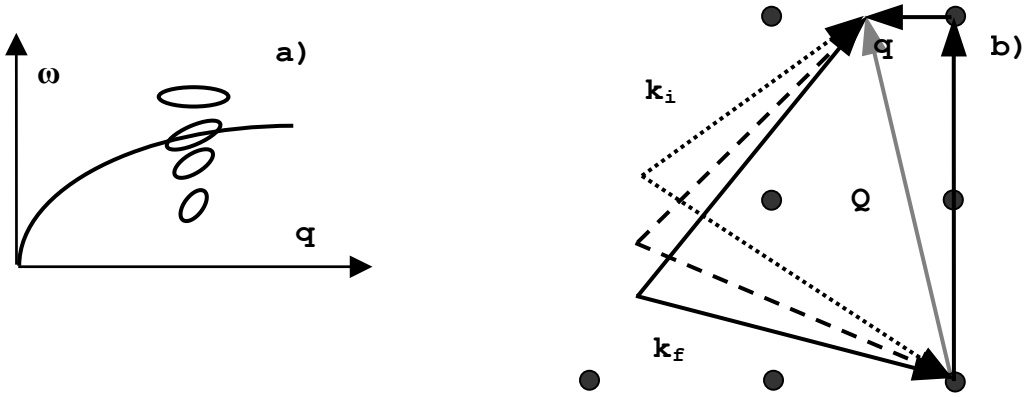

Figure 37: Measurement of the phonon dispersion relation at constant momentum transfer $\boldsymbol{Q}$. a) shows how a constant $\boldsymbol{Q}$ scan relates to the dispersion curve, b) shows how a constant $\boldsymbol{Q}$ scan looks like in reciprocal space.

In Figure 37 a) the experimental points of the constant $\boldsymbol{Q}$ scan are shown by ellipses for the following reasons: neither monochromator nor analyzer give perfect δ function for $\boldsymbol{k_i}$ and $\boldsymbol{k_f}$, but due to the final resolution they give some distribution around $\boldsymbol{k_i}$ and $\boldsymbol{k_f}$. The resolution of a triple-axis spectrometer may be described in a good approximation by multiplication of Gaussian profiles for energy ω and each component of $\boldsymbol{k}$ [81]. The finite size of the resolution volume in (ω, $\boldsymbol{Q}$) space is usually represented by a resolution ellipsoid – a four dimensional surface, with a size depending on the spectrometer configuration. In the example shown in Figure 38 a) the resolution ellipsoid intersects with a bigger length of the dispersion curve than in the case shown in Figure 38 b), what leads to a bigger scattering intensity. Proper orientation of the resolution ellipsoid with respect to the dispersion curve is an important point in triple-axis experiments. Different orientations of the resolution ellipsoid can be achieved by different configurations of monochromator, sample and analyzer with respect to each other[82].

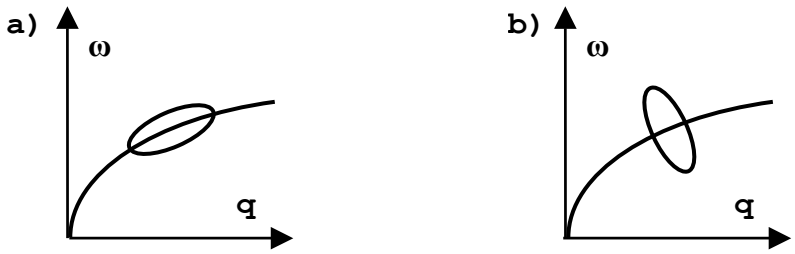

Figure 48: Different orientations of the resolution ellipsoid with respect to the dispersion curve. a) case of "phonon focusing", b) case of "phonon defocusing".

4.3 Uniting of triple-axis and spin-echo techniques.

Another application of the triple-axis technique consists in measuring of the anharmonical broadening of phonons. Linewidth measurements can be done by the constant momentum transfer method of by the constant energy transfer method.

Uniting the triple axis method with the spin-echo technique (namely NRSE) opens a new way for phonon linewidth measurements. It consists in selecting of a particular phonon by means of the triple axis technique and by investigating its anharmonical broadening by means of spin-echo technique. The method of tilted field boundaries (paragraph 1.2) has to be used in this case. Tilting of field boundaries means an inclination of the lines (generally speaking planes) of the constant τ_{NSE} to be parallel to the slope of the dispersion curve in the point of measurement [83]. This situation is illustrated in Figure 39. The distance between the lines of constant τ_{NSE} represents the limit of the spin-echo energy resolution. The closer the spin-echo lines, the higher the energy resolution. The intersection of the lines of constant τ_{NSE} with the dispersion curve (surface) leads to a depolarization of the neutron beam [84]. From that a phenomenological conclusion can be derived: spin-echo energy resolution for the case of phonon line width measurements is limited by the curvature of the dispersion surface.

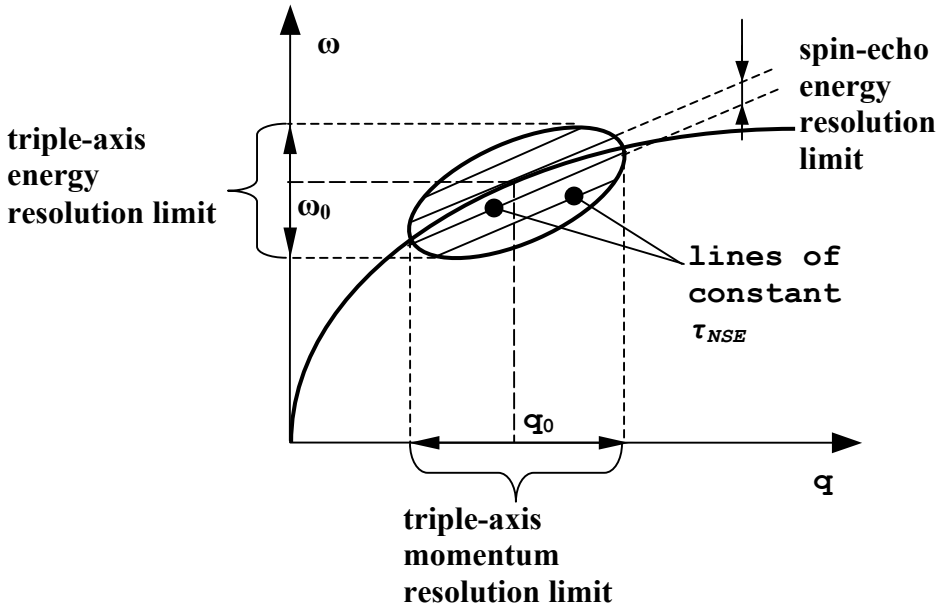

Figure 39: Improvement of triple-axis energy resolution by spin-echo. The background triple-axis resolution ellipsoid is shown with lines of constant τ_{NSE}.

In case of triple-axis measurements one has to deal with a dispersion surface as function of q_x and q_y, as it is shown in Figure 40. The energy resolution of spin-echo measurements is limited by curvature of the dispersion surface within the resolution ellipsoid. Therefore, only the most flat parts of the dispersion surface are suitable for linewidth measurement by means of spin echo.

For line width measurements one has to look for places of sufficiently low curvature of the dispersion surface. Such a proposal for the study of germanium linewidths is an object of this thesis work and will be described further in this manuscript. Besides curvature of the dispersion surface one has to take into account the scattering rate from the particular phonon, which should be reasonable (the curvature can be rather small but scattering from the chosen phonon can be too small to do an experiment). Also one has to remember about triple-axis phonon focusing, i.e. choosing a proper orientation of the resolution ellipsoid (see Figure 40). As the angle of turning of the bootstrap coils is usually limited to ± 50° [85], not all configurations can be met for the phonon line width measurements, and this the main technical limitation for measurements of phonon linewidth by united tripe-axis and NRSE techniques.

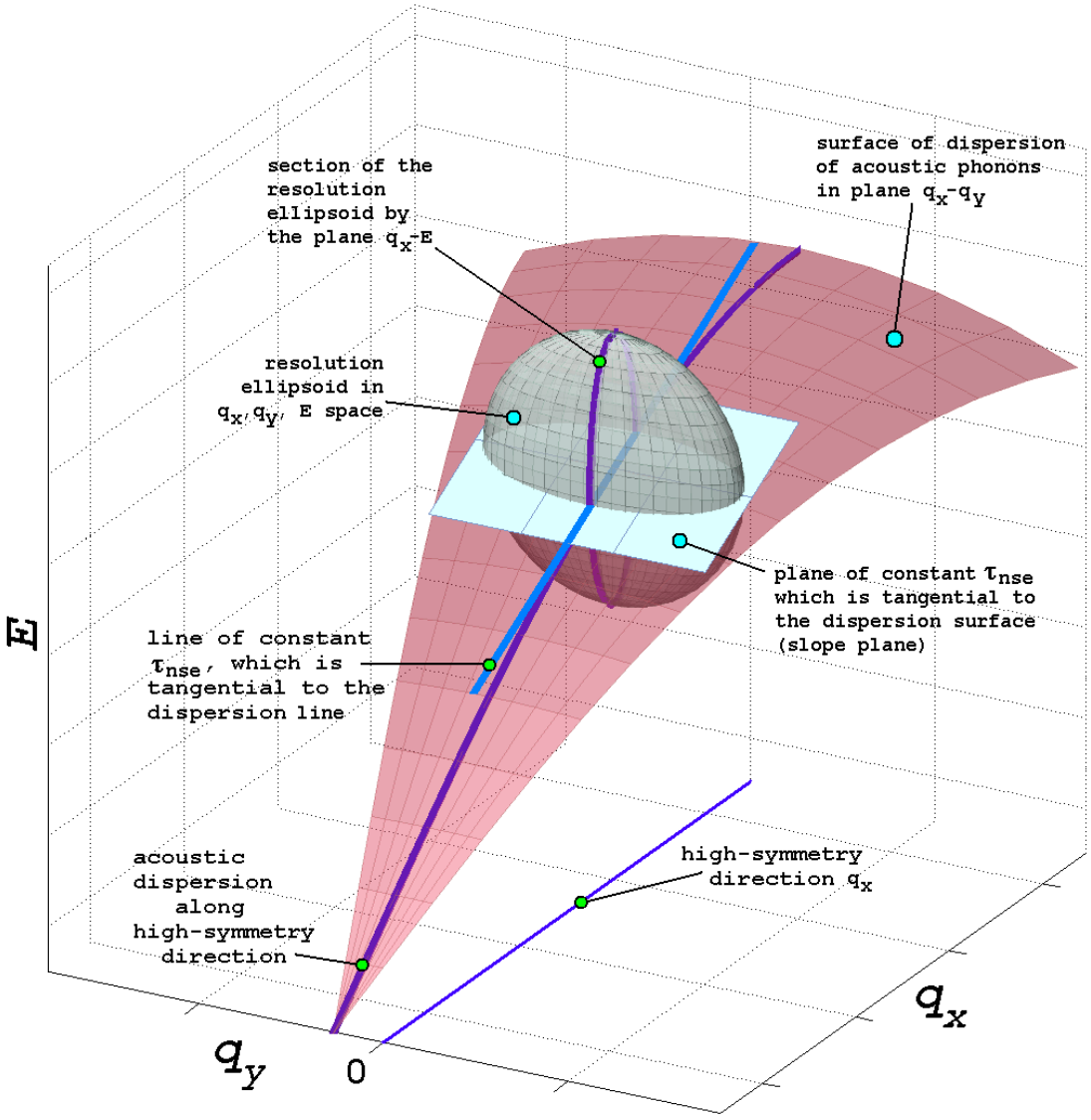

Figure 40: The generalization of Figure 39 - intersection of the dispersion surface with the resolution ellipsoid.

4.4 Basic data about germanium.

Germanium is the 32nd element of the Mendeleev table. Stable isotopes of it are 70, 72, 73, 74, 76. It has the crystal structure of diamond with lattice constant 5.658 Å at 300K (space group $Fdm(O^7_h)$), with two atoms in a unit cell at positions (000) and (1/4,1/4,1/4). The model of a germanium crystal structure and the shape of its Brillouin zone is shown in Figure 41.

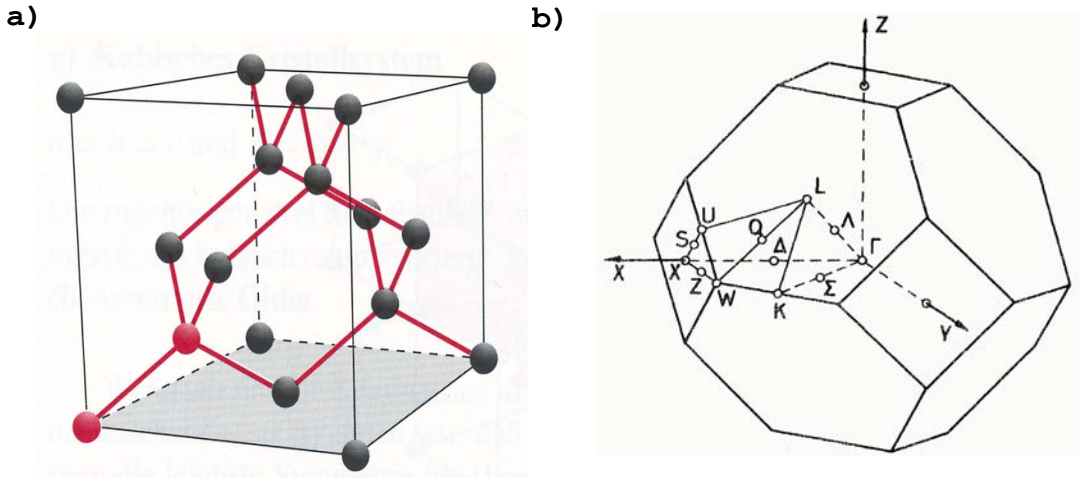

Figure 41: Crystal structure of diamond-type lattice a) and its first Brillouin zone with conventional notation of points and directions in reciprocal space.

As there are two atoms in the unit cell of germanium, crystal oscillations consist of three acoustic and three optic branches. They are shown in Figure 42. Because of the symmetry of the germanium crystal structure, along some directions transverse oscillations are degenerate. The phonon density of states for germanium is given in Figure 43.

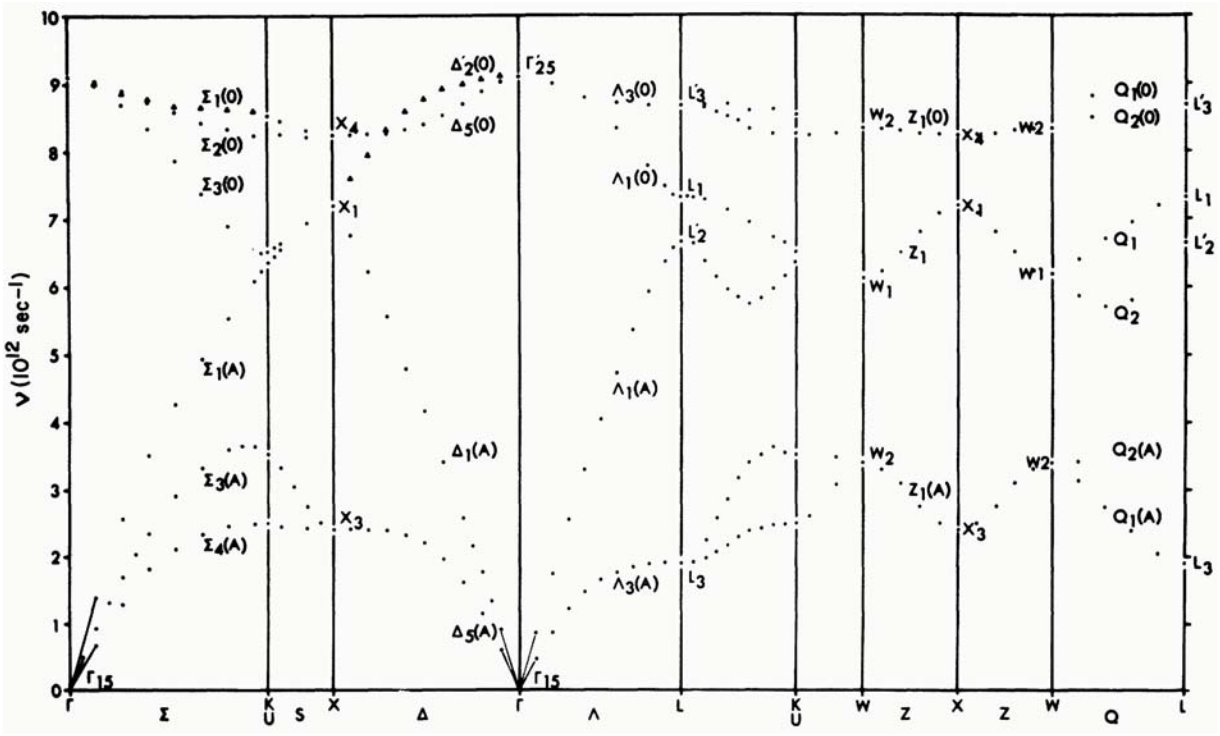

Figure 42: Phonon dispersion in germanium (at 80k). From [86].

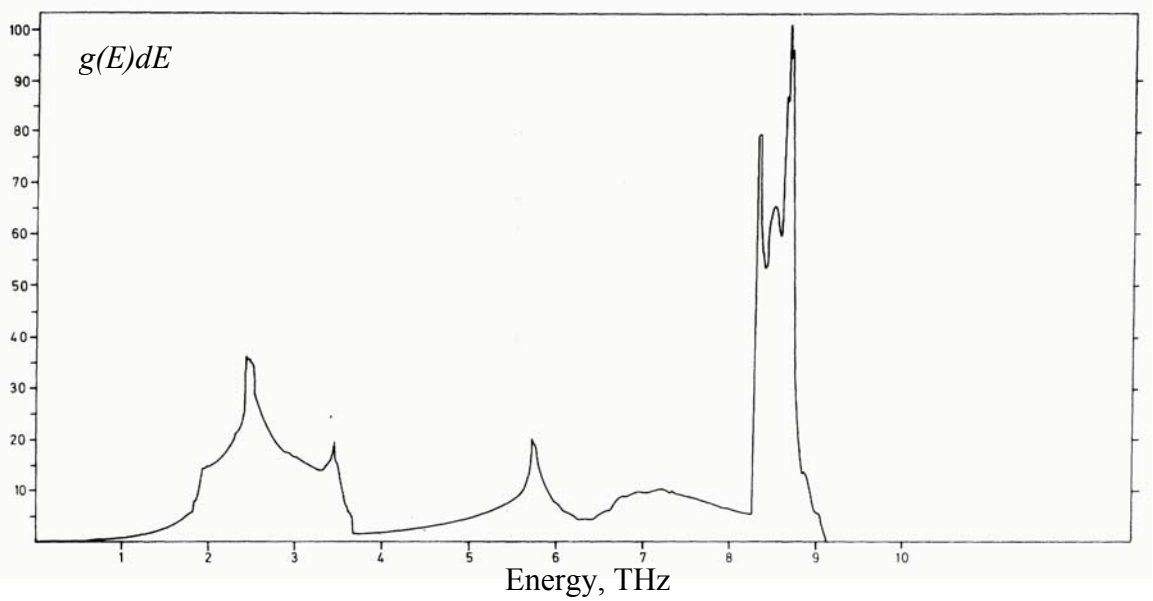

Figure 43: Phonon density of states in germanium (at 80k). From [45].

4.5 Computer-based estimation of the optimum parameters for germanium linewidth measurement on IN3 spectrometer.

The first task for a triple-axis experiment is to calculate the resolution function for a particular spectrometer configuration. There are plenty of computer programs for that, usually based on Cooper-Nathan method [81], [82], [87]. The ResCal [88] routine for MatLab [89] package was chosen to do these calculations. For the phonon dispersion in germanium, experimental data from [45] have been taken. These data represent the phonon dispersion in germanium in the whole range of the irreducible part of the Brillouin zone. In order to handle a continuous function, instead of discrete points only, the experimental data points were interpolated. The scattering cross-section for a particular scattering vector $\boldsymbol{Q}$ is proportional to [90]:

$$\frac{\partial^2 \sigma}{\partial \Omega \, \partial E} \propto \frac{1}{Q} \left| \boldsymbol{Q} \cdot \boldsymbol{\sigma}_1 + \boldsymbol{Q} \cdot \boldsymbol{\sigma}_2 \cdot e^{\pi i \boldsymbol{Q} \boldsymbol{\Delta}} \right|^2 \qquad (4.13)$$

where $\boldsymbol{Q}$ is the momentum transfer (taken in reciprocal lattice units), $\boldsymbol{\sigma}_1$ and $\boldsymbol{\sigma}_2$ vectors of eigen displacements of atom 1 and 2 in the unit cell, $\boldsymbol{\Delta}$ is a position of the second atom in a unit cell with respect to the first one, $\boldsymbol{\Delta}$ is (0.25,0.25,0.25). The vectors of eigen displacements were calculated by the PWscf ab-initio condensed matter code [55], based on the bond-charge model.

Dealing with a particular spectrometer, one has to take its limitation into account. In the case of the IN3 spectrometer one can not go above an energy transfer of more than 8 meV, and the momentum of the incident or scattered neutrons is fixed to be 2.662 $Å^{-1}$. The condition for spin-echo phonon focusing demands that the vector of the group velocity of the phonon should lie in the plane of scattering, because the bootstrap coils evidently can be turned only around a vertical axis. If the phonon group velocity has a non-zero vertical component, bootstraps have to be turned around a horizontal axis. The last constraint limits the phonons for consideration to those ones, which belong to symmetry directions and symmetry planes. Symmetry directions and planes of the irreducible part of the first Brillouin zone of germanium are shown in Figure 41.

The following idea was taken as a base of consideration for optimum points of the phonon linewidth measurements by the combined triple-axis and resonance spin-echo technique. One has to find a point, satisfying the following conditions:

1) The curvature of the dispersion surface inside the resolution ellipsoid should not exceed the characteristic value of the phonon linewidth in germanium. It should approximately be no more than 5 μeV at room temperature [91], [92].

2) The mutual orientation of the vector of the phonon group velocity and the vectors of the velocities of incident and scattered neutrons should be so that the condition of spin-echo phonon focusing (1.48) and (1.53) can be satisfied by tilting of the bootstrap coils.

3) The scattering rate of the chosen phonon vectors $\boldsymbol{Q}$ must be reasonable (not too small).

Here and further we limit our consideration to transverse acoustic phonons because of the reason that the energy transfer is limited to 8 meV, and because the transverse phonons give higher scattering rate then the longitudinal ones. The size of the resolution ellipsoid is taken as the isosurface in (q_x, q_y, E) space, where its Gaussian profile drops to 1/10 of its maximal value:

$$I(Q) \propto e^{-q_i M_{i,j} q_j} \text{ – resolution function,}$$

$$0.1 = e^{-q_i M_{i,j} q_j} \text{ - the isosurface considered.} \qquad (4.14)$$

where $\mathbf{q_i} = \mathbf{q_i^0} - \mathbf{Q_i}$, $\mathbf{q_i^0}$ is the center of the resolution ellipsoid (phonon to be measured), $\mathbf{Q_i}$ is the point where the value of intensity should be estimated, $\mathbf{M_{i,j}}$ is the resolution matrix from Cooper-Nathan calculations.

Some conclusions about optimum points in the irreducible part of the Brillouin zone can be gained by symmetry reasons. Neutron scattering experiments can be performed in one of the high-symmetry planes: the plane **Σ**, **Δ** (Figure 44)**,** the plane **Σ**, **Λ** (Figure 45) and the plane **Λ**, **Δ** (Figure 46)**.**

Symmetry directions (**Σ**, **Λ**, **Δ**) are most informative from the point of view of the exploration of the lattice dynamics, this way scans lying along symmetry directions should be considered first. Along directions **Λ**, **Δ** transverse acoustic phonons are degenerate, but in high symmetry planes, aside from these directions, transverse acoustic phonons are split. The resolution ellipsoid for a phonon belonging to **Λ** and **Δ** directions will intersect with dispersion surfaces aside the symmetry directions, and the resolution ellipsoid will cut a “butterfly” from the dispersion surfaces, as shown in Figure 47. It

means that the energy resolution of the experiment is limited by the energy difference between the surfaces of the two dispersion branches, about 200 – 400 μeV (with q-resolution about 0.05 r.l.u of germanium, depending on the particular phonon) and the spin-echo technique can not be used for linewidth measurements along directions **Λ Δ** (except the cases when q-resolution is dramatically improved by collimation leading to a significant loss of intensity)**.**

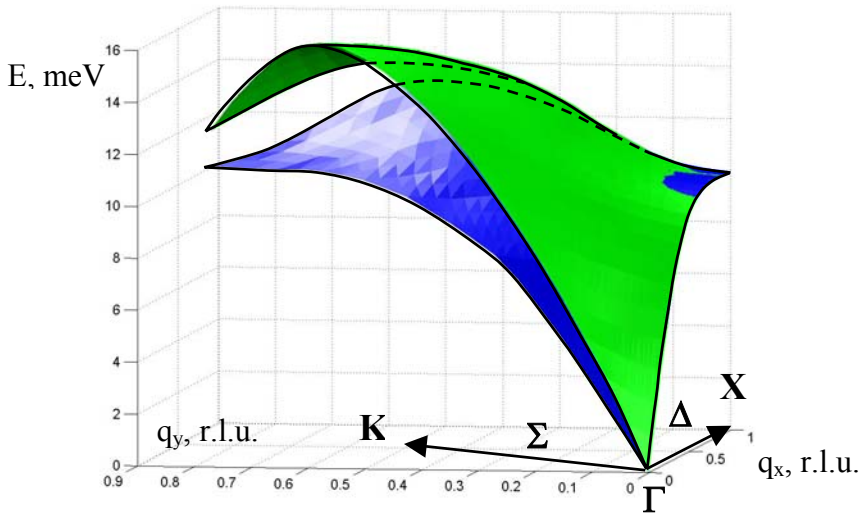

Figure 44: Dispersion surfaces of transverse acoustic phonons in the plane of high symmetry **ΔΣ**. q_x corresponds to [q00] direction, q_y corresponds to [0q0] direction.

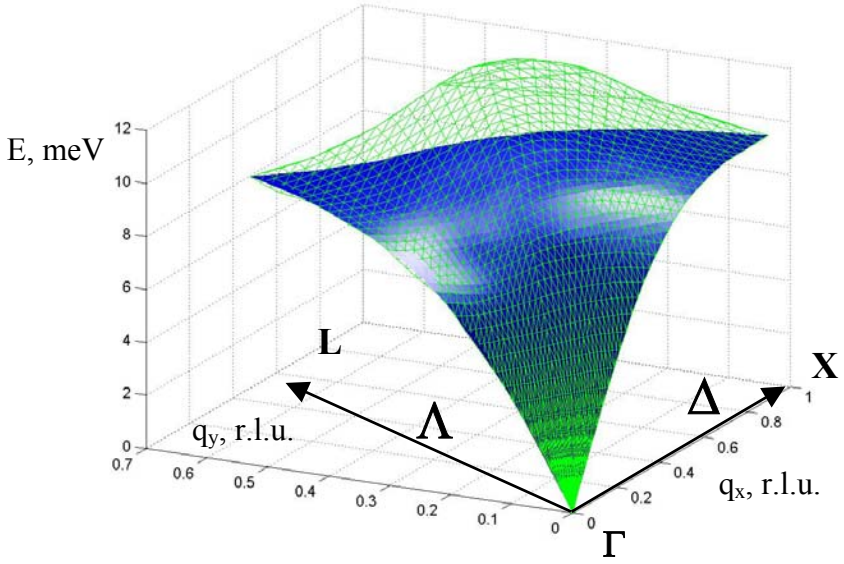

Figure 45: Dispersion surfaces of transverse acoustic phonons on a plane of high symmetry **ΔΛ**. q_x corresponds to [q00] direction, q_y corresponds to [qq0] direction.

Generally one can derive the following phenomenological rule : if two non-degenerate branches intersect with the resolution ellipsoid, the spin-echo energy resolution is limited by the difference between them, and this phonon is not appropriate for a good experiment. Therefore, the **Σ** direction and phonons belonging to planes **ΣΛ** and **ΣΔ** should be considered. But before going into these estimations, let us first consider the results of first spin-echo measurements of phonon linewidths in germanium at the IN3 [93] spectrometer at the ILL with the NRSE option "Zeta" It is done in the next paragraph.

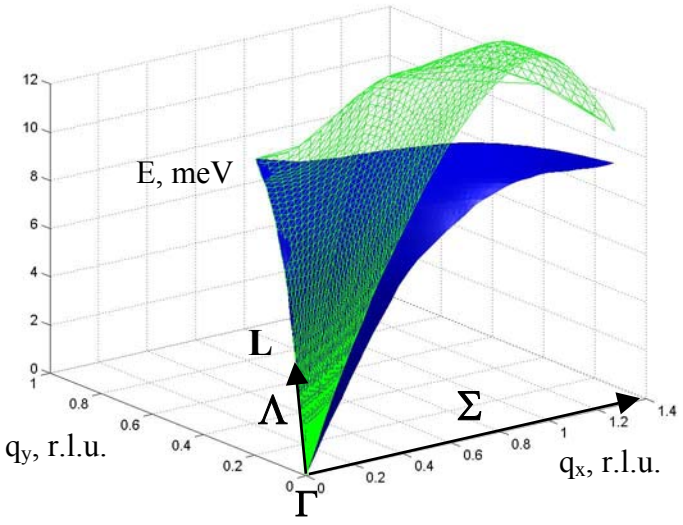

Figure 46: Dispersion surfaces of transverse acoustic phonons on a plane of high symmetry **ΣΛ**. q_x corresponds to [qq0] direction, q_y corresponds to [q00] direction.

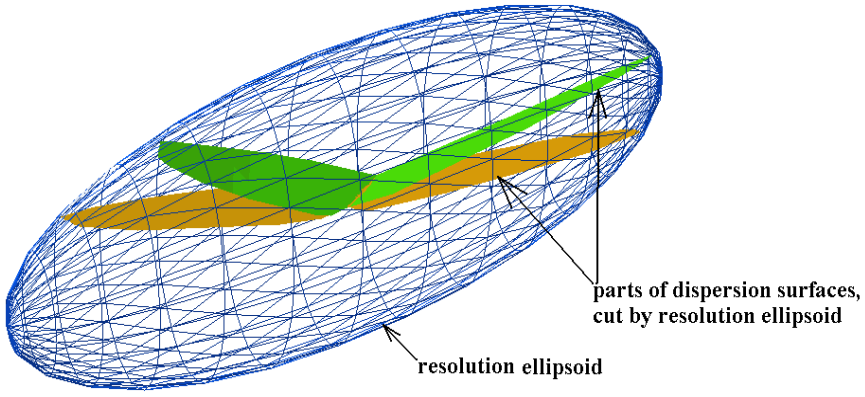

Figure 47: Resolution ellipsoid and parts of dispersion surfaces have been cut by it. The wave vector transfer here is (0.12 2 2), the plane of measurements is **ΔΣ**.

4.6 Results of measurements of phonon linewidth in germanium on IN3-Zeta spectrometer at ILL in November 2001.

The measurements of phonon linewidth in germanium on the IN3-Zeta spectrometer in ILL in November 2001 have been made with a single-crystal kindly supplied by Juri Kulda to determine the transverse acoustic phonon at (0.12, 2, 2) (in reciprocal lattice units), for an energy transfer 3 meV. The measured linewidth was 204 ± 40 μeV, and the level of background was higher than usually. This linewidth is much higher then one expects as linewidth for this phonon. This paragraph is devoted to the explanation of this result.

The experiment has been done with the following setting of the triple-axis spectrometer [94]:

1) The energy transfer for the scattered neutron is considered as negative.
2) The scattering senses are: at the monochromator -1 (to the left from the incident neutron beam direction), at the sample -1 and at the analyzer 1 (to the right from the incident neutron beam to the analyzer direction).
3) The transmission characteristics of Soller beam collimators are given in units of minutes of arc in (Table 4).
4) The scattering plane was chosen to be (100) – (011) (see Figure 48).

Table 4: Values of Soller beam collimators in units of minutes of arc:

	Collimator 1	Collimator 2	Collimator 3	Collimator 4
horizontal	600	40	40	40
vertical	600	600	600	600

This configuration was simulated by means of ResCal routines, and the intersection of the resolution ellipsoid with the dispersion surfaces of acoustic transverse phonons is shown in Figure 49. Only the low energy transverse acoustic branch gives a scattering signal, as only in this plane the polarization vector is coplanar to the plane of scattering [95]. The other transverse dispersion branch gives only background, causing significant experimental error (40 μeV). The points on the dispersion surface, lying inside the resolution ellipsoid were extracted by means of criteria (4.14). Then two planes, parallel to the slope of the dispersion along the Δ direction in the point of measurements

(0.12,0,0), were constructed each passing the point of the dispersion surface, which is maximally distant from the slope plane, and each such a point belong to one of the two half-spaces separated by the slope. These planes (maximal and minimal) are shown in Figure 50.

The value of phonon linewidth obtained in this experiment should corresponds to the difference between these two planes estimated as follows: if planes are defined by equations like:

$$E = \Phi(q_x,q_y), \qquad (4.15)$$

then the estimation for the experimental result can be written as:

$$\Gamma = |\Phi_2(0,0) - \Phi_1(0,0)|, \qquad (4.16)$$

where Φ_2 and Φ_1 are the equations corresponding to the maximal and minimal planes (as in Figure 50).

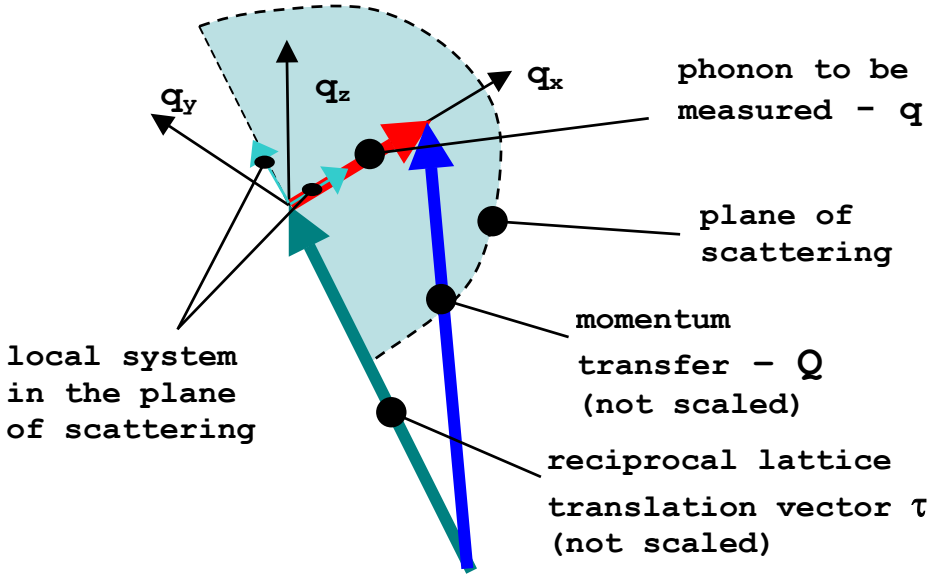

Figure 48. Vector diagram describing the experiment. Scattering plane chosen for the experiment, reciprocal coordinate system of crystal is also drawn.

Estimated as above, this value gives 242.1 μeV. It is in good agreement with the value obtained in the experiment. This value definitely does not correspond to the linewidth, but can be explained as net curvature of that part of the dispersion surface, which is intersecting the resolution ellipsoid.

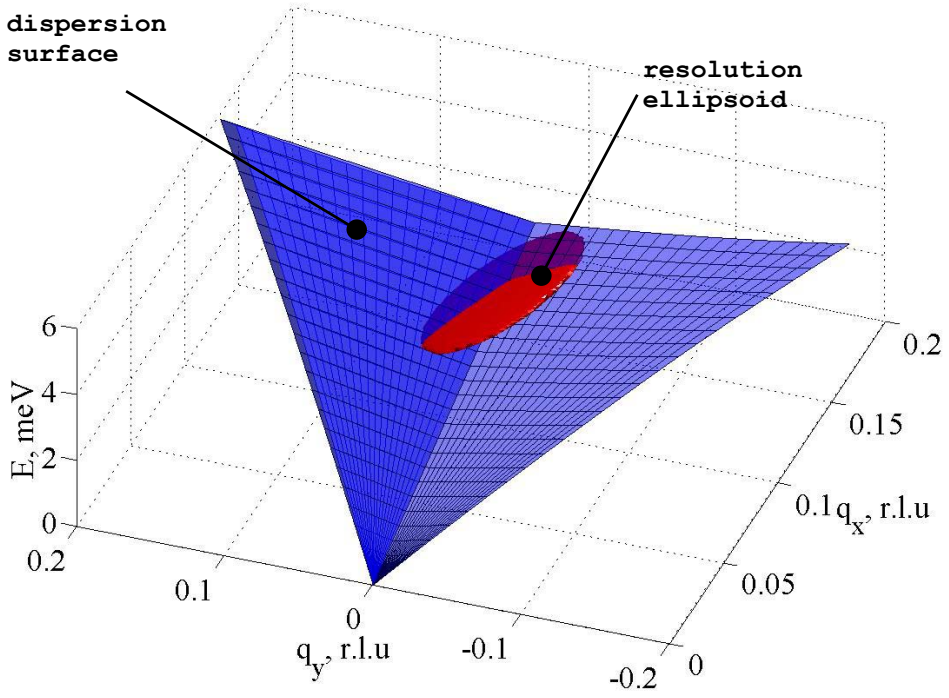

Figure 49: Dispersion surface of the low energy transverse acoustic mode intersecting with the resolution ellipsoid at the point of measurement.

In this particular point of measurements, lying in high-symmetry direction, the curvature is rather high, and the surface is most curved along the direction perpendicular to this high symmetry direction. This situation is common for any high-symmetry direction in the energy region less then 8 meV, and confirms the conclusion from in the previous paragraph that phonons on high-symmetry direction are not well suited for high energy resolution measurement by the NRSE technique. The obtained agreement between experimental result and the calculated value of the energy resolution limit allows to apply the described approach to the estimation of the optimal phonon and experimental parameters for measurements of phonon linewidths by the NRSE technique.

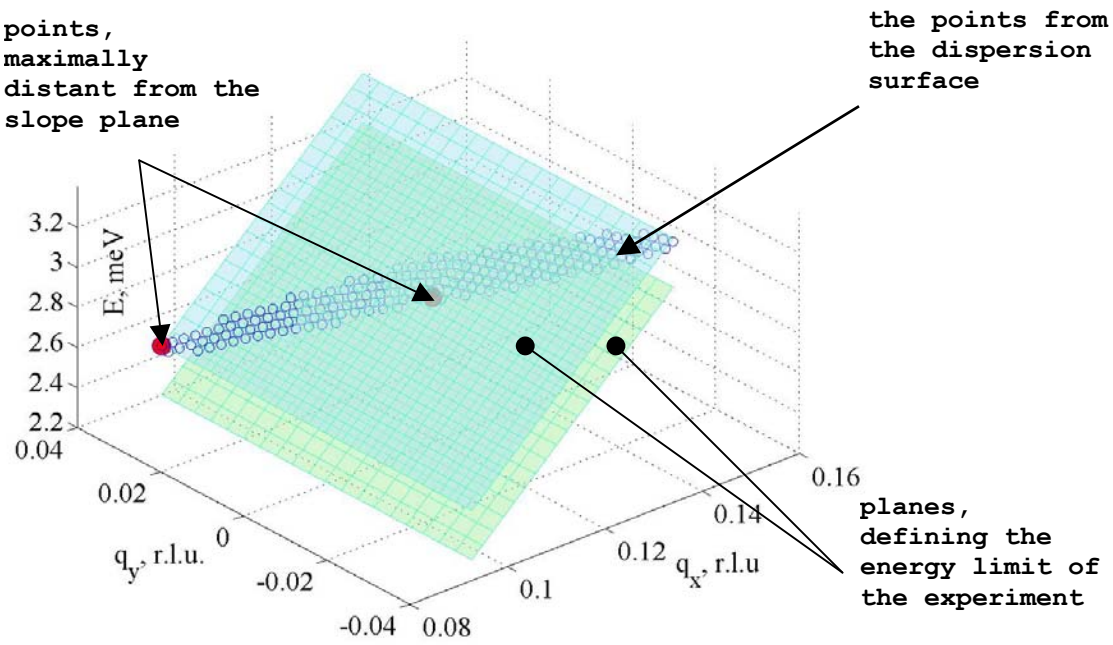

Figure 50: The part of dispersion surface of the low energy transverse acoustic mode intersected with resolution ellipsoid (shown by blue empty circles). Planes, defining the NRSE energy limit of measurements are drawn semi-transparent. The points used for the construction of these planes are drawn by solid red circles.

4.7 Consideration of the possibility to perform linewidth measurements on acoustic phonons in the Σ high-symmetry direction.

Acoustic transverse phonons are non-degenerate along the high-symmetry **Σ** direction, allowing to choose the phonon for measurements such that the resolution ellipsoid centered at the point of the measurement (at chosen triple-axis spectrometer configuration) intersects only with a single dispersion surface. The constraint of intersecting only with one dispersion surface limits us to choose the phonon far from the center of the Brillouin zone. On the other hand, the IN3 triple axis spectrometer is limited to a maximum energy of 8 meV[96]. Because of this constraints the points (0, 0.2, 0.2), 5.34 meV and (0, 0.3, 0.3) 7.53 meV were chosen, which correspond to the low energy transverse acoustic mode. Let us first consider the phonon (0, 0.2, 0.2). As it is a transverse phonon, its τ vector should be perpendicular to the vector $\boldsymbol{q}$ and the momentum transfer vector $\boldsymbol{Q}$ is taken to be (0, -1.8, 2.2). The intersection of the resolution ellipsoid

with the dispersion surface along the scattering plane (010)-(001) is shown in Figure 51. The triple-axis settings for this particular orientation of the resolution ellipsoid in Figure 51 are the following: the mosaic of monochromator and analyzer are taken as 30', mosaic of the sample is takes as 1°. The scattering senses are taken as "-1", "-1", "1" (on monochromator, sample and analyzer, respectively), the neutron energy transfer is taken negative and the energy of the scattered neutrons is kept fixed at $k_f = 2.662$ Å^{-1}.

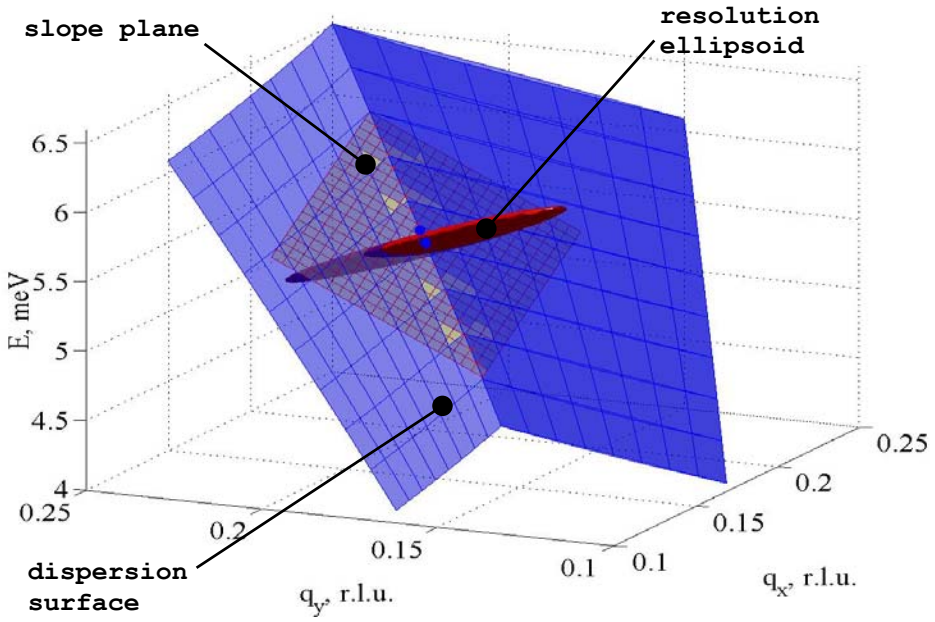

Figure 51: Dispersion surface of the low energy transverse acoustic mode intersected with the resolution ellipsoid. q_x corresponds to the [010] direction, q_y corresponds to [001] direction. Yellow spots on this figure are caused by features of computer drawing.

The obtained value for the NRSE energy resolution limit (calculated in the manner described in the previous paragraph) is 0.3195 meV. The planes defining the energy resolution limit are shown in Figure 52. The value of 0.3195 meV is too high for the phonon (0, 0.2, 0.2), 5.34 meV could be proposed for the neutron scattering experiment. Simulations at different triple-axis spectrometer settings at which the same phonon is measured have been done and their results are shown in the Table 5. Scattering senses and the sign of the neutron energy transfer have been varied. Simulations of the same kind have been done for the (0, 0.3, 0.3), 7.53 meV phonon also. The results are shown in Table 6.

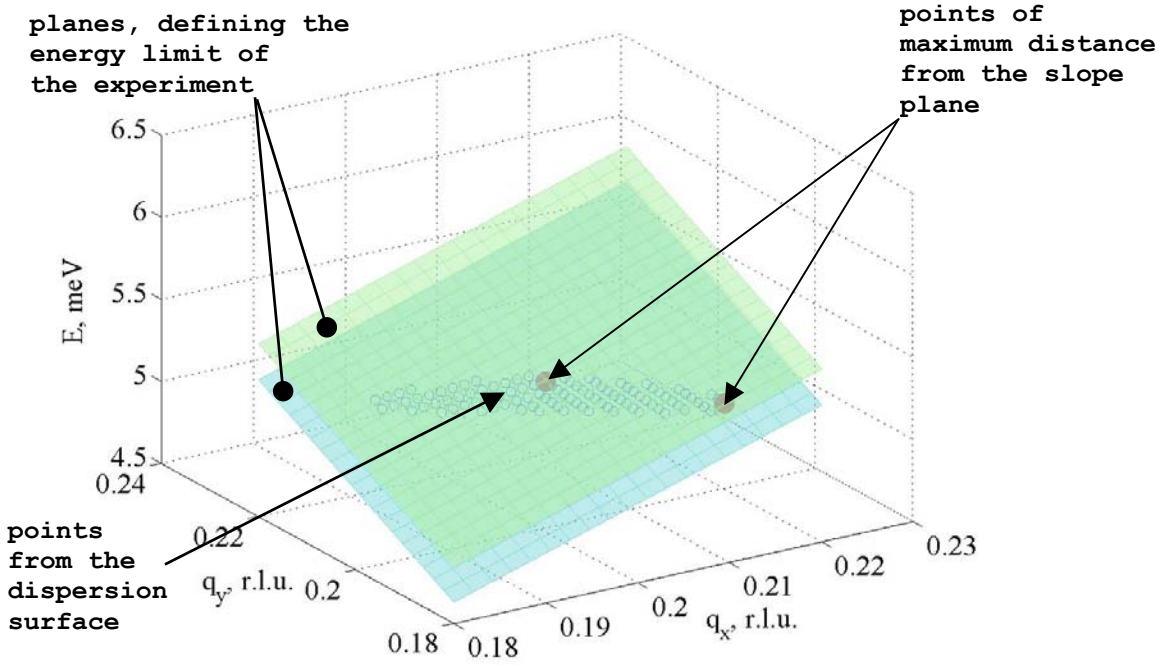

Figure 52: Part of dispersion surface of the low energy transverse acoustic mode intersected with the resolution ellipsoid (shown by blue empty circles). Planes, defining the energy limit of measurements are drawn semi-transparent. The points used for the construction of these planes are drawn by solid red circles.

Table 5: Results of the calculations on the estimation of the limit of the energy resolution limit for the phonon (0, 0.2, 0.2), 5.34 meV

A*	-	+	-	+	-	+	-	+
B*	--+	--+	-++	-++	+++	+++	---	---
C*	0.3195	0.6176	0.4220	0.4834	0.2861	0.6055	0.3813	0.5715

A here and further in tables is the sign of the energy transfer, B are the scattering senses on the monochromator, on sample and on analyzer respectively. C is the calculated energy resolution in meV.

Table 5 continued.

A	-	+	-	+	-	+
B	+-+	+-+	+--	+--	++-	++-
C	0.2319	0.3750	0.3255	0.5264	0.3893	0.3763

Table 6 Results of the calculations on the estimation of the limit of the energy resolution limit for the phonon (0, 0.3, 0.3), 7.53 meV

A	-	+	-	+	-	+	-	+
B	--+	--+	-++	-++	+++	+++	---	---
C	0.0993	0.1573	0.1031	0.2034	0.0715	0.2648	0.1171	0.2058

Table 6, continued.

A	-	+	-	+	-	+
B	+-+	+-+	+--	+--	++-	++-
C	0.0778	0.1047	0.1365	0.1832	0.1365	0.1832

The values shown in the Table 5 and 6 have been obtained for the following other triple-axis spectrometer settings: the mosaic of monochromator and analyzer are 35', sample mosaic is taken as 1°, all Soller collimators are taken as 40' of arc. The energy of the scattered neutrons is kept fixed at q = 2.662 $Å^{-1}$.

As one can see from Table 5 and Table 6, the obtained values for the energy resolution are not good enough to be proposed for the scattering experiment. The reason for that is the same as for to the experimental result in the previous paragraph. In the vicinity of the high symmetry direction, the dispersion surface is mostly curved along the direction perpendicular to this high symmetry direction. And, more important, the sign of the surface curvature changes after crossing the high-symmetry direction. This conclusion makes phonons of high symmetry non-acceptable to be proposed for the high energy resolution measurement by means of the united triples axis and spin-echo technique. The next paragraphs are devoted to the consideration of asymmetry phonons for NRSE measurements.

4.8 Consideration of the possibility to perform linewidth measurements of acoustic phonons in the ΣΔ symmetry plane.

For phonons, not belonging to the high symmetry directions , special care should be taken on the intensity in a TAS-experiment. The dependence of the scattered intensity (or of the form factor) from the mutual orientation of the vector of neutron momentum transfer and eigen displacements of atoms in the crystal lattice is given by equation (4.13). On the other hand, one also should take care on spin-echo phonon focusing conditions, given in paragraph 1.2 (this problem is thoroughly discussed in [2]). This paragraph is devoted to such a consideration for phonons in the **ΣΔ** plane. Consider Figure 53, where the low-energetic transverse acoustic phonon branch is shown together with the resolution ellipsoid for the phonon (0, 0.2, 0.25), 6.27 meV. The **τ** vector here is taken as (0, -2 2). The triple axis settings for this orientation of the resolution ellipsoid are the following: the mosaic of monochromator and analyzer are taken to be 30', mosaic of the sample is taken to be 1°.

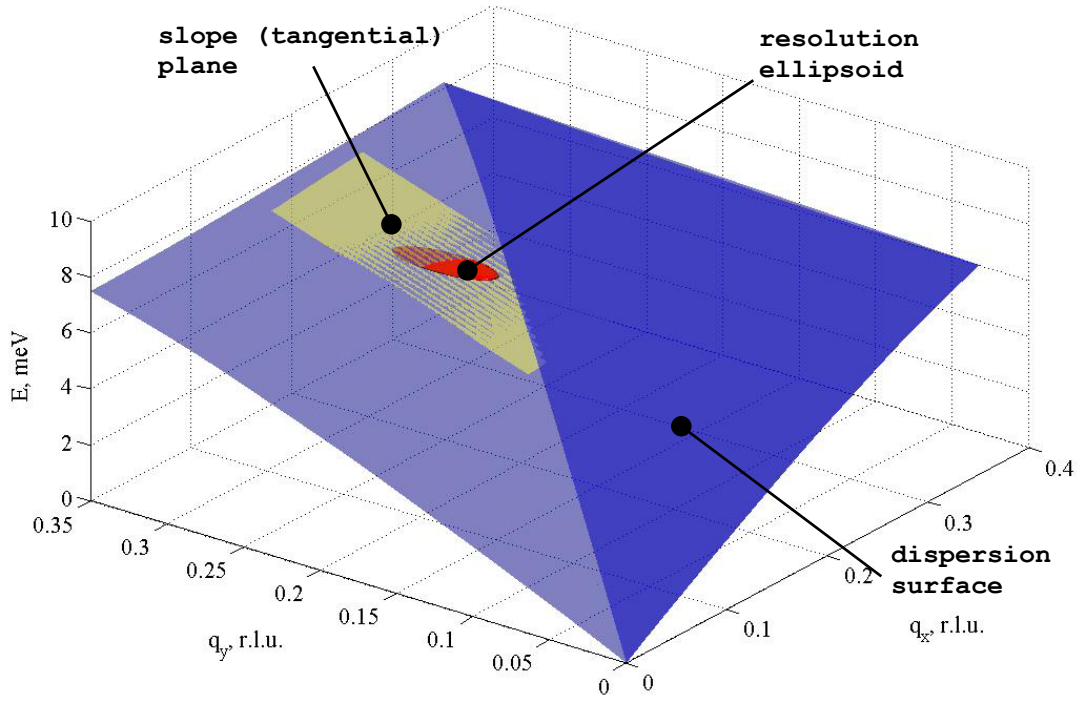

Figure 53: Dispersion surface of the low energy transverse acoustic mode intersected with the resolution ellipsoid. q_x corresponds to the [010] direction, q_y corresponds to [001] direction.

The scattering senses are taken to be “-1”, “-1”, “1” (on monochromator, sample and analyzer, respectively), the neutron energy transfer is taken negative and the energy of the scattered neutrons is kept fixed to $k_f = 2.662$ Å^{-1}.

The spin-echo energy resolution limit was estimated to be 2.5 μeV. This estimation has been obtained in the following manner: a plane, tangential to the dispersion surface in the point (0, 0.2, 0.25) is constructed by fitting an equation of the form $E = A \cdot q_x + B \cdot q_y + D$ to the points of the dispersion surface residing inside the resolution ellipsoid (which are taken by criteria (4.14)). The components of this surface actually are the components of the phonon group velocity **C** (A is C_x, B is C_y, C_z is zero here because the phonon (0, 0.2, 0.25), 6.27 meV belongs to the symmetry plane **ΣΔ**). Then planes passing through the points, maximally distant from the slope plane, and parallel to it were constructed. With the aid of them in a manner given by equation (4.16) the limit of the spin-echo energy resolution in this point was estimated. This discussion is illustrated by Figure 54.

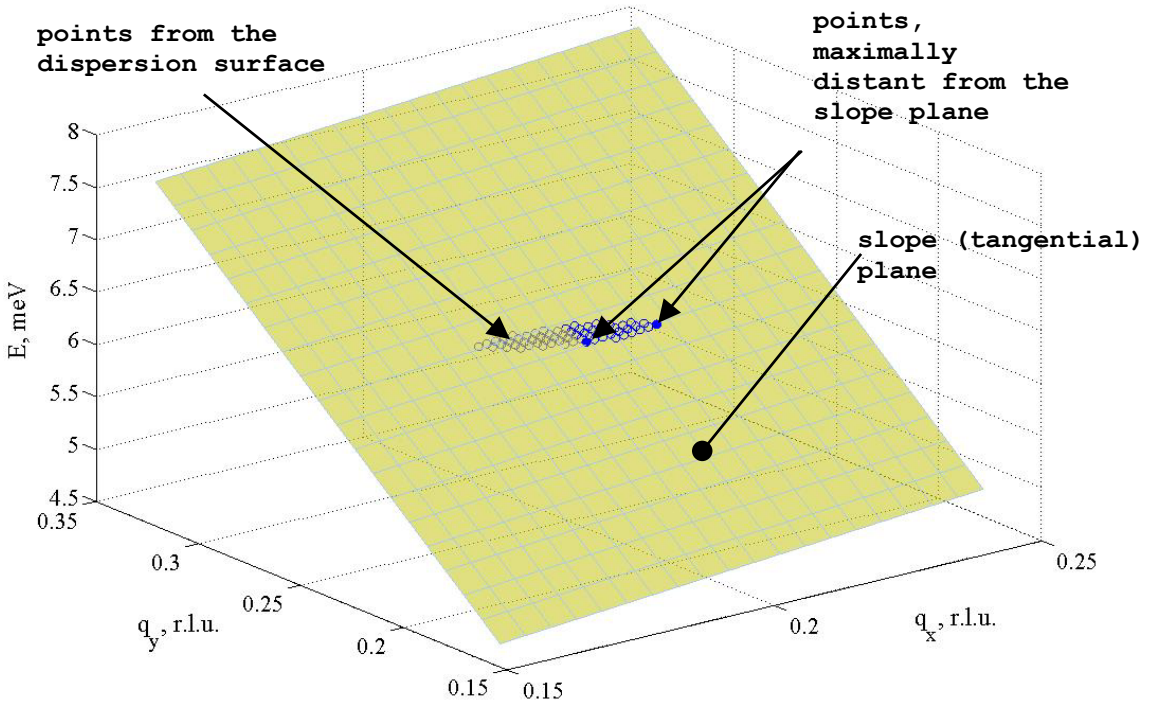

Figure 54: The point from the dispersion surface resided inside the resolution ellipsoid and the tangential plane in the point (0, 0.2, 0.25). q_x corresponds to the (010) direction, q_y corresponds to (001) direction.

The next problem to be considered here is the possibility to tilt the NRSE bootstrap coils to satisfy the spin-echo phonon focusing conditions (1.48) and (1.53). The limit of

the NRSE bootstrap coils tilt angle for the spectrometer IN3 is about 50º. The mutual orientation of the velocities of the incident and scattered neutrons and the phonon group velocity is shown in Figure 55. The $\mathbf{C_x}$, $\mathbf{C_y}$ values of the phonon group velocity here are (724.8, 3285.5) m/s.

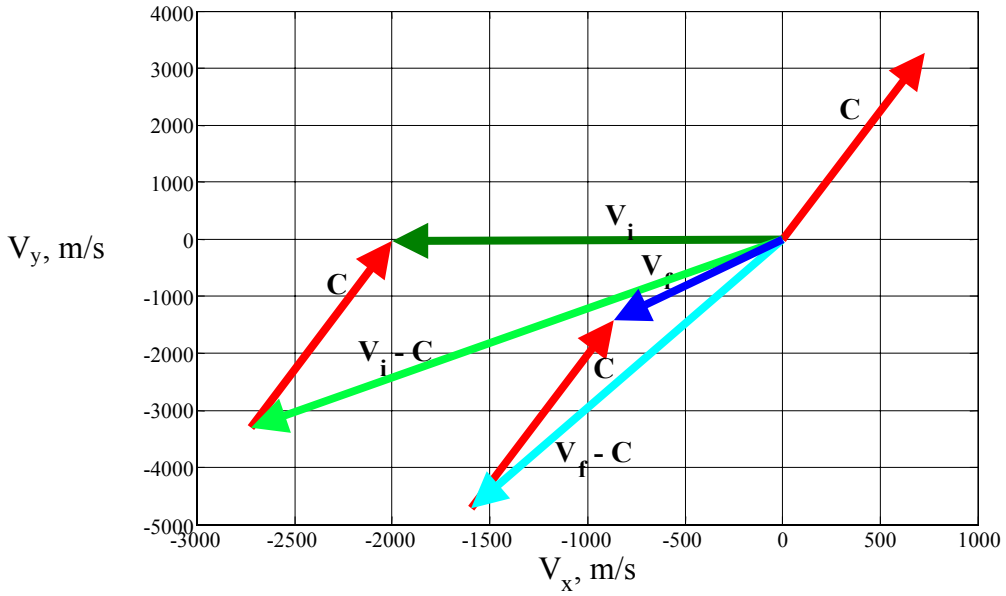

Figure 55: Mutual orientation of the phonon group velocity **C** vector in the point of estimation (0, 0.2, 0.25), 6.27 meV and vectors of the velocities of incident $\mathbf{V_i}$ and scattered neutrons $\mathbf{V_f}$.

The normal vectors of the bootstrap coils must be parallel to the vectors $\mathbf{V_i - C}$ (in the first arm) and to $\mathbf{V_f - C}$ (in the second arm). In this way coils in the first arm must be turned to the angle 49.31º counterclockwise (seen from the top), and in the second arm to the angle 8.28º counterclockwise. The angle of tilting 8.28º is easily achievable, but the angle 49.31º is just at the limit of capabilities of the spectrometer, but nevertheless it is acceptable. One can see from the Figure 53, that the dispersion surface in the vicinity of the point (0, 0.2, 0.25) is rather flat and this region can be considered to be acceptable for high-resolution spin-echo measurements.

Because of the IN3 spectrometer configuration, either the incident or the final wave vector is fixed to a value of 2.662 $Å^{-1}$. $\mathbf{k_f}$, and thus $\mathbf{V_f}$, are chosen fixed. But we can vary vector $\mathbf{V_i}$ by changing the value of the neutron energy transfer (what means we will measure another phonon). If we increase $\mathbf{V_i}$ we should get a smaller tilt angle for the first

arm. We consider in following the phonon (0 0.25 0.3), 7.27 meV. Calculations of the same kind as above have been done for it. They shown that for this phonon the limit of the spin-echo energy resolution is 8.2 μeV (which is done as for the previous phonon), but the tiling angles are as follows: in the first arm 42.66º counterclockwise (if seen from the top), and in the second arm at the angle 10.68º counterclockwise. These values are appreciable to be proposed for the experiment.

Another problem in estimation of the optimum parameters for phonon linewidth measurements consists in the necessity to consider the mutual orientation of the vector of the neutron momentum transfer in and vectors of the atomic eigendisplacement. The factor in the scattering rate for that is given by equation (4.13). Eigenvectors for the phonons (0, 0.2, 0.25), 6.27 meV and (0 0.25 0.3), 7.2735 meV have been calculated by means of the PWscf ab-initio package. The factor (4.13) was approximately 1.36 for both (one could compare this values with value of the factor (4.13) obtained for the phonon considered in paragraph 4.6 of this manuscript) . The last fact allows to expect reasonable scattering rates for both of these phonons. In this way they really could be proposed for the neutron scattering measurements.

4.9 Consideration of the possibility to perform linewidth measurements of acoustic phonons in the ΣΛ symmetry plane.

Within the **ΣΛ**plane (as also in **ΣΔ**), transverse acoustic phonons in germanium are non-degenerate. This fact opens the possibility of linewidth measurements by triple-axis and spin-echo techniques. In this plane the eigen displacements of the atoms of the lower energy transverse acoustic phonon branch in germanium are perpendicular to this plane. Therefore, it is impossible to perform neutron scattering on phonons belonging to this plane. This way we have to consider here another transverse branch , where the eigen displacements are coplanar to the plane. This is the branch of higher energy, what makes the limitation for the neutron energy transfer of 8 meV more crucial.

Consider the phonon (-0.08 0.22 0.22), 6.74 meV. The τ vector here is taken as (-2, 0 ,0). The triple-axis settings to estimate the limit of energy resolution for this phonon are as follows: the mosaicities of the monochromator and crystal are taken as 30', the mosaicity of the sample is taken as 1°. All the Soller collimators are chosen to be 40 minutes of arc, the energy of the scattered neutrons is kept fixed, the neutron energy

transfer is taken to be negative. The scattering senses are taken as “1”, ‘1”, “-1” (on the monochromator, sample and analyzer, respectively). The plane of scattering is chosen to be [100]-[011]. These parameters will be the same for all phonons discussed in this paragraph. The dispersion surface together with the resolution ellipsoid is drawn in Figure 56.

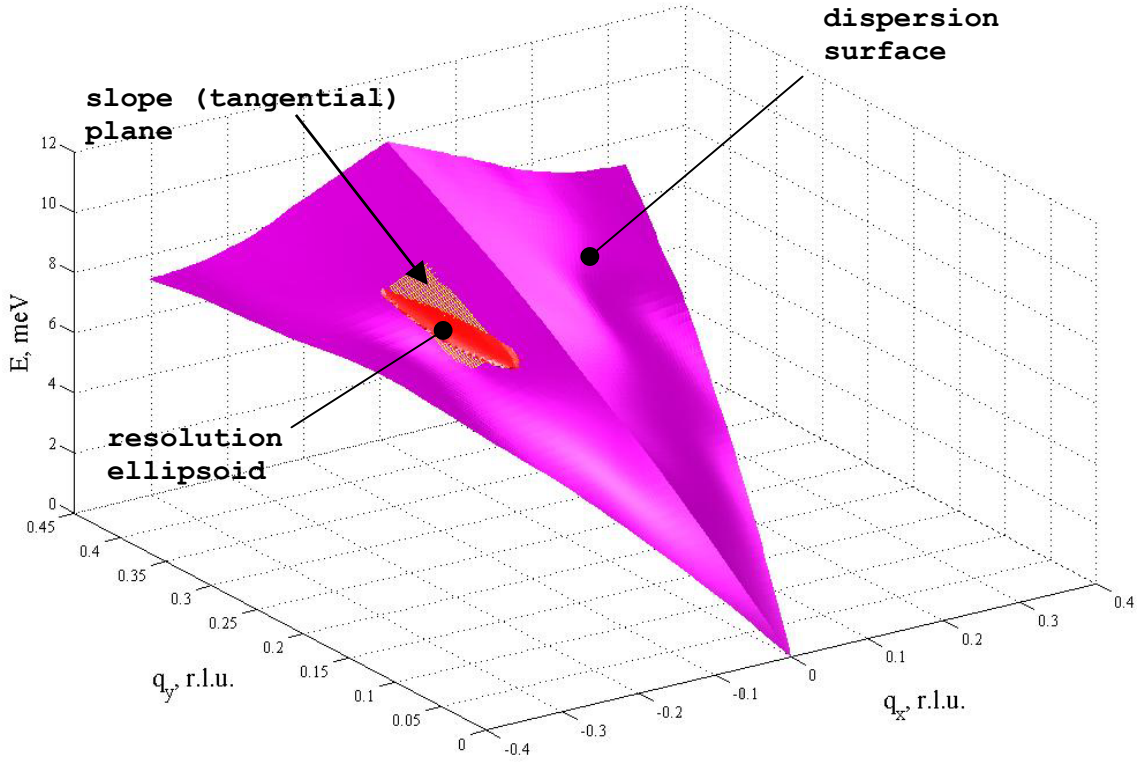

Figure 56: Dispersion surface of the lower energy transverse acoustic phonons along the **ΣΛ** plane. The resolution ellipsoid and the slope (tangential) plane in the point of estimation are (-0.08 0.22 0.22), 6.74 meV. The q_x axis corresponds here to [100] direction, q_y corresponds to [011] direction.

The energy resolution for this phonon, estimated on the base of the triple axis parameters given above, is 203.2 μeV. This value is too big to propose this phonon for an experiment. It is important to note, that in here the resolution ellipsoid is oriented parallel to the dispersion surface, what is called triple-axis phonon focusing. Here a large region of the dispersion surface resides inside the resolution ellipsoid, and this is the main cause of the high value for the energy resolution limit. This problem could be solved by choosing the scattering plane to be (100)-(0-11), where the ellipsoid would be oriented in the anti-focusing way. However the resolution ellipsoid would intersect with the other

transverse acoustic branch, what would lead to a significant increase of the scattering background and should be avoided.

The energy resolution can be reduced only by the higher collimations, reducing the q-width of the resolution ellipsoid. This can be achieved by reducing the Soller collimation and by choosing different scattering senses. Anti-focusing orientation of the resolution ellipsoid can be achieved with the "-1", "-1", "-1" configuration. The estimation of the energy resolution for the phonon (-0.04, 0.24 0.24), 7.72 meV obtained with Soller collimators of 20 minutes of arc, gave 8.3 μeV. This value is acceptably low. The intersection of resolution ellipsoid with the dispersion surface in the point of consideration is given in Figure 57. The phonon considered opens a very good possibility for spin-echo phonon focusing. The vector diagram describing the possibility to satisfy the spin-echo focusing conditions (1.48) and (1.53) is shown in Figure 58.

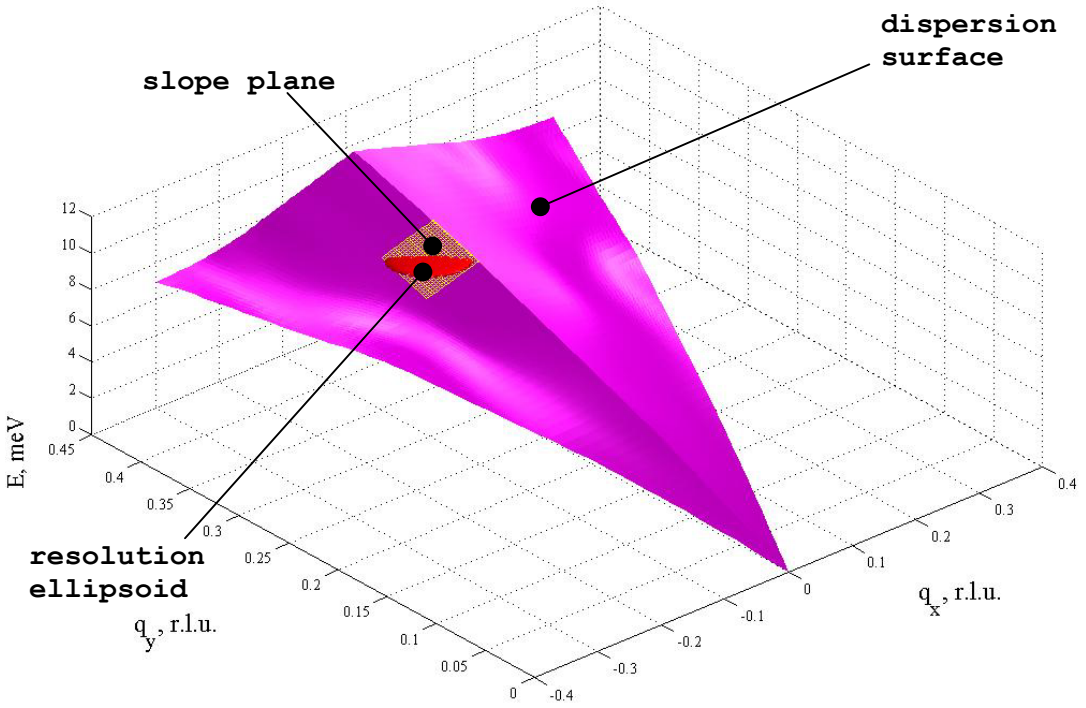

Figure 57: Dispersion surface of the lower energy transverse acoustic phonons in the **ΣΛ** plane. The resolution ellipsoid and the slope (tangential) plane in the point of estimation are (-0.04, 0.24 0.24), 7.72 meV .The q_x axis corresponds here to [100] direction, q_y corresponds to [011] direction.

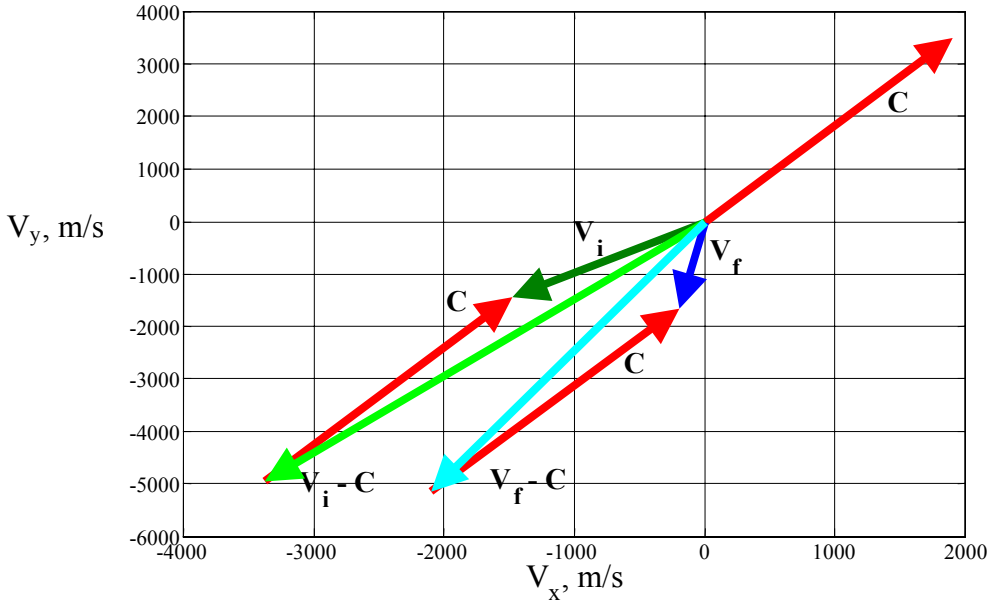

Figure 58: Mutual orientation of vectors of velocities of incoming neutrons $\mathbf{V_i}$ and scattered neutrons $\mathbf{V_f}$ and vector of the phonon group velocity **C**.

The angles for bootstrap coil tilting here are the following: for the first arm 11.39º counterclockwise, for the second one 15.3413º clockwise.

One should also take into account the factor in the scattering cross-section given by equation (4.13), representing the mutual orientation of the vector of the neutron momentum transfer and vectors of the atomic eigen displacements. Eigenvectors for the phonon (-0.04, 0.24 0.24), 7.72 meV have been calculated by means of the PWscf ab-initio package. The value of factor (4.3) for this phonon is 0.54. This value is reasonably good and the phonon (-0.04, 0.24 0.24), 7.72 meV can be proposed for the real neutron scattering experiment.

Summary.

This work is devoted to neutron spin echo and neutron resonant spin echo instrumentation and research.

In the first chapter we describe the basic theory of the methods of neutron spin echo and neutron resonant spin echo. We focus on the very basics of the Spin-Echo (paragraph 1.1), on methods used for studying non-dispersive excitations (like lattice dynamics in glasses), and also on the methods of exploration of the lattice dynamical properties of ordered systems, like bulk crystals. The measurement of phonons in crystals demands tilting of the magnetic fields boundaries, what is explained in paragraph 1.2. In paragraph 1.3 we give the basics of the neutron resonant spin echo with a complete description of the bootstrap technique. We do not pretend to give the full theory of the neutron spin echo, for the details about spin echo, we propose, for example, book [3].

In the second chapter we present calculations to improve the performance of the coils for spin echo. The results in paragraph 2.1 prove the possibility to wind coils not only from a flat tape, but also from wire with round cross-section. Static field coils wound by round wire are successfully being used in the ZETA NRSE option of the IN3 triple-axis spectrometer at the ILL. The results of paragraph 2.2 give good advise how to optimize the bootstrap geometry for better performance. Some of them (like increasing of the thickness of the outer mu-metal shield of the bootstrap coil pair to 1 mm) are also taken into account on IN3-ZETA at the ILL, what resulted in an improvement of the spectrometer performance.

The third chapter is devoted to the design study of a multi angle neutron resonance spectrometer. In paragraph 3.1 the derivation of the MIEZE-2 principle is derived from the quantum-mechanical point of view and the basic idea of a multi angle neutron resonance spectrometer is given. In paragraph 3.2 we show the results of ray-tracing simulations to optimize the neutron beam intensity on the detector. This basic estimate demonstrates that a spherical mirror can give appreciable focusing of neutron paths onto the detector with high path length homogeneity, what allows to use focusing geometry for the MIEZE-2 technique. In paragraph 3.3 we present results of the curved static field coil for the curved bootstrap coils. The Boundary Element Method is used for modeling its magnetic field. Simulations show that curved bootstrap coils will show good

performance with rather small losses of polarization, because the leakage fields outside of bootstrap are small. The magnetic field inside of the coils will be enough homogeneous to make nearly perfect spin-flips. In paragraph 3.4 we estimate the performance of the curved RF-field coil. We did it in a purely analytical way, making the results free from iteration errors. As a result we conclude that a multi angle neutron resonance spectrometer is possible and that the curved geometry does not lead to significant losses of polarization in comparison with a corresponding flat geometry. The focusing geometry gives a significant increase of beam intensity on the detector, making the construction of a multi angle neutron resonance spectrometer highly favorable.

The fourth chapter is devoted to measurements of phonon linewidths in germanium by means of the united TAS-NRSE techniques. Paragraph 4.1 gives the survey of the theoretical and experimental results obtained on phonon lifetimes, paragraph 4.2 provides an overview of the triple-axis technique. In paragraph 4.3 we consider the combination of the TAS and NRSE techniques for measuring of phonons in bulk crystals. The paragraph 4.4 is devoted to the basic data about germanium. In paragraph 4.5 we derive the conditions for the computer-based estimation of the optimum parameters for germanium linewidth measurement on IN3 spectrometer at the ILL. The next paragraph 4.6 is devoted to measurements of phonon linewidths in germanium on IN3-Zeta spectrometer at ILL in November 2001. Our explanation of the experimental result is in good agreement with experiment. In paragraphs 4.7-4.9 we estimate the optimum parameters for the measurements of phonon linewidths in germanium. We conclude that such measurements are hardly possible for phonons in high-symmetry directions because of the high curvature of the dispersion surface across high symmetry direction. However, they are possible for phonons belonging to symmetry planes. We demonstrate how such estimation can be done. Presently an energy resolution of about 2.5 μeV can be achieved. We show the parameters of the spectrometer configuration to reach this energy resolution, and estimate the scattering intensities which could be reached in TAS measurements.

In the appendixes we derive general data and results having no direct connection to the NSE-NRSE techniques themselves, but are widely used in simulating the magnetic coil performance for spectrometers. We present some new ideas, those are not been completed yet, and present a design for the high-precision coil for the MUPAD project at the ILL.

Appendix A. Mu-metal and its shielding properties.

The word mu-metal, like Xerox, being a registered trade name of Magnetic Shielding Corporation, is a common name for ferromagnetic soft materials, being used for magnetic field screening. Mu-metal is an alloy of the following composition: Ni – 77%Fe - 14%Cu - 5% Mo – 4%. The main feature of mu-metal is the ability to absorb magnetic energy without retaining it. Namely, mu-metal draws the external magnetic field inside of itself when the external field is on, and has a vanishing remanent magnetization. A typical picture of magnetic flux lines is given in Figure A1

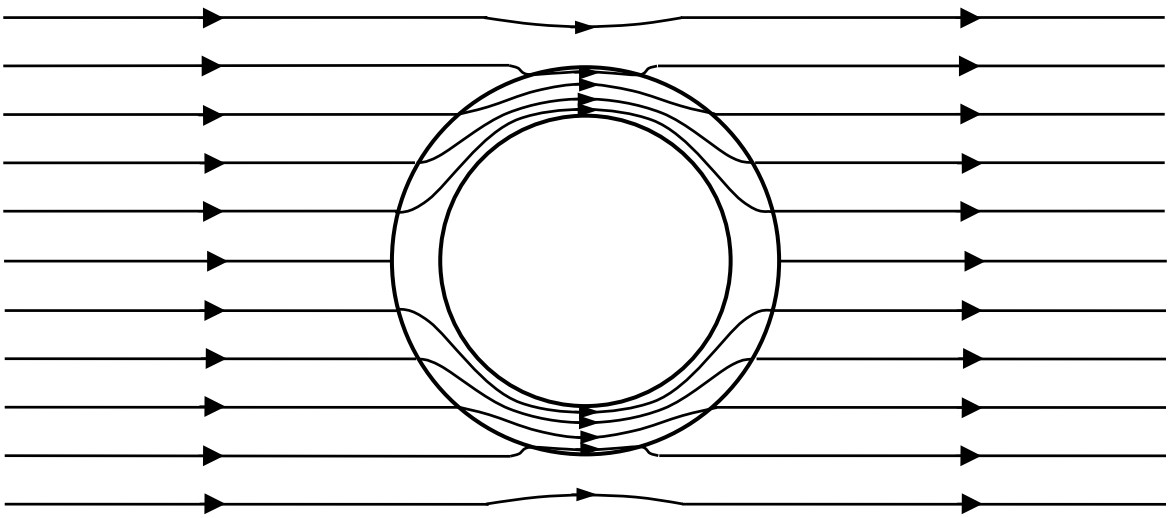

Figure A1: Pattern of magnetic flux lines in the presence of a mu-metal tube. It is considered that in the absence of the mu-metal tube all flux lines would be straight.

It is important to note that shielding action of mu-metal exits only if mu-metal is far away from the saturation (when it just can't absorb more magnetic field that it has absorbed already), see Figure A2.

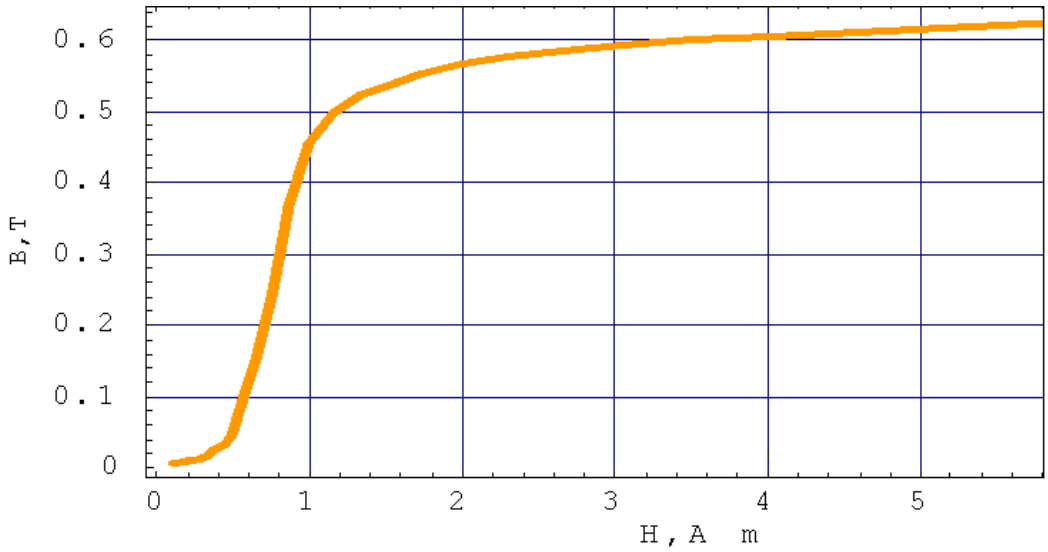

Figure A2: Magnetization curve of mu-metal. This dependence has been used in all simulations of this thesis.

The shielding effect of mu-metal is quite significant, but not perfect. Some magnetic field will exist inside of the shielded volume. For the field inside of an infinite mu-metal tube there is a reduction coefficient with respect to the field value as it would be in the absence of mu-metal tube (it is considered that in absence of mu-metal the magnetic field is homogeneous). In the case of a long tube, the reduction coefficient A can be written as follows:

$$A = \frac{\mu}{4} \cdot \left(1 - \frac{R_i}{R_o}\right) \qquad \text{(A.1)}$$

where R_i is the inner radius of the shield, R_o is the outer radius of the shield, μ is permeability. The last formula is taken from [97], where formulas for the shielding effect of double and triple layer tubes can be found.

Appendix B. Alternative way to manufacture coils.

The usual way to make a coil is to wind it with wire or band around some base, defining the geometry of the coil by hand or by a special winding machine. Being very simple from the manufacturing point of view this approach has a significant drawback: even slight mistakes in winding (like inhomogeneity of distance between the winding, the difference of strength applied to one winding in comparison to another one) makes the wound coil inapplicable for us in a scientific instrument, because such mistakes make the magnetic field of the coil too inhomogeneous.

The other approach consists of the following idea: The aluminum base for the coil is covered with an insulating layer of aluminum oxide and subsequently coved by a layer of conductor (aluminum). The coating process can be done in principle by a variety of technologies; one of them is evaporation technology [98]. The pilot example of such a coil has been manufactured at the Baltic Equipment Factory [99], St-Petersburg, Russia. The photo of it and a schematic drawing are given in Figure B1.

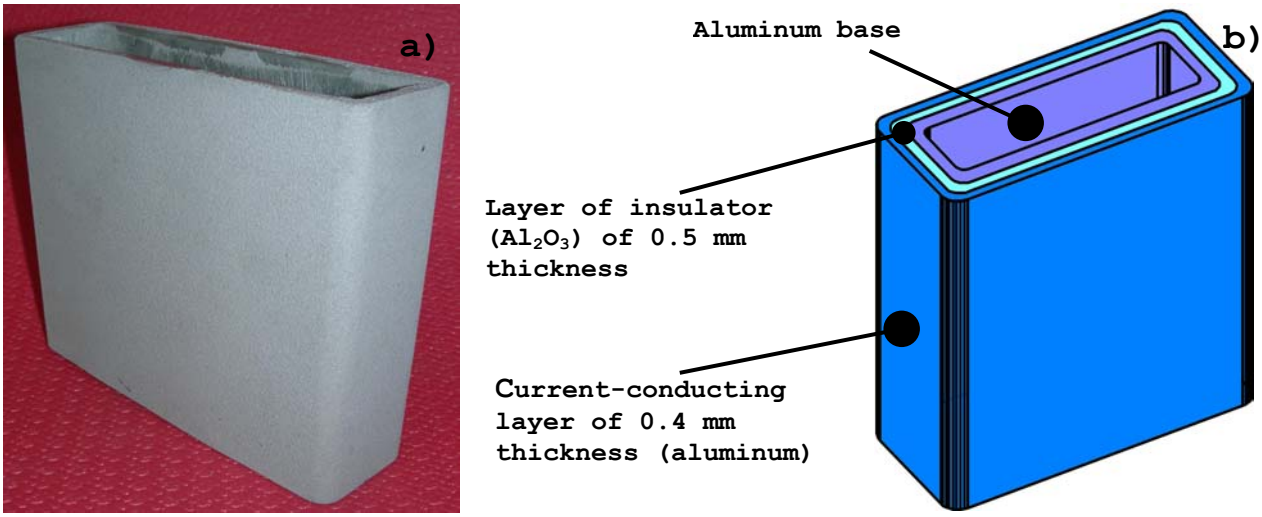

Figure B1: a) Photo of the coil made by evaporation technology; b) the schematic drawing.

The coil shown in Figure B1 represents not yet a coil ready to use. The next step is to cut the layer of aluminum by laser to make a structure like band windings. This work has to be done by means of a computer-controlled machine. This will be the next step in the realization of this idea.

Appendix C. Boundary Element Method and the comparison of its results with experiment.

Any static magnetic field $\boldsymbol{B}$ can be written as:

$$\boldsymbol{B} = \nabla \times \boldsymbol{A} \qquad \text{(C.1)}$$

where $\boldsymbol{A}$ consists of two components: first, the magnetic potential due to the currents

$$\boldsymbol{A}_J(\boldsymbol{r}) = 4\pi\mu_0 \int G(\boldsymbol{r}, \boldsymbol{r'})\boldsymbol{J}(\boldsymbol{r}')d\boldsymbol{r}' \qquad \text{(C.2)}$$

$\boldsymbol{J}(\boldsymbol{r}')$ is the current density distribution, $G(\boldsymbol{r}, \boldsymbol{r}')$ is the kernel, defining the distance from the current element to the point of viewing. The second component is the magnetic field from magnetized regions. They can be described in terms of an equivalent surface current density

$$\boldsymbol{K} = \boldsymbol{M} \times \boldsymbol{n} \qquad \text{(C.3)}$$

where $\boldsymbol{M}$ is the magnetization, and $\boldsymbol{n}$ is the normal to the surface. Using surface current densities, the magnetic potential can be written as:

$$\boldsymbol{A}_K(\boldsymbol{r}) = 4\pi\mu_0 \int G(\boldsymbol{r}, \boldsymbol{r}')K(\boldsymbol{r}')d\boldsymbol{r} \qquad \text{(C.4)}$$

To determine $\boldsymbol{K}$, the interface equation for the continuity of the tangential component of the field intensity is applied:

$$\boldsymbol{n} \times (\boldsymbol{H}_2 - \boldsymbol{H}_1) = 0 \qquad \text{(C.5)}$$

where indexes 1 and 2 denote the two sides of the surface, or

$$\boldsymbol{n} \times \left(\frac{\boldsymbol{B}_2}{\mu_2} - \frac{\boldsymbol{B}_1}{\mu_1}\right) = 0 \qquad \text{(C.6)}$$

Substituting (C.1) into (C.6) for $\boldsymbol{B}$ yields an integral equation in terms of $\boldsymbol{K}$. This equation can be solved for $\boldsymbol{K}$ and subsequently $\boldsymbol{B}$ can be calculated anywhere by addition of (C.2) and (C.4). This integral equation can be solved for example by the method of weighted residuals (see for example the reference [100] for that), as it is done in - "Amperes". The main advantage of the method is that it only deals with the surfaces of magnetized bodies, but not with the volumes. More clearly: this method does not mesh volumes, but it meshes only surfaces between volumes of different permeability.

When material of high permeability is far from saturation, the magnetic flux inside the material follows the boundary of them, strongly decaying with distance from the boundary. The fact that BEM works with surfaces is important: it “feels” this “near-to-boundary” flux, without the necessity to have a fine mesh. Methods, working by volume meshing, need in this case an extraordinary fine mesh to “feel” flux following the boundary of magnetic material.

To test the method and the reliability of the software, a hardware prototype (Figure C1) has been built. We compare its performance with results of simulations.

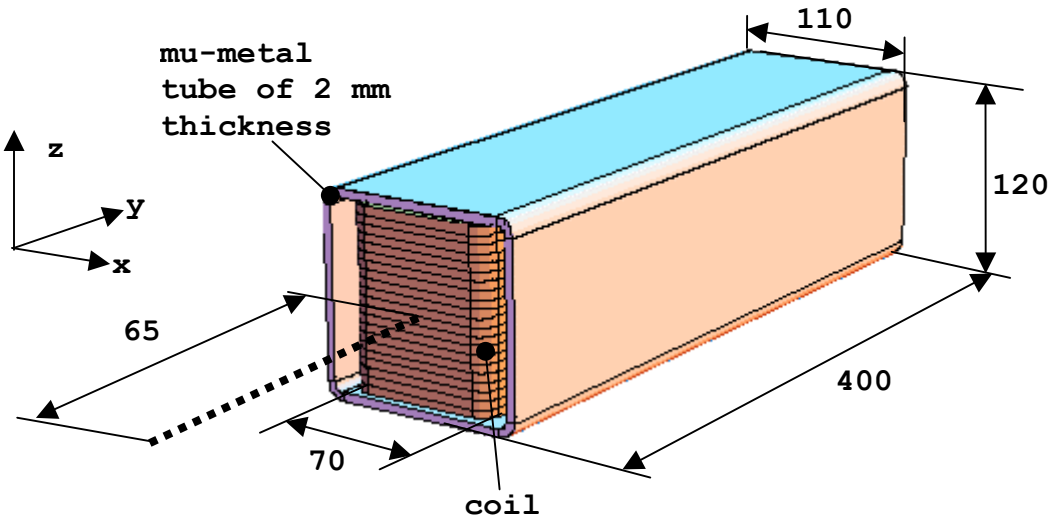

Figure C1: The coil used to test Amperes program (not to scale). The dotted line represents the distance along which the field has been measured to compare with the simulation. The dimensions are given in millimeters.

The model, representing the coil shown in Figure C1, was created in “Amperes”. B_Z, the magnetic field component was the item chosen for comparison. Measurements have been done using hardware of the Reseda Spin Echo spectrometer, and its magnetic shielding system was used to estimate the action of external fields (earth field, fields from electrical devices and so on), so the distortion of the field of the coil produced by the presence of the shielding.

In one measurement such a shielding has been applied, in another measurement, the coil it was not shielded. Results of the measurements are given in Figure C2 in comparison with the BEM simulation.

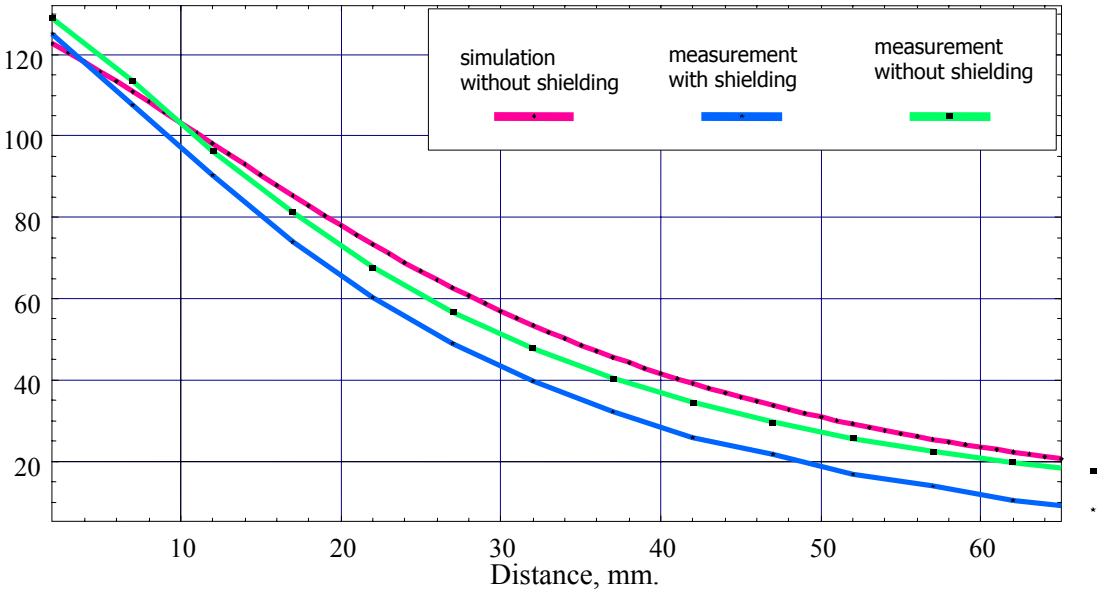

Figure C2: Comparison of BEM simulation with experiment.

The experimental error in the measurements is not more then 1%. Figure C2 shows that the deviation of the simulation from the measurements are not significant (not large then 10 μT).

Therefore, the BEM method and "Amperes" show reasonable agreement with experiment, proving that "Amperes" is a good tool for 3D magnetostatic simulations.

Appendix D. Design of the coils for the MUPAD project.

One of the objectives of this thesis was the design of the spin-flip coils for the Mu-Pad project [101]. The coils should produce a π spin flip with very high precision (better than 1° deviation for a beam of typically 3 cm diameter). The geometrical limitations are the following: the coil should fit to a box of approximately 150×150×50mm. The aim of the work was to optimize the coil geometry to have a sufficiently homogeneous field inside of the coil in the volume passed by the neutron beam, and to have such a small field leakage outside of the coil, to have a spin precession outside the coil no more then 1% of the flip, i.e. – less the 1.8°, and this unavoidable leakage should be localized in the close vicinity of the coil to have no cross-talk between coils, as two coils making spin flips in different planes are planned to be utilized. There are two possibilities to design such coils as shown in Figure D1 and Figure D2. In both coils the field in the beam area is produced by the central coil, and then is guided back to the other side of the coil. In case of the active coil the guiding is done by the aim of mu-metal plates on top and bottom of the coil and two coils of half the cross-section of the central coil on each side of main coil, which are set to the same field value as the central one (the same current) but of opposite direction. In this way the path of the flux produced by the central coil is as follows: central coil – mu-metal plate – right (left) coil – mu-metal plate – back to central coil.

In case of passive guiding a mu-metal yoke is used. The path of the flux is: coil – right (left) part of the yoke – back to coil. In both cases the magnetic flux outside the coil is mostly kept inside of mu-metal yoke (or coil – plate system). The presence of the magnetic field outside the coil is a second order effect; caused by imperfection in the coil manufacturing. There is always a gap between coil and mu-metal, and this point must be estimated very carefully. The gap is simulated in this work as a 1 mm gap (if not defined differently) between coil and yoke (coils and plates for active guiding system).

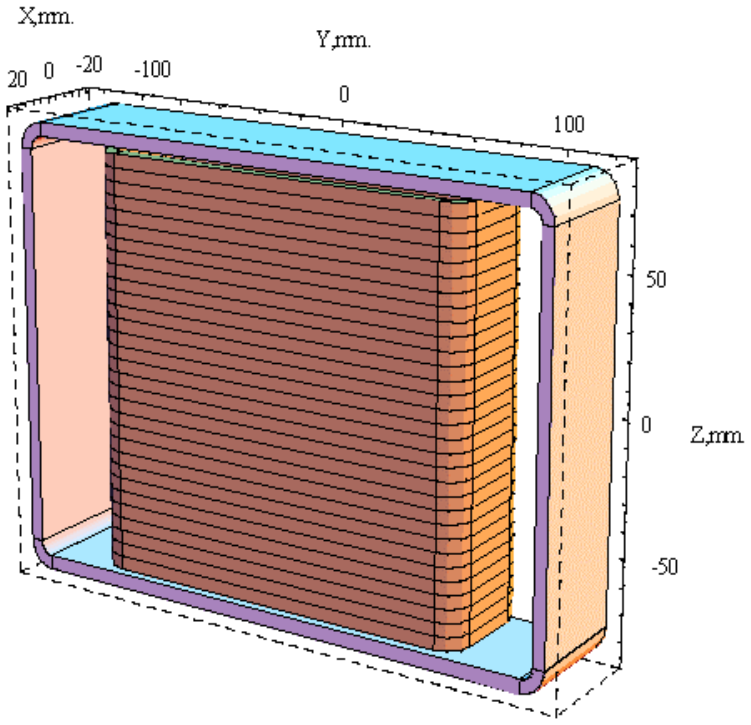

Figure D1: 3D lay-out of a passive coil.

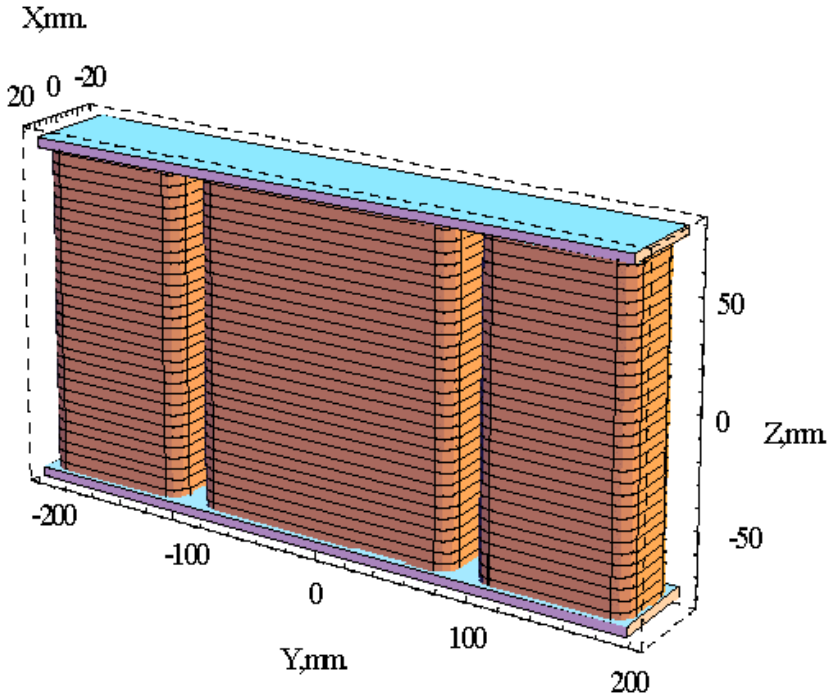

Figure D2: 3D layout of an active coil.

To compare these two basic geometries shown in Figures D1 and D2 simulations have been done by means of the Boundary Element Method (see Appendix C).

Both coils have shown a good homogeneity of the field inside of the coil to be used for the π spin flip in a beam area of 50×50 mm. This field is not changed by further variation of the coil geometry (as is defined by the presence of the mu-metal on top and bottom of the coil) and shows that the spin turn within the beam area will have an error of 0.3°, i.e. 0.15% of the whole spin flip. The variation of the spin precession angle is shown in the Figure D3.

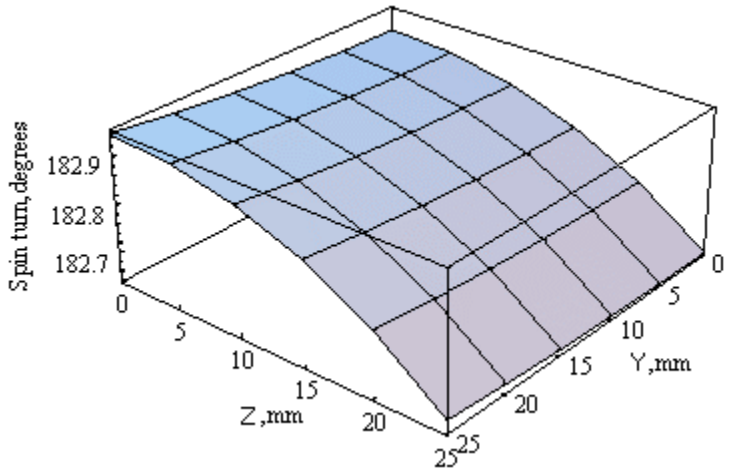

Figure D3: Variation of the spin precession angle through the beam section (Y, Z) of the active coil (Figure D1), obtained only inside of the coil. Neutron paths considered to be parallel to X axis.

The small increase (less then 0.01%) of the field towards the conducting layers of the coil is shown in Figure D4, a bit stronger (less then 0.15%) reduction of the field in direction from the center of the coil to top (or bottom) is shown in Figure D5. Small “hills” on these graphs are caused by some features of the numerical algorithm (singularities in mesh handling) [102], and do not affect the field picture significantly.

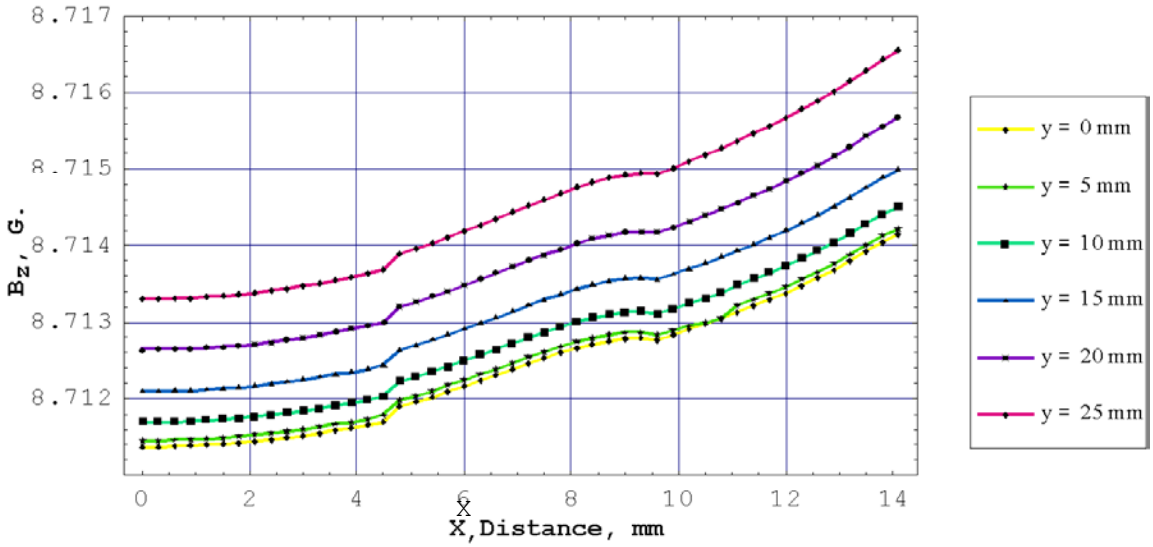

Figure D4: Field inside of coil at Z = 0 (horizontal plane) at different Y values (offset from the optical axis) as function from the distance along the beam axis (with origin in the center of the coil).

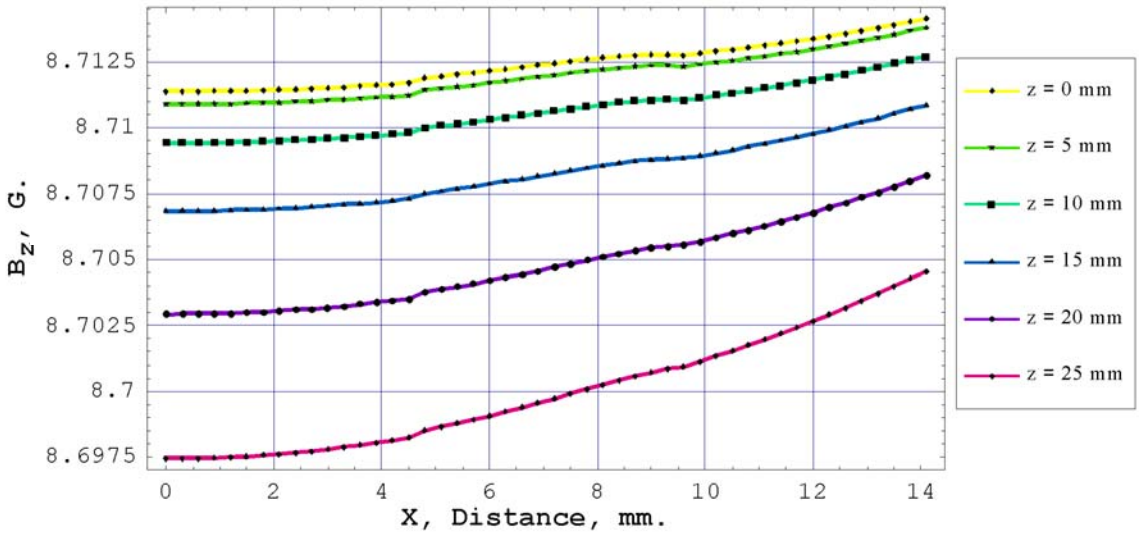

Figure D5: Field inside of coil at Y = 0 (vertical plane) at different Z values (offset from the optical axis) as function from the distance along the beam axis (with origin in the center of the coil).

In order to handle with more distinguishable effects in optimizing the field outside the coil, the field value inside of the coil was set to ~87Gs, what is ten times bigger then the field to be applied in reality (8.7). This has been done for a more detailed optimization of the coil, namely to have a better floating point arithmetic in machine computations, because the expected field outside is rather small in comparison to the field

inside the coil. The mu-metal, even at fields 87G (and at much bigger fields), is far from saturation and the model shows quasi-linear dependence of the magnetization from the current applied to the coil. The comparison of the field from both coils in the beam region outside of the coils along the optical axis is shown in Figure D6.

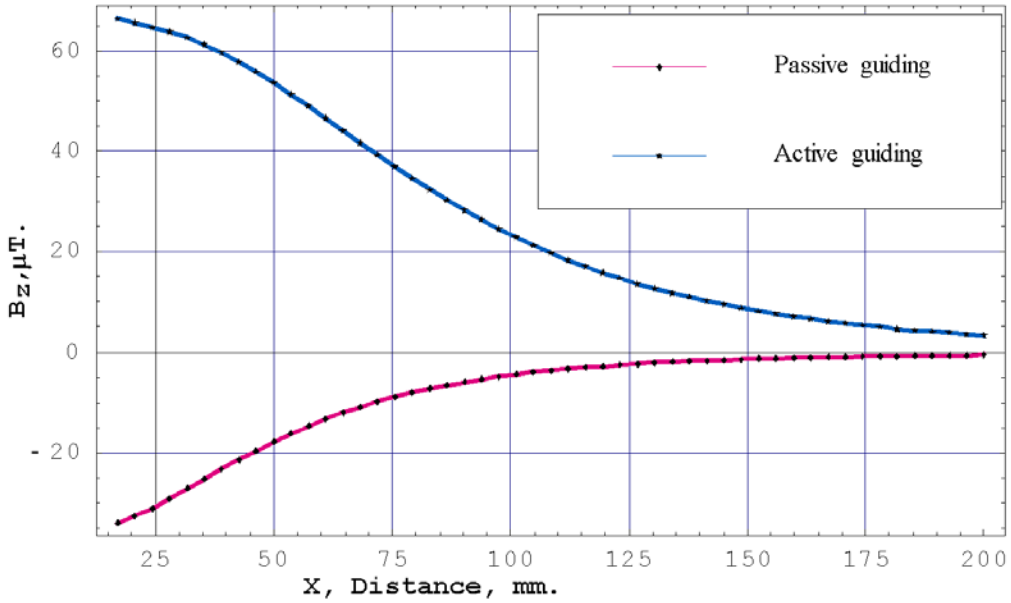

Figure D6: Comparison of the field from both coils in the beam region (along optical axis) outside the coil. The starting point for graphs is 17mm from the coil center, what is + 1 mm out side of the coils (not to handle with a effects of conducting layer).

The coil with passive guiding works better. Path integrals (in terms of spin turn) are 2×10.7° (2× means that the value for path integral is taken on both sides out of the coil) for the passive coil and 2×34.4° for the active coil (for 1500m/s neutrons). One should note that these values have been obtained for the 10× field value. The other effect observed in the simulation is that the outside field of the active coil is positive, while the direction of current was chosen to have positive field inside, and this way the field outside should be negative by sign. But it is not so. It could be that the action of the coil on the sides (which have negative field) makes the field positive. But this fact was not conformed by considering these three coils without mu-metal plates – the sign of the field outside doesn't coincide with the sign of the field inside of the central coil. This means that in presence of mu-metal plates field from side coils suppresses the field from the

central one in the beam region outside the coil. As the simulations of the passive guiding coil have shown better results, it was chosen for the further optimization.

Variation of the yoke geometry have been done, but no one has given a significant improvement - the field outside is rather big in any of the shown configurations (Figure D7).

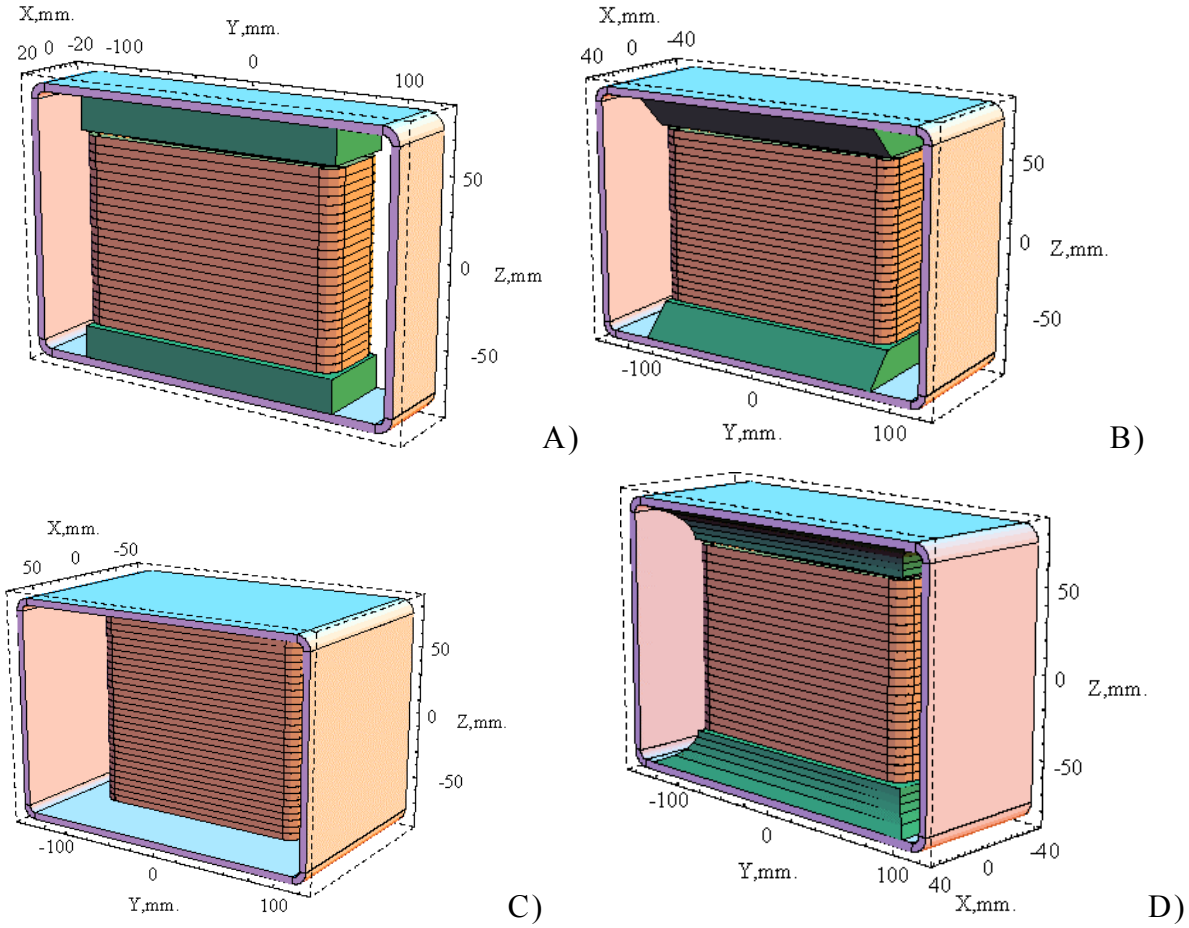

Figure D7: Variation of the yoke shape. Additional parts shown by green color. A) Plates of rectangular cross-section above and below the coil. B) Plates of trapezoidal cross-section. C) Significant overlap of the coil by yoke in X direction. D) Plates smooth transition from coil cross-section to yoke cross-section.

One remark should be made here: the increase of yoke size in x direction reduces the field outside the coil, and we could reach the necessary limit of spin turn in the space outside the coil (which is 1.8°). But within the allowed dimensions of the coil one can not reach a small enough field outside of the coil.

For further reduction of the field outside an additional mu-metal shield of 1 mm thickness was applied – Figure D8.

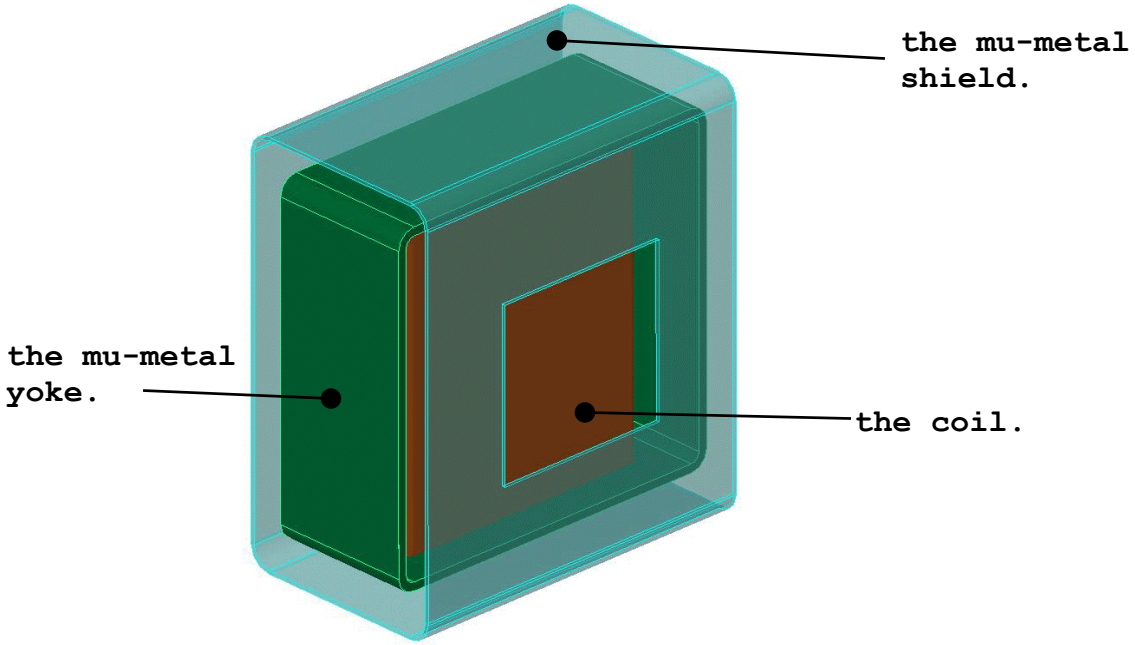

Figure D8: The coil with the shield.

The application of the mu-metal shield reduced the field outside significantly, the path integral becomes 2×2.22° in this case. Round and square beam windows were considered. Simulations have shown very slight difference between them. The graph of the field outside is shown in the Figure D9. At ~140 mm from the coil center the field is already so small, that it can be considered to be zero. It is an important result as for cross-talk problem. Increasing of the shield size in x direction does not make an improvement, as it was in case without the shield. Generally, the mu-metal shield significantly reduces the leakage field outside the coil. The field is reduced by approximately a factor of 5, that is in good agreement with results obtained in 2D simulations by the Finite Element Method (see paragraph 2.2 of this thesis, the corresponding reduction factor there is approximately 2).

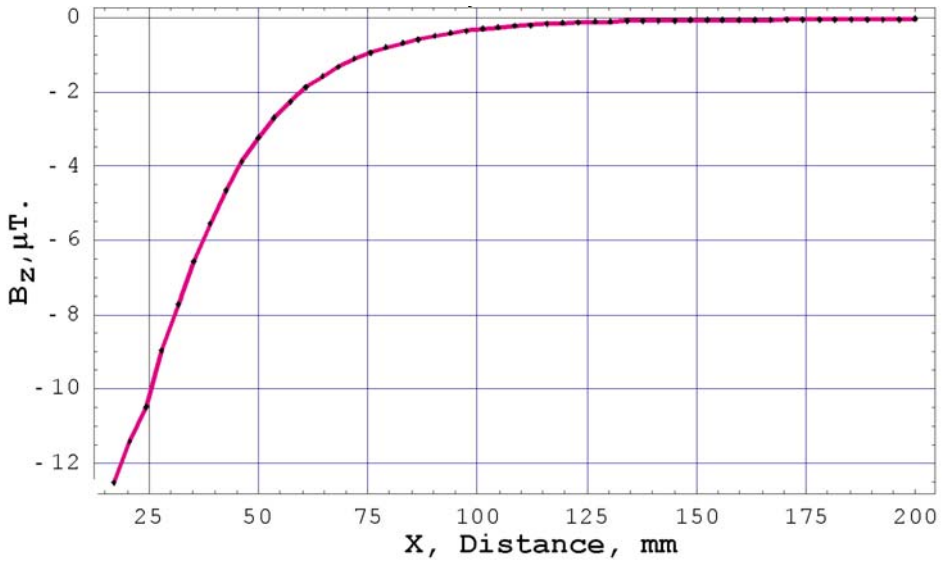

Figure D9: Field outside of the coil.

The application of the mu-metal shield yields a reduction factor of approximately 10^3, when compared with the field inside the coil. As the mu metal is far from saturation (the highest field value inside of the mu-metal yoke is ~ 1896 G at the field inside the coil of 87 G), one could expect the model to behave quasy-linear, what means that if the current in the coil is reduced ten times, as needed in reality, the field outside will reduced approximately ten times too. But it is not really so, as shown in Figure D10. Path integral outside of the coil here is 2×0.92. This value is already small enough that the coil can be used. But it is at the limit, and different manufacturing errors can spoil the situation. To avoid it, some effort should be put into the construction of the coil. Further reducing of the field outside can be achieved by reducing the gap between the coil and the yoke. The gap between coil and the yoke was 1 mm in all the previous simulations. The reduction of this gap to 0.5 mm (what can be achieved by the technology of coils manufacturing) gives some reduction of the field outside, approximately of 30%, as shown in Figure D11. The angle of the Larmor precession in the outside field is here 0.69°*2 = 1.38°. This is already well below the necessary limit (1.8°). Further reduction of the outer field can be achieved by implementation of a second mu-metal shield, what should decrease the field outside of the coil approximately five times.

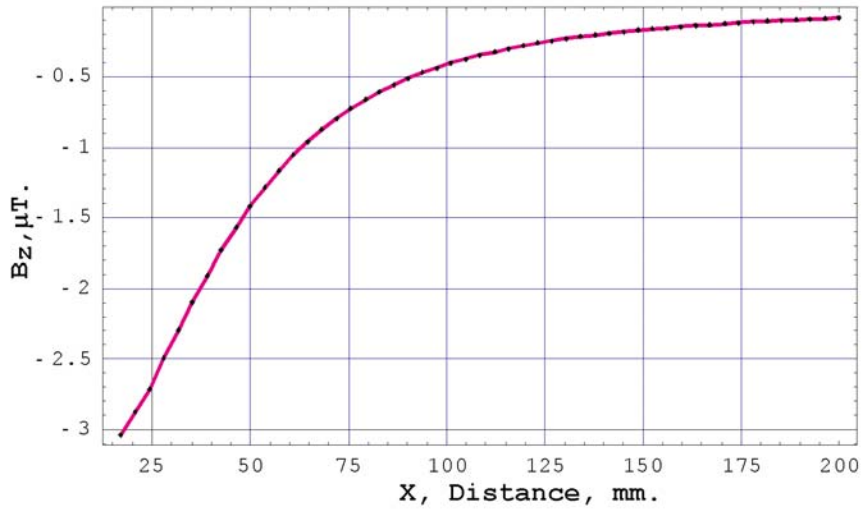

Figure D10: Field outside of the coil, current value to have a π spin flip is applied to the coil.

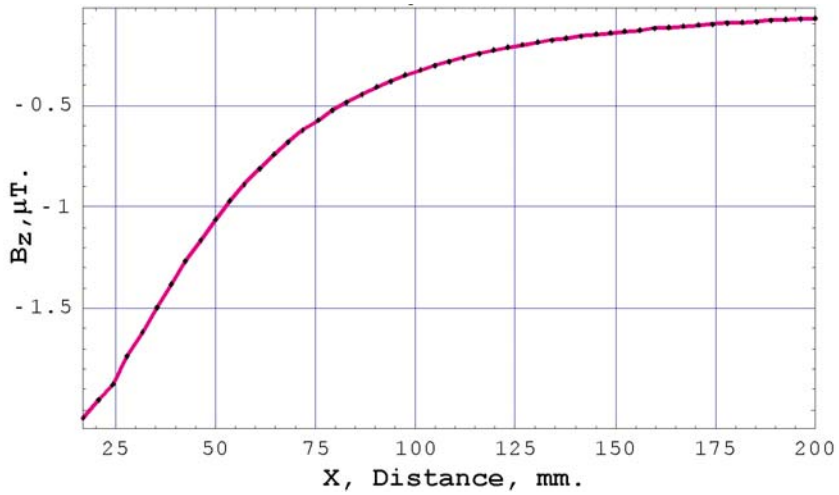

Figure D11: Reduction of the field outside the coil if the gap between yoke and coil is reduced to 0.5 mm instead of 1 mm.

Calculation of two shields is a very challenging task, and could not be done because of the limit of the available computer resources. At this stage the design of the coils for the MU-PAD project can be considered to be completed successfully. Coils of the chosen geometry show good homogeneity of the field inside of the coil, and a reasonably low field outside the coil. It is shown that passive guiding of the flux is significantly better then active guiding for the reduction of the field outside of the coil.

3D simulations of magnetic shielding have been done, and they show a strong (5 times) reduction of the field outside of the coil. Only application of the shield reduces the field well enough, but if we make the gap between coil and yoke (on top and bottom of the coil) of 0.5 mm (what is an acceptable value for the coil manufacturing), the field also becomes much lower. The drawing of the magnetic system (the coil, the yoke and the shielding together) is given in Figure D12.

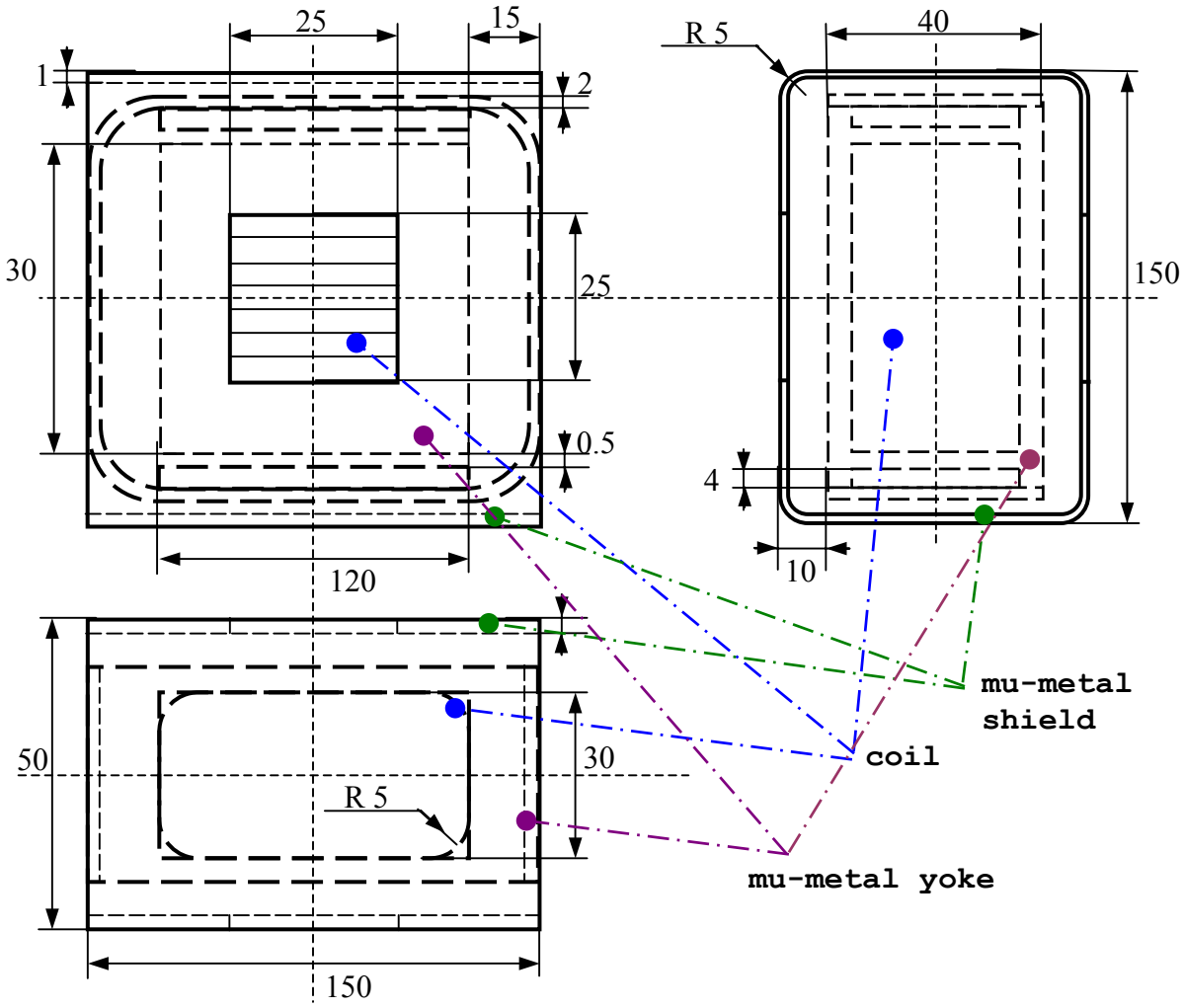

Figure D12: The drawing of the spin-flip coil for the MU-PAD project.

Appendix E: **Magnetostatic inverse problem. The basic formulation of the task and a simple example.**

All the approaches used until now for the magnetostatic design, i) either particular approach is based on a purely analytical calculation without using any iteration procedures, or ii) a numerical approach, using iteration procedures, both work in the following manner: one has to define the geometry (coils sizes, currents in them, magnetic materials residing in the magnetic field and so on) and then this approach (usually some computer code) will give (after the calculation of the defined model) the distribution of the magnetic field for the given geometry.

The inverse problem consists in developing a method, which would work the other way around – namely in this approach one has to define the field configuration, and from this field distribution the geometry (coil sizes and currents, magnetic material and so on) necessary for the creation of this field should be calculated (by computer or another manner). The basic idea of the inverse task for the magnetostatic was proposed by Dr. Oleg Chubar in 2001 (at ESRF at that time).

Mathematically this problem can be formulated in a short way: The geometry that provides the magnetic field of the desired configuration should minimize following functional:

$$D(G) = \left\| f_{desired} - M(G) \right\|_L + \left\| w_1(G) \right\|_L + \left\| w_2(G) \right\|_L + ... + \left\| w_i(G) \right\|_L \quad \text{(M1)}$$

where $f_{desired}$ is the field distribution which should be reached in the minimization of the functional (M1), G is the geometry (the parameter which should deliver a minimum), M is the operator giving the field distribution, which acts on the geometry G, $w_1(G)$ … $w_i(G)$ are the constrain functionals demanding some limits for the geometry, which could be the limits of the currents to be used for the real hardware for the magnetic device, demand of continuity (or discontinuity) for some regions in the model, like demand of continuity of current carrying elements of geometry or some geometrical shape or size limitations; L is the norm to be chosen for the functional minimization.

What do we mean here under the term of magnetic field operator M can be explained within the simple example of the Bio-Savart law:

$$\boldsymbol{B}(\boldsymbol{r}) = \frac{1}{c}\int \frac{[\boldsymbol{j}(\boldsymbol{r}) \times \boldsymbol{r}]}{r^3} dV \qquad \text{(M2)}$$

where ***j(r)*** is the distribution of the current , ***r*** is the coordinate vector, and *c* is the speed of light. The magnetic field operator in this case is the integration of current distribution over the kernel $-\frac{1}{\boldsymbol{r}^3}\boldsymbol{r}\times$. The "geometry" in this case is the current distribution.

Another example can be given in the 2D case, when the field of the solenoid is defined by the equation:

$$\boldsymbol{B}(\boldsymbol{r}) = \frac{1}{c}\left(\sum_{1}^{N} J \frac{[\boldsymbol{n} \times (\boldsymbol{r} - \boldsymbol{r}_i)]}{(\boldsymbol{r} - \boldsymbol{r}_i)^2} - \sum_{N+1}^{2N} J \frac{[\boldsymbol{n} \times (\boldsymbol{r} - \boldsymbol{r}_i)]}{(\boldsymbol{r} - \boldsymbol{r}_i)^2} \right) \qquad \text{(M3)}$$

where *J* is the current applied to the coil, ***r*** is the observation point, $\boldsymbol{r}_\text{i}$ are the positions of the wires comprising the coil, their distribution is given in Figure E1. N is the number of winding of the coil, ***n*** is the normal to the plane of drawing. We may not care here that in equation (M3) the effects of the finite size of the wires are not taken into account. If we use orts ***i*** and ***j*** on the plane of consideration, the positions of the wires $\boldsymbol{r}_\text{i}$ and equation M3 can be read as follows:

$\boldsymbol{r}_i = -\boldsymbol{iL} + \boldsymbol{j}d \cdot \text{i}$, when I = 1 .. N, and

$\boldsymbol{r}_i = \boldsymbol{iL} + \boldsymbol{j}d \cdot \text{i}$, when I = N+1 .. 2N;

$$\boldsymbol{B}(\boldsymbol{r}) = \frac{1}{c}\left(\sum_{1}^{N} J \frac{[\boldsymbol{n} \times (\boldsymbol{r} - (-\boldsymbol{iL} + \boldsymbol{j}d \cdot \text{i}))]}{(\boldsymbol{r} - (-\boldsymbol{iL} + \boldsymbol{j}d \cdot \text{i}))^2} - \sum_{N+1}^{2N} J \frac{[\boldsymbol{n} \times (\boldsymbol{r} - (\boldsymbol{iL} + \boldsymbol{j}d \cdot \text{i}))]}{(\boldsymbol{r} - (\boldsymbol{iL} + \boldsymbol{j}d \cdot \text{i}))^2} \right) \qquad \text{(M4)}$$

In this simple two-dimensional approach we further formulate an example of reverse task. Figure E1 illustrates the simple approach for calculation of the field of the solenoid. Such coils are widely used in condensed matter studies with polarized neutrons for the creation of the static, highly-homogeneous magnetic field in a well-defined region of the space.

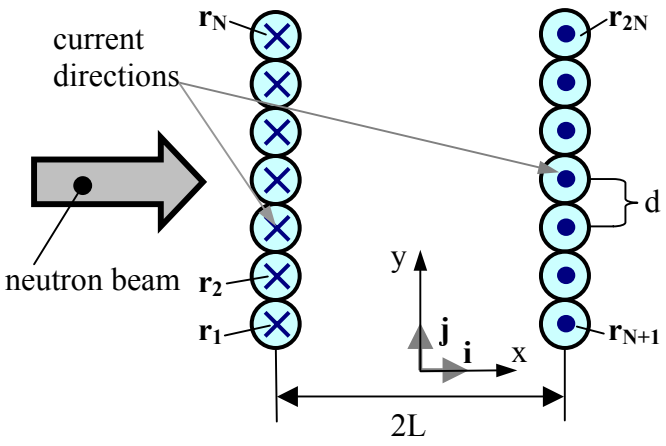

Figure E1: The solenoid in two-dimensional approach.

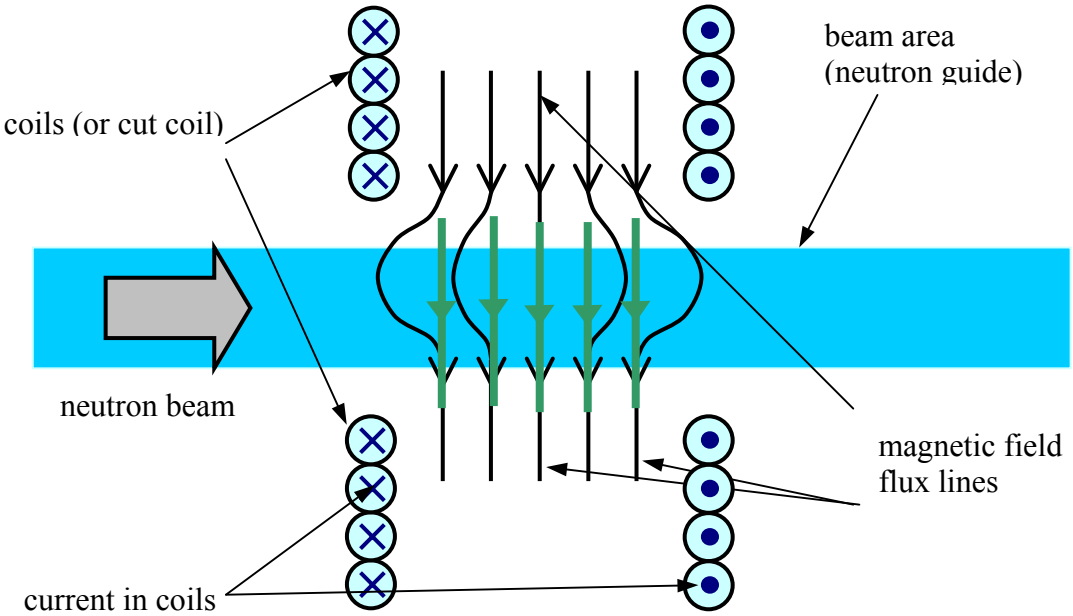

Figure E2: The field distribution of the solenoid in a two-dimensional approach in the case when the current carrying elements (windings) are removed from the center of the coil (in the beam area). Green arrows show the desired field, current distribution for the creation of which should be obtained by solving the inverse task.

In this case the "geometry" is the distribution of wires $\boldsymbol{r}_i$ and the current J; the operator of magnetic field in this case is given by (M3) or (M4).

One of the problems in optimizing the performance of these coils is the scattering and absorption of the neutrons by the material constituting the current conducting elements (windings) of the coils, that leads to the reduction of the neutron beam intensity. There are some instruments where the current carrying elements of the coil are removed from the beam area. But this removing leads to a strong non-homogeneity of the magnetic field in the beam area, as it is shown in Figure E2, leading to a significant loss of the neutron beam polarization. It would be great to have such a type of coil, but with straight, homogeneous field in the coil region with sharp edges. For example, one could try to reach this result by looking for some special current distributions in the upper (symmetry identical the lower) part of such a coil with a cut in the middle. And it is exactly the inverse task as it is formulated by equation (M1). The main problem arising in solving this problem is the choice if the norm L in equation (M1), that has not been solved in general form yet, and remains a question for future investigations.

References.

[1] S.W. Lovesey, T.Springer, Dynamics of Solids and Liquids by Neutron Scattering, in Topics in Current Physics Volume 3, Berlin Heidelberg New York, Springer Verlag, 1977.

[2] Klimko. S. „ZETA, A zero field spin echo method for very high resolution study of elementary excitations and first application „ Doktorarbeit, Fakkultät fûr Physik, Technischen Universität Berlin. 2003.

[3] Neutron Spin Echo Spectroscopy , F. Mezei, C. Pappas p.5

[4] P.Hank, "Aufbau des Neutroneneresonanz-Spinechospektrometer in Saclay und Erweiterung der Me . möglichkeiten durch die MIEZE-Option", Doktorarbeit, Fakultät für Physic, Technischen Universität München, (1999).

[5] http://tumb1.biblio.tu-muenchen.de/publ/diss/ph/2003/bleuel.pdf

[6] http://www.ill.fr/YellowBook/IN20/

[7] F. Mezei, in: Neutron Inelastic Scattering (IAEA, Vienna, 1978), p.125.

[8] Phys. Rev., 70, pp.460-474, (1946)

[9] Rev. Mod. Phys., 26, pp.167-171, (1954)

[10] Am. J. Phys. 62(9), 1994

[11] http://www.ansys.com/

[12] Moaveni, S. Finite Element Analysis: Theory and Application With ANSYS. Prentice-Hall, Upper Saddle River, NJ, 1999, 527 pp., 2003.

[13] P. Hank and so on, Proceedings of the Third Summer School on Neutron Scattering, Zuoz 20-26 Aug. 1995

[14] D.V. Sivuhin. General Physics, Vol. 4 "Optics", Moscow, "Nauka", 1987

[15] www.integratedsoft.com

[16] Physica B, 234-236, p. 1130 (1997)

[17] Physica B, 234-236, p. 1126 (1997)

[18] J. Synchrotron Rad. (1988). 5, p. 481

[19] IEEE Trans. Magn. 18(6) p. 1860

[20] Physica B, p. 266 (1999)

[21] Phys. stat.sol. 42, 821 (1970).

[22] Phys. Rev. B, Vol.10, p.612 (1974)

[23] Phys. Rev. B, Vol.26, p.5658 (1982)

[24] Phys. Rev. B, Vol.29, p.4541 (1984)

[25] M. Cardona, in Festkoerperprobleme/Advances in Solid State Physics, Vol. 34, edited by R. Helbig. Vieweg, Braunschweig/Wiesbaden, 1994,p.35.

[26] Solid State Commun. 96, p. 111 (1995).

[27] J. Appl. Phys. 77, p. 2857 (1995).

[28] Phys. Rev. B. 52, p. 1115 (1996)

[29] Phys. Rev. B 38, p. 5219 (1988).

[30] Solid State Commun. 90, 295 (1994)

[31] Phys. Rev. B 56, p. 237 (1997).

[32] Phys. Rev. B 54, p. 11305 (1996).

[33] Phys. Rev. B 56, 9431 (1997)

[34] Appl. Phys. Lett. 71, 2109 (1997).

[35] Phys. Rev. B 44, 8633 (1991).

[36] Phys. Rev. B 56, 13 167 (1997).

[37] Phys. Rev. B 57, 1348 (1998).

[38] Phys. Rev. B 56, 210 (1997).

[39] Phys. Rev. B 65, 075206 (2002)

[40] Phys. Rev. B 58, 10443-10451 (1998)

[41] Phys. Rev. Lett. 78, 1283-1286 (1997)

[42] Phys. Rev. B 49, 8263-8272 (1994)

[43] Phys. Rev. Lett. Vol. 85, p. 586 (2000)

[44] Phys. Rev. B 48, 12661 (1993).

[45] Phys. Rev. B 58, 10510 (1998)

[46] Phys. Rev., B 65, 075206, (2002)

[47] Phys. Rev. B 43, 4541, (1991)

[48] Phys. Rev. B, Vol.5, p.3151 (1972)

[49] W. Weber, Phys. Rev. B 15, 4789 (1977).

[50] Chemical Physics, V. 40, p. 345-357(1979)

[51] Chemical Physics, V. 40, p. 345-357(1979)

[52] Helen M. J. Smith, Phil. Trans. of Royal. Soc. Of London. Series A, p.105 (1947)

[53] http://cms.mpi.univie.ac.at/vasp/vasp/vasp.html

[54] http://www.abinit.org

[55] http://www.pwscf.org

[56] http://wolf.ifj.edu.pl/phonon/

[57] Computational Materials Science 25, 478-492 (2002)

[58] Phys.Rev.136 (1964)B864.

[59] Phys.Rev.140 (1965)A1133

[60] Rev.Mod.Phys.64 (1992)1045.

[61] Math.Comput.19 (1965)577.

[62] J.Comput.Chem.3 (1982)214.

[63] Phys.Rev.Lett.69 (1992)3789.

[64] Phys.Rev.159 (1967)98.

[65] F.S.Acton, in :Numerical Methods That (Usually)Work, Harper and Row, New York,1970,p.130.

[66] Rev.Lett.58 (1987)1861.

[67] Phys.Rev.B 58 (1998)3641.

[68] Phys.Rev.B 47(1993)4238.

[69]Solid State Commun.17 (1975)1425, Phys. Rev.B 15 (1977)2884.

[70] E.K.U.Gross, J.F.Dobson, M.Petersilka, "Density functional theory II",in:R.F.Nalewajski (Ed.),Topics in Current Chemistry,vol.181,Springer,Berlin,1996,p.81.

[71] Phys.Rev.Lett.82 (1999)2123.

[72] http://www.netlib.org/lapack/

[73] http://www.fftw.org/

[74] Phys. Rev. Lett. 58, 1861.

[75] Rev. of Modern Phys., 73, p.515 2001

[76] http://www.pwscf.org/pseudo/1.3/html/Ge.html

[77] Phys. Rev. B 59, 6182-6188 (1999)

[78] Phys. Rev. B 67, 144304 (2003)

[79] B.N. Brockhouse, et all "Neutron inelastic scattering , Vol.II", (IAEA., Vienna), (1968)

[80] D.V. Sivuhin. General Physics, Vol. 4 "Optics", Moscow, "Nauka", 1987

[81] M. J. Cooper & R. Nathans, Acta Cryst. 23, 357, (1967).

[82] B. Dorner, Coherent Inelastic Neutron Scattering in Lattice Dynamics, in Springer

Tracts in modern Physics, 93, Berlin Heidelberg New York, Springer Verlag, 1982.
[83] Neutron Spin Echo Spectroscopy , F. Mezei, C. Pappas, p.74
[84] Neutron Spin Echo Spectroscopy , F. Mezei, C. Pappas p.116
[85] Klimko. S. „ZETA, A zero field spin echo method for very high resolution study of elementary excitations and first application „ Doktorarbeit, Fakkultät fûr Physik, Technischen Universität Berlin. 2003.
[86] Phys. Rev. B, 3, pp.364-369, (1971)
[87] Acta Cryst. A 25, pp.547-550, (1969)
[88] http://neutron.risoe.dk/
[89] http://www.mathworks.com/
[90] Phys. Rev. B, 50 p. 13347 (1994)
[91] Phys. Rev. B 10, 612-620 (1974)
[92] Phys. Rev. B 67, 144304 (2003)
[93] http://www.ill.fr/YellowBook/IN3/
[94] http://whisky.ill.fr/tas/practical/MadHelp/index.html
[95] Sacha Ivanov, communications
[96] Franz Demmel, communications.
[97] http://www.amuneal.com/pages/magshield-formula.ph
[98] http://www.mems-exchange.org/catalog/evaporation/
[99] Baltic Equipment Factory.
[100] Magnetostatic Modeling Guide of Amperes program, www.integratedsoft.com
[101] on MU-PAD project
[102] Tom Judge, www.integratedsoft.com, communications.

Acknowledgements.

It is my pleasure to thank the many people who made this thesis possible.

Prof. Peter Böni for presenting me with an opportunity to work and study in the area of Neutron Research at FRM-2,. I am grateful for his leadership, sound advice, encouragement and continuous support.

Prof. Wolfgang Gläser for friendly hospitality in his institute in the beginning my staying in Munich.

Prof. Winfred Petry for welcoming me to the world of science, helping me adjust to my new environment, patiently sharing his expertise and knowledge about NRSE and taking the time to proofread this thesis thoroughly. I am especially grateful to him for taking the time to discuss my numerous questions

Dr. Roland Gähler. I really would like to thank you for all you did for me all this time. For leadership and expertise not only in science and technique but also in the world of around the science bureaucracy and the hardest point of the "political physics". I'm really thankful to you that you gave me the first chance to start this work and for the second chance to complete.

Dr. Markus Bleuel for his kindest support in all time of my staying in Munich. If you would not be there, it would much harder for me to survive in Munich, especially in very beginning of my stay. All the time you were opened for help and discussions, thank you very much.

Dr. Sergey Klimko for the perfect discussions, and mostly for the friendly support and for the proper words have been said in proper time. Definitely without you this work could not be completed.

Dr. Tomas Keller for his faithful participation in every part of work on magnetostatic and spin-precession simulations.

Dr. Alex Mirmelstein for his always thoughtful support and beautiful scientific discussions.

Dr. Evgeniy Clementev for perfect scientific discussion.

Dr. Bruno Dorner for the one but very important talk on science and all around in my life

Markus Axtner for the perfect technological expertise.

To my parents - just thank you very much for I'm being. To my grand parent for …more less the same ☺.

To Tanyana Tikhonova, aka TANYA, for you were in my life. I wouldn't survive without your mental support in first year of my staying in Munich. Probably I should say "I'm sorry" for plenty of things which were further… but you see, I was frank with you.

To Alexander Selvachev, aka ISCANDER, for everything for the support and for the critics. It really helped me. For the thought that "your way of the feeling about life is not only possible".

To Vladimir Bondarenko, aka BONDA, and Oksana Kirilenko, aka XU, just because you were good friends to me all that time.

To Natalya Bobrovskih (Migacheva), aka TOSHKA for unbelievable fredship, care and support, and to her husband Zhenya that he made her a happy women.

To Irina Moiseenko, aka IRA, for your were real, honest and frank friend all this time.

To Andrey Maklakov, aka ZDOROVIY, just for understanding without word. For the solid feelings "your back is protected".

To Alexander Makeev, aka McCeeff , especially for songs, for the pack of cigarettes you bought that time, and for the fact that you are always a good friend.

To Pavel Lousan, aka PASHA. For friendship, always mixed somehow with scientific discussion. For always being ready to reply my crazy question about numerical math and Linux computing.

To Alexander Lazar, aka SANICH, for OBR (BU) "PCHELKA", and for feelings that "everything is never over".

To Oleg Kalashev, aka KALASHEV, for our meetings in Munich, Geneva, Grenoble, and for the feeling "just do it, if you like this work, and everything will be fine".

To Vladimir Treschikov, aka VOVA, for the altitude, friendship and for the words: "be cool and be yourself"

To Elelna Silant'eva, aka LENKA, for good friendship, for the real support and hiking trips your organized for me.

To Aleksey Virsis, aka VIRUS, and to Ludmila Virsis, aka MILKA, just for everything and for the place where you are always welcome.

To Alla Partigulova, aka ALYA, for you black hairs and for you have saved my life that autumn in Munich.

To Yakov Fominov aka YASHA and to Marina Fominova aka MARINA, for the perfect science discussions and for frank support.

To Yury Borisov aka YURA, for friendship and for the song about “Pentod 6G2P”.

To Elena Reut aka LYALKA, for the help to my grandfather.

To Ilya Valuev aka ILYA, for visits to me in Munich and for being opened for collaboration.

To Nataliya Konvisar, aka KONVISARSHA, for partnership in all our crazy projects and for tzhe responsibility in them.

To Maxim Oxrimenko aka MAKS, for friendship and for believe in my idea in the fields on numerical math.

To Juliya Abramova, aka YUL’KA, for friendship and for you made ISCANDER a bit more happy man.

To Aleksey Alyanin aka YOSCH, for Cheget mountain, for friendship.

To Olga Semenova aka OLYA, for friendship and for being always opened for crazy idea to go to some place you have never been before.

To Yury Evdokimov, aka YURASIK, and to Nadya Evdokimova aka NADYA, for being opened, frank and easiness.

To Igor Getman, for the bringing me to the wonderful world of the mountain sky.

To Vladimir Nogaller, for marvelous mountain trips we did together in Oberbayern.

And you everyone, who was in my life all this time!

That is all for the moment, HAVE FUN !!! 8-)))